National Library
of Canada

Bibliothèque nationale
du Canada

Acquisitions and
Bibliographic Services Branch

Direction des acquisitions et
des services bibliographiques

395 Wellington Street
Ottawa, Ontario
K1A 0N4

395, rue Wellington
Ottawa (Ontario)
K1A 0N4

Your file Votre référence

Our file Notre référence

NOTICE

The quality of this microform is heavily dependent upon the quality of the original thesis submitted for microfilming. Every effort has been made to ensure the highest quality of reproduction possible.

If pages are missing, contact the university which granted the degree.

Some pages may have indistinct print especially if the original pages were typed with a poor typewriter ribbon or if the university sent us an inferior photocopy.

Reproduction in full or in part of this microform is governed by the Canadian Copyright Act, R.S.C. 1970, c. C-30, and subsequent amendments.

AVIS

La qualité de cette microforme dépend grandement de la qualité de la thèse soumise au microfilmage. Nous avons tout fait pour assurer une qualité supérieure de reproduction.

S'il manque des pages, veuillez communiquer avec l'université qui a conféré le grade.

La qualité d'impression de certaines pages peut laisser à désirer, surtout si les pages originales ont été dactylographiées à l'aide d'un ruban usé ou si l'université nous a fait parvenir une photocopie de qualité inférieure.

La reproduction, même partielle, de cette microforme est soumise à la Loi canadienne sur le droit d'auteur, SRC 1970, c. C-30, et ses amendements subséquents.

Canada

Magnetic Properties of Metastable fcc Co(001) Ultrathin Films

by

Maciej Matthew Zbigniew Kowalewski

THESIS SUBMITTED IN PARTIAL FULFILLMENT OF
THE REQUIREMENTS FOR THE DEGREE OF
MASTER OF SCIENCE
in the
Department
of
Physics

SIMON FRASER UNIVERSITY
August 1993

National Library
of Canada

Acquisitions and
Bibliographic Services Branch

395 Wellington Street
Ottawa, Ontario
K1A 0N4

Bibliothèque nationale
du Canada

Direction des acquisitions et
des services bibliographiques

395, rue Wellington
Ottawa (Ontario)
K1A 0N4

Your file Votre référence

Our file Notre référence

The author has granted an irrevocable non-exclusive licence allowing the National Library of Canada to reproduce, loan, distribute or sell copies of his/her thesis by any means and in any form or format, making this thesis available to interested persons.

L'auteur a accordé une licence irrévocable et non exclusive permettant à la Bibliothèque nationale du Canada de reproduire, prêter, distribuer ou vendre des copies de sa thèse de quelque manière et sous quelque forme que ce soit pour mettre des exemplaires de cette thèse à la disposition des personnes intéressées.

The author retains ownership of the copyright in his/her thesis. Neither the thesis nor substantial extracts from it may be printed or otherwise reproduced without his/her permission.

L'auteur conserve la propriété du droit d'auteur qui protège sa thèse. Ni la thèse ni des extraits substantiels de celle-ci ne doivent être imprimés ou autrement reproduits sans son autorisation.

ISBN 0-315-91202-2

Canada

Approval

Name: Maciej Matthew Zbigniew Kowalewski

Degree: Master of Science

Title of Thesis: Magnetic Properties of Metastable fcc Co(001) Ultrathin Films

Examining Committee:

Chair: Dr. M. Thewalt

Dr. B. Heinrich
Senior Supervisor

Dr. A.S. Arrott

Dr. J.F. Cochran

Dr. E.D. Crozier

Dr. R.F. Frindt

Date Approved: August 13, 1993

Title of Thesis/Project/Extended Essay

Magnetic Properties of Metastable fcc Co (001) Ultrathin Films

Author: ________

(signature)

Maciej Matthew Z. Kowalewski

(name)

August 18TH, 1993

(date)

ABSTRACT

Metastable fcc Co(001) ultrathin films were grown on fcc Cu(001) single crystal substrate by means of Molecular Beam Epitaxy (MBE). The growth was monitored using the Reflection High Energy Electron Diffraction (RHEED) technique. RHEED intensity oscillations revealed that metastable fcc Co(001) grows on a fcc Cu(001) substrate in a quasi layer-by-layer mode and RHEED patterns showed that Co atoms follow the in-plane spacing of the Cu template. The magnetic properties of Co ultrathin structures were investigated by employing the Ferromagnetic Resonance (FMR) technique. The FMR measurements on single cobalt layer samples, Cu(001)/Co/Cu, were used to determine the fcc Co(001) magnetic parameters such as the in-plane and the perpendicular magnetic anisotropies, the spectroscopic g-factor and the magnetic damping.

The ultrathin cobalt films exhibited large uniaxial perpendicular anisotropies with the hard axis normal to the film plane and large fourfold in-plane anisotropies with the easy axes along the <110> crystallographic directions. The thickness dependence of the perpendicular uniaxial anisotropy and the fourfold in-plane anisotropy were measured. Both anisotropies are shown to be well described by a sum of contributions from a constant term and from a term proportional to 1/d. The constant term is due to tetragonal distortions of the fcc Co(001) lattice, and the 1/d dependent term originates from the intrinsic interface anisotropy. The temperature dependence of the magnetic anisotropies is discussed.

The exchange coupling between Co layers through the fcc Cu spacer layer was studied in several Cu(001)/Co/Cu/Co/Cu structures. The FMR studies revealed that the magnetic properties of single Co layers are different from the magnetic properties of films of the same thickness situated in Co/Cu/Co trilayer structures.

Dedication

For my supportive and loving family: my parents, Wanda and Zbigniew, my wife, Virginia, and my children, Daniela, Tatiana and Andrew.

Acknowledgments

It has been a gratifying experience to work with the Magnetism and Surface Science Group at Simon Fraser University. Most important I would like to thank my senior supervisor Dr. Bretislav Heinrich for his guidance and support. His invaluable advice has been most essential to this work. Our stimulating discussions have broadened my understanding of magnetism and molecular beam epitaxy and motivated me to continue acquiring the knowledge. I am very lucky to have been associated with an experimentalist of his expertise. I have benefited greatly not only from his immense scientific expertise, but also from his personal wisdom. I am very grateful for his moral support and personal advice in the time of need. Thank you.

I wish to thank the members of my supervisory committee, Dr. Daryl Crozier, Dr. John Cochran and Dr. Anthony Arrott, for their advice and assistance during my pursuit of the Master degree. I am particularly grateful to Dr. John Cochran for a very careful reading of this thesis and for his valuable comments.

I thank the post-graduate student, Dr. Zbigniew Celinski, for allowing me to participate in many of his experiments and for finding plenty of time and patience to explain the operations of the MBE system and the FMR apparatus. I am also grateful to Mr. Ken Myrtle for his assistance in matters of MBE.

I would like to thank Dr. Jurgen Kirschner for supplying the copper substrate and participating in some of the experiments. I thank Dr. Clauss Schneider for very valuable discussions concerning strains in cobalt films.

I wish to express my pleasure to have been working or talking with the many people I came to know at SFU including Dr. Janusz Chrzanowski, Mr. David Atlan, Mr. Jaegwang Lee, Dr. Yutaka Yoshida, and Dr. Milton From.

Table of Contents

Approval ii

Abstract iii

Dedication v

Acknowledgments vi

List of Tables x

List of Figures xi

1. Introduction 1

2. Growth of Metastable fcc Co(001) Ultrathin Structures 3

- 2.1 Introduction 3
- 2.2 Molecular Beam Epitaxy apparatus 3
- 2.3 Reflection High Energy Electron Diffraction (RHEED) 7
  - 2.3.1 Kinematic approximation 7
  - 2.3.2 The Ewald construction 11
  - 2.3.3 RHEED intensities for point scatterers 13
  - 2.3.4 RHEED intensity oscillations 22
- 2.4 Sample preparation and growth characterization 24
  - 2.4.1 Preparation of the fcc Cu(001) substrate 24
  - 2.4.2 Film preparation and nomenclature 25
  - 2.4.3 RHEED patterns of the Cu substrate and deposited films . 28
  - 2.4.4 RHEED oscillations of Co and Cu 30
- 2.5 Tetragonal distortion of the fcc Co(001) films 31

3. FMR Theory for Ultrathin Films 33

3.1 Introduction 33

3.2 Landau-Lifshitz equation of motion for magnetization 33

3.3 Geometry of FMR 40

3.4 Internal fields 43

3.5 The magnetocrystalline anisotropy 46

3.6 The demagnetizing field 52

3.7 Resonance condition 54

3.8 FMR linewidth ΔH 57

3.9 FMR apparatus 57

4. Ferromagnetic Resonance Studies of Ultrathin fcc Co(001) Structures 62

4.1 Introduction 62

4.2 Experimental results and analysis of magnetic anisotropies 62

4.2.1 Calculations of the g-factor 65

4.2.2 Magnetic anisotropies 68

A. Perpendicular uniaxial anisotropies 71

B. Fourfold in-plane anisotropies 72

4.2.3 Discussion 76

4.3 Exchange coupling between Co layers 83

4.3.1 Ferromagnetic Resonance on 4Co/6Cu/10.3Co 85

4.3.2 Ferromagnetic Resonance on 4Co/6Cu/4Co/3Fe 88

4.3.3 Ferromagnetic Resonance on 4Co/10Cu/10Co 91

5. Summary of magnetic properties of fcc Co(001) ultrathin structures 93

Appendix A: Comparison of the face-centered-tetragonal and body-centered-tetragonal coordinate systems 96
Appendix B: Undercoupled microwave cavity 100

List of references 106

List of Tables

2.1 List of (a) single Co layer, (b) Co/Fe layer and (b) multilayer samples 26

4.1 Magnetic properties of Cu/10Co/10Cu/20Au sample at different microwave frequencies 66

4.2 Magnetic properties of single-layered Co(001) samples grown on Cu(001) substrate calculated for an fct coordinate system . . . 69

4.3 Magnetic properties of multilayered samples 86

A.1 Magnetic properties of single-layered Co(001) samples grown on Cu(001) substrate presented in the bct coordinate system . . 104

List of Figures

2.1 Simplified diagram of a Physical Electronics MBE-400 series system 4

2.2 Calculation of the path difference between two atomic scatterers . 8

2.3 The fcc (001) plane shown in (a) the real space and (b) the reciprocal space 10

2.4 Ewald's construction for diffraction from a 2-D mesh 12

2.5 Incident and scattered electron beam trajectories and the corresponding RHEED pattern created on the fluorescent screen 13

2.6 Ewald's construction for a finite 2-D mesh. 15

2.7 Schematic view of the cross section of the surface atoms for the two atomic layer system 16

2.8 The reciprocal rods for surfaces with (a) large extended terrace (b) randomly distributed terraces of average size L 19

2.9 Schematic picture of the RHEED pattern for the incident beam along the <100> azimuth of the fcc Cu(001) surface 21

2.10 Models for a perfect and a quasi layer-by-layer growth modes . 22

2.11 RHEED oscillations for a perfect layer-by-layer growth mode with the anti-Bragg condition φ=(odd integer)π 23

2.12 Schematic side view of the layered structures 27

2.13 RHEED patterns of a Cu(001) surface and a Co(001) film 29

2.14 RHEED oscillations during the growth of Co and Cu 31

2.15 Schematic side view of the Cu(001) substrate and the tetragonally distorted fcc Co(001) film 32

3.1 The coordinate system for FMR 37

3.2 Geometry of the parallel configuration of FMR 41

3.3 Ultrathin film of N atomic layers with n atoms in each layer 44

3.4 The demagnetizing field in the parallel configuration 53

3.5 Block diagram of the FMR apparatus 58

3.6 Microwave cavity used in the parallel configuration at 36GHz . . 60

3.7 An example of the FMR signal along the easy axis in the 4Co/6Cu/20Au sample (36.3 GHz, RT) 61

4.1 The FMR signals for 4Co/6Cu/20Au sample (36.3 GHz, RT) . . . 64

4.2 The plot of ΔH vs f for the 10 ML Co sample 67

4.3 The in-plane angular dependence of the FMR field for the 4.3Co/6Cu/4Co sample 70

4.4 The perpendicular uniaxial anisotropy as a function of thickness of Co(001) film for (a) 77 K and (b) 300 K 74

4.5 The fourfold in-plane anisotropy as a function of thickness of Co(001) film for (a) 77 K and (b) 300 K 75

4.6 FMR signals in the 4Co/6Cu/10.3Co sample along the (a) easy and (b) hard magnetic axes (36.3 GHz and T=300 K) and their corresponding calculated FMR lines (c) and (d) 87

4.7 FMR signal along the easy axis in the 4Co/6Cu/4Co/3Fe film . . . 90

4.8 FMR signal along the easy axis in the 4Co/10Cu/10Co film 91

B.1 View of the Co(001) surface 100

Chapter 1

Introduction

Ultrathin magnetic metallic structures grown by means of the Molecular Beam Epitaxy (MBE) technique have become important in the study of material science. A variety of interesting systems have emerged in the past decade. One of them is fcc Co(001) which is a metastable structure stabilized at low temperatures by growing the Co film on a Cu(001) surface template [1.1]. Though much attention has been given to studies of the growth and electronic state properties of this system, relatively little is known about its basic magnetic properties. This thesis provides a detailed account of the magnetic properties of single fcc Co(001) ultrathin layers, and presents magnetic studies of several trilayer samples consisting of two ultrathin layers of fcc Co(001) separated by a layer of fcc Cu(001) .

Ultrathin magnetic films of 3d transition metals exhibit unique magnetic properties. Since ultrathin structures contain only a few atomic layers their growth must be characterize precisely. Such important aspects as the preparation of the substrate, the anealing temperature, the growth temperature, the thickness of the film and the surface structure during the growth need to be addressed.

The growth and tools used for the structural characterization are discussed in Chapter 2. The Molecular Beam Epitaxy technique allows one to produce clean ultrathin films having sharp interfaces. In most cases, films having reproducible properties can be grown using the same growth conditions. Reflection High Energy Electron Diffraction (RHEED) patterns and RHEED intensity oscillations were used to determine the quality of the film growth.

Chapter 3 is devoted to the ferromagnetic resonance (FMR) technique. The power of ferromagnetic resonance is explained, and it is shown that this technique can be used to determine the basic magnetic properties of fcc Co(001).

In Chapter 4 the experimental results are reported and discussed. The measurements on the single Co layers are used to extract their basic magnetic properties. Trilayer structures consisting of two Co magnetic layers separated by a non-ferromagnetic Cu interlayer are used to determine the exchange coupling between the cobalt layers.

Chapter 2

Growth of Metastable fcc Co(001) Ultrathin Structures

2.1 Introduction

At room temperature cobalt has a hexagonal close packed (hcp) structure with the base lattice parameter of 2.507 Å and the c-axis spacing of 4.069 Å. The fcc structure is stable at temperatures over 750K with the bulk lattice constant whose cube edge is 3.548 Å. Fcc Co(001) can be stabilized at low temperatures by depositing Co atoms on an fcc Cu(001) single crystal substrate. In this work the MBE technique was used to grow fcc Co(001) ultrathin films. The surface of the bulk Cu crystal, having a lattice spacing of 3.615 Å, acts as a template for the Co atoms. The lattice mismatch of 1.8% between the bulk fcc Co and Cu is sufficiently small that the deposited Co atoms follow the in-plane spacing of the fcc Cu template. In the direction perpendicular to the Co film surface the lattice spacing is reduced from $(3.615/2)$Å so that the Co lattice can be described as a tetragonally distorted fcc structure [2.1].

2.2 Molecular Beam Epitaxy apparatus

Epitaxial growth of the ultrathin films was carried out in a Physical Electronics (Φ) MBE-400 system. The layout of this system is shown in Figure 2.1. The system consists of two interconnected ultrahigh vacuum chambers: the analysis chamber and the growth chamber. The copper substrate was mounted on a molybdenum holder and inserted into an

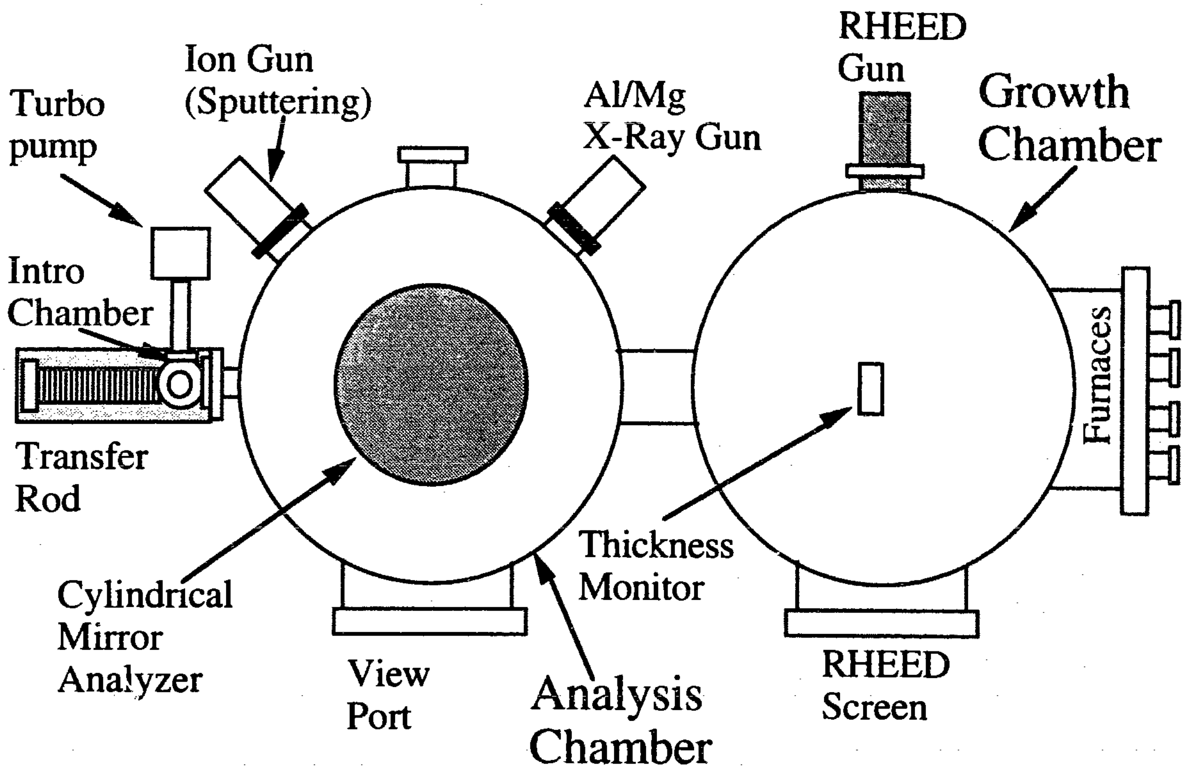

Figure 2.1. Simplified diagram of a Physical Electronics MBE-400 series system.

introductory chamber (intro chamber). The introductory chamber was held at a low 10^{-6} Torr pressure by means of a turbomolecular pump. The intro chamber was sealed off from the rest of the MBE machine by means of a pneumatic valve. In order to insert the substrate, the intro chamber was back filled with a dry N_2. Then the sample was attached to the transfer rod. The chamber was closed and the nitrogen was pumped out by means of the turbo pump. The end of the transfer rod was then driven by an electric motor from the intro chamber into the analysis chamber through a teflon seal and a pneumatic valve.

The analysis chamber was used for the substrate preparation. The substrate was cleaned at room temperature by sputtering with an Ar^+ ion beam from an Ar^+ gun. The end of the transfer arm which housed the substrate holder could be tilted towards the Ar^+ ion gun. During the sputtering process the MBE machine was filled with argon to ~$5x10^{-5}$ Torr. Some of the argon atoms diffused into the ionization chamber of the gun where they were ionized, accelerated to ~2keV and collimated into a beam which was rastered over the substrate. X-ray Photoemission Spectroscopy (XPS) and Auger Electron Spectroscopy (AES) were used to monitor the elemental composition of the substrate. The AES was particularly useful for monitoring the surface contaminants and atoms from previously grown structures. During the AES measurements the chamber was kept in the low 10^{-10} Torr range by means of an ion pump. The vacuum was monitored by means of ionization gauges.

In AES the high energy electron beam ~2-10 keV impinges on the sample and leads to an inner shell vacancy formation (for example K-shell). The electrons of the ionized atoms which occupy outer energy levels (for example L-shell electrons) can then fill the vacant core level and the residual energy can be given to a third electron either in the same or in a more shallow level. Upon acquiring the kinetic energy in this way, the third electron (called an Auger electron) is ejected from the atom. The residual energy that becomes available as the electron kinetic energy is determined by the atomic electron levels involved in the Auger process. For kinetic energies larger than the work function of the spectrometer, the Auger electrons leave the sample and a fraction of them enters the input aperture aperature of a double pass Cylindrical Mirror Analyzer (CMA). The CMA allows one to obtain the electron energy distribution N(E) of electrons leaving the sample. Each element has unique energy levels, and hence the kinetic energies of the ejected Auger electrons are distinctive for that element and are visible as sharp but small peaks in N(E). The Auger signal can be enhanced by applying a small energy modulation. In this case one monitors the energy derivative of the electron energy distribution, dN(E)/dE. The derivative signal, dN(E)/dE, has significantly enhanced Auger peaks relative to the background. The elemental identification is carried out by comparing the measured dN(E)/dE curves with the set of standard spectra listed in the handbook published by Physical Electronics (Φ) [2.2]. AES allows one to determine the elemental composition of the surface of the substrate (Auger electrons provide information about the composition of the topmost 5-30 Å of the specimen because electron mean free path in solids range from 5-30 Å for electron kinetic energies ranging from ~10 eV to ~1 keV). A detailed description of AES can be found elsewhere [2.3].

The sputtering and annealing process (repetitive sputtering and heating of the sample) was continued until only the substrate atoms were observed in the measured Auger spectra. After a sputtering and annealing cycle, the clean Cu(001) substrate was transferred to the growth chamber. The cryopump in the growth chamber maintained the vacuum in the low 10^{-10} Torr range. The growth chamber housed several evaporation cells which were surrounded by a cryoshroud cooled with liquid nitrogen. The cobalt atoms were evaporated from a fine cobalt wire wound around a tungsten filament. The tungsten filament was heated by means of a dc power supply. A power of ~45 watts was needed to reach a Co deposition rate of ~1 monolayer (ML) per minute. The growth of films was initiated and terminated by means of pneumatic shutters which operated in conjunction with the individual sources. The thickness and structure of deposited films were monitored using an in-situ Reflection High Energy Electron Diffraction (RHEED) system. A magnifying lens was used to focus a small area of the RHEED screen onto a photomultiplier tube in order to follow the intensity of the RHEED specular spot as a function of the film thickness during the growth. The thickness of the films was double-checked using a crystal thickness monitor placed 1 cm above the substrate. The RHEED system was the only tool used for the structural studies and therefore it will be discussed in more detail in the following section.

2.3 Reflection High Energy Electron Diffraction (RHEED).

The Reflection High Energy Electron Diffraction technique provides a reciprocal space image of the sample surface. In RHEED an impinging 10-30 keV electron beam strikes the sample at small angles with respect to the surface, ~1°. The low angle of incidence of the electron beam contributes to the surface sensitivity of RHEED. In order to penetrate 1.8 Å (1 ML of Cu substrate) electrons must travel approximately 100 Å in the sample at an angle of 1°, which is larger than the inelastic mean free path of electrons (50 Å at 10keV). Hence, in such a configuration, the elastically scattered electrons originate only from the top atomic surface layer. This surface sensitivity allows one to continuously monitor the structure of the grown overlayers.

2.3.1 Kinematic approximation.

In the following the kinematic approximation will be used to interpret the main qualitative features of RHEED patterns. First, consider just two point scatterers separated by vector $|\mathbf{r}| = AD$ (see Figure 2.2). In order for a constructive interference to occur the path difference between the two rays scattered by each of the atoms must be an integral number of wavelengths. From Figure 2.2 the path difference is AC-BD. If we call the unit vector along the incoming rays $\hat{\mathbf{k}}_i$, and the unit vector along the scattered rays $\hat{\mathbf{k}}_f$,

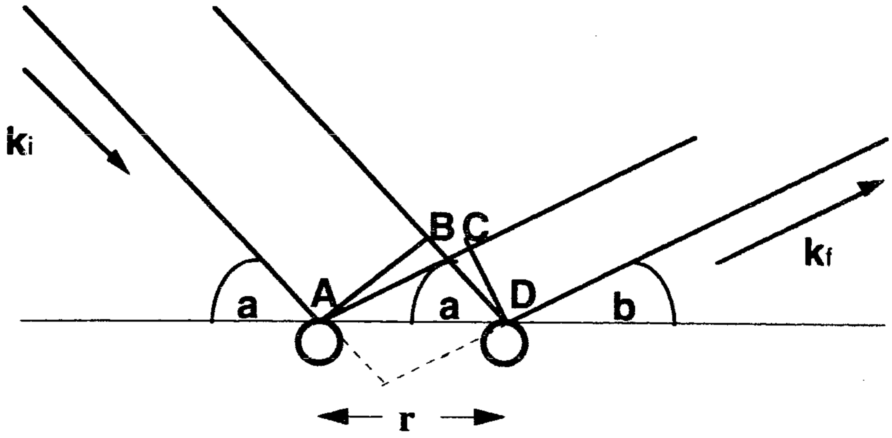

Figure 2.2 The calculation of the path difference between two atomic scatterers.

then the condition for constructive interference can be written as follows

$$\mathrm{AC} - \mathrm{BD} = \mathbf{r} \bullet \hat{\mathbf{k}}_f - \mathbf{r} \bullet \hat{\mathbf{k}}_i = m\lambda \tag{2.1}$$

where m is an integer and λ is the wavelength of the impinging electrons. Multiplying by 2π/λ yields

$$\mathbf{r} \bullet \left(\mathbf{k}_f - \mathbf{k}_i\right) = \mathbf{r} \bullet \mathbf{K} = 2\pi m \tag{2.2}$$

where $\mathbf{k}_i = \frac{2\pi}{\lambda}\hat{\mathbf{k}}_i$, $\mathbf{k}_f = \frac{2\pi}{\lambda}\hat{\mathbf{k}}_f$ are the incident and scattered wave vectors, and $\mathbf{K} \equiv \mathbf{k}_f - \mathbf{k}_i$ is the scattering wavevector. If we consider not just two point scatterers, but an infinite 2-D array of point scatterers, then the above condition must be hold for all vectors $\mathbf{r} = \mathbf{R} = n_1\mathbf{a}_1 + n_2\mathbf{a}_2$ of the atomic mesh, where n_1, n_2 are integers and $\mathbf{a}_1$ and $\mathbf{a}_2$ are the in-plane primitive lattice vectors. In order that equation (2.2) is satisfied for any in-plane vector **R**, the scattering wavevectors, **K**, must be equal to the reciprocal lattice vectors, **G**, of the 2-D atomic mesh [2.4]:

$$\mathbf{K} = \mathbf{G} \tag{2.3}$$

Note that the condition (2.2) is satisfied for any value of the scattering wavevector in the direction perpendicular to the surface, $\mathbf{K}_{\perp}$. Therefore, it follows that the reciprocal space of the 2-D atomic mesh consists of rods perpendicular to the sample surface and originating at those discrete reciprocal lattice points which are generated by the two in-plane basis vectors $\mathbf{b}_1$ and $\mathbf{b}_2$:

$$\mathbf{b}_1 = 2\pi \frac{\hat{\mathbf{c}} \times \mathbf{a}_1}{|\mathbf{a}_1 \times \mathbf{a}_2|} \quad \text{and} \quad \mathbf{b}_2 = 2\pi \frac{\mathbf{a}_2 \times \hat{\mathbf{c}}}{|\mathbf{a}_1 \times \mathbf{a}_2|} \tag{2.4}$$

where $\hat{\mathbf{c}}$ is a unit vector normal to the surface. In mathematical terms the reciprocal lattice space is described by the vector $\mathbf{G}$ of the form:

$$\mathbf{G} = m_1\mathbf{b}_1 + m_2\mathbf{b}_2 + p\hat{\mathbf{c}} \tag{2.5}$$

where m_1 and m_2 are integers, p is an arbitrary number in Å^{-1} and $\hat{\mathbf{c}}$ is a unit vector normal to the surface. The normal component of scattering wavevector , $\mathbf{K}_{\perp}$, is found from energy conservation in elastic scattering:

$$|\mathbf{k}_f| = |\mathbf{k}_i| \tag{2.6}$$

The ideal (001) surface of the fcc lattice can be viewed as a square atomic mesh having the in-plane lattice vectors $\mathbf{a}_1 = \frac{a\sqrt{2}}{2}\hat{\mathbf{i}}$ and $\mathbf{a}_2 = \frac{a\sqrt{2}}{2}\hat{\mathbf{j}}$, where $\hat{\mathbf{i}}$ and $\hat{\mathbf{j}}$ are the unit vectors parallel to the sides of a square (see Figure

Figure 2.3. (a) The fcc (001) plane shown in real space. The plane can be viewed as a square mesh whose unit cell is shown by the dashed lines. The base of the fcc lattice cube is shown as a solid line. Throughout this thesis all the references to the directions in the real space are with respect to the fcc lattice as shown in the figure.

(b) The reciprocal space consists of rods perpendicular to the surface which are located on the square mesh of side $\frac{2\sqrt{2}\pi}{a}$. The square outlined by the broken line indicates the unit cell. The convention for numbering rods in the reciprocal space used in this thesis is indicated in the figure.

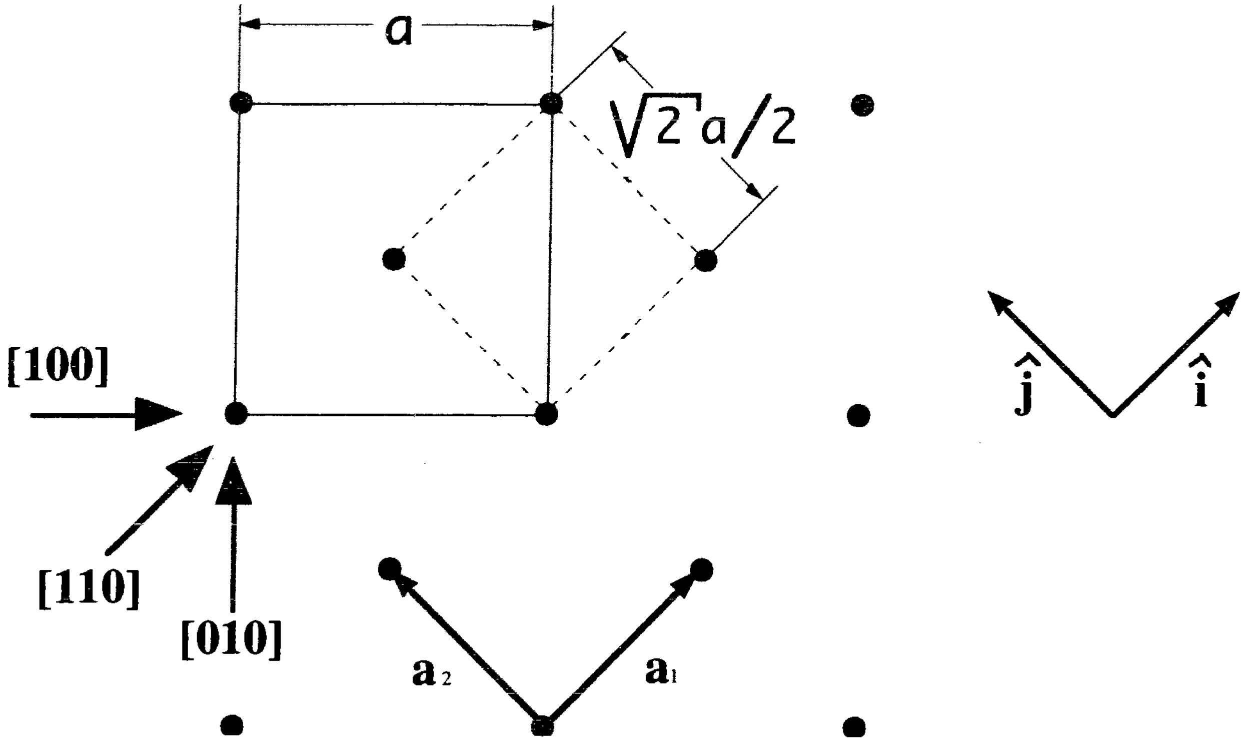
a
$\sqrt{2}a/2$
[100]
[110]
[010]
$\mathbf{a}_2$
$\mathbf{a}_1$
$\hat{\mathbf{j}}$
$\hat{\mathbf{i}}$

(a)

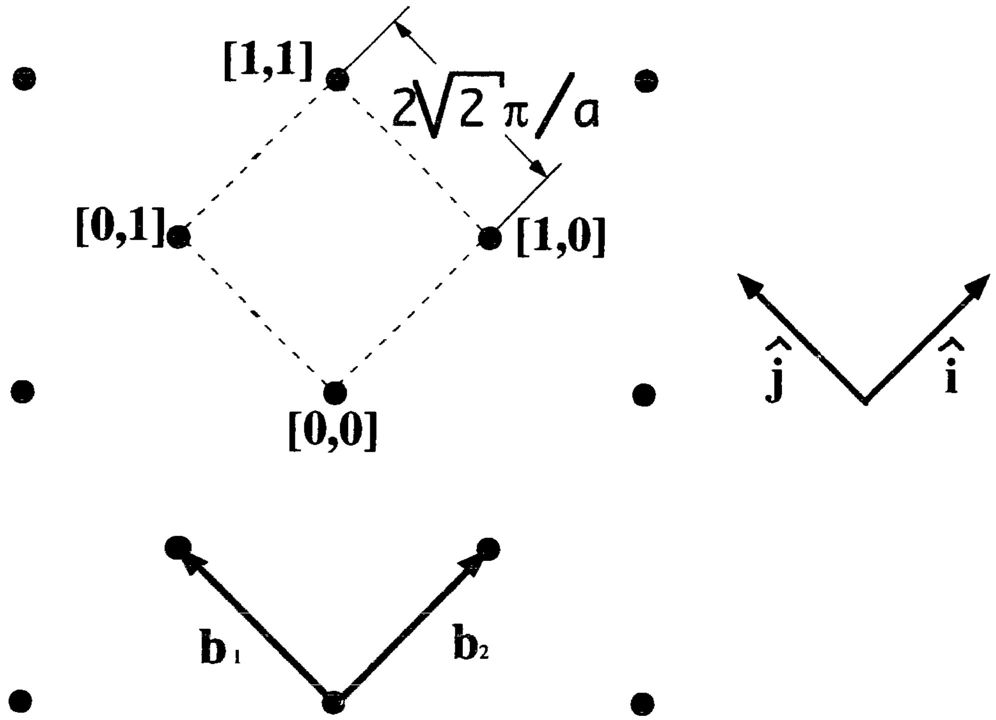
[1,1]
$2\sqrt{2}\pi/a$
[0,1]
[1,0]
[0,0]
$\hat{\mathbf{j}}$
$\hat{\mathbf{i}}$
$\mathbf{b}_1$
$\mathbf{b}_2$

(b)

2.3 (a)). The reciprocal space consists of lines going through the discrete points of a square mesh spanned by the in-plane basis vectors: $\mathbf{b}_1 = \frac{2\sqrt{2}\pi}{a}\hat{\mathbf{j}}$ and $\mathbf{b}_2 = \frac{2\sqrt{2}\pi}{a}\hat{\mathbf{i}}$, see Figure 2.3 (b).

2.3.2 The Ewald construction.

The Ewald construction is a simple geometric construction that allows one to visualize elastic scattering in RHEED, see Figure 2.4. If we draw the wavevector $\mathbf{k}_\mathrm{i}$ of the incident electron in the k-space such that its tip is pointing to the origin of the reciprocal lattice, then a sphere centered on the starting point of $\mathbf{k}_\mathrm{i}$ and having a radius $|\mathbf{k}_\mathrm{f}| = |\mathbf{k}_\mathrm{i}|$ will intercept the reciprocal lattice rod. For example for the 10 keV incident electron beam the Ewald sphere having a radius $|\mathbf{k}_i| = \frac{\sqrt{2mE}}{\hbar} \approx 52\text{Å}^{-1}$ is sufficiently large to intercept the reciprocal rods of the fcc (001) surface having a spacing of $\frac{2\sqrt{2}\pi}{a} \approx 2.5\mathring{A}^{-1}$ along the <110> direction if the angle of incidence is greater than 2.8°. The scattered electron beam wavevectors $\mathbf{k}_\mathrm{f}$ are obtained by connecting the center of the sphere with these intercepts, see Figure 2.4.

The scattered beams form an image on the phosphorescent screen as shown in Figure 2.5. The bright spot in the shadow of the fluorescent screen is a part of the incident beam which misses the sample. The intense specular spot corresponds to the intercept of the Ewald sphere with the [0,0] reciprocal rod. Inelastic scattering creates a bright background in the upper part of the screen: the presence of the opaque sample produces a distinct shadow on the screen.

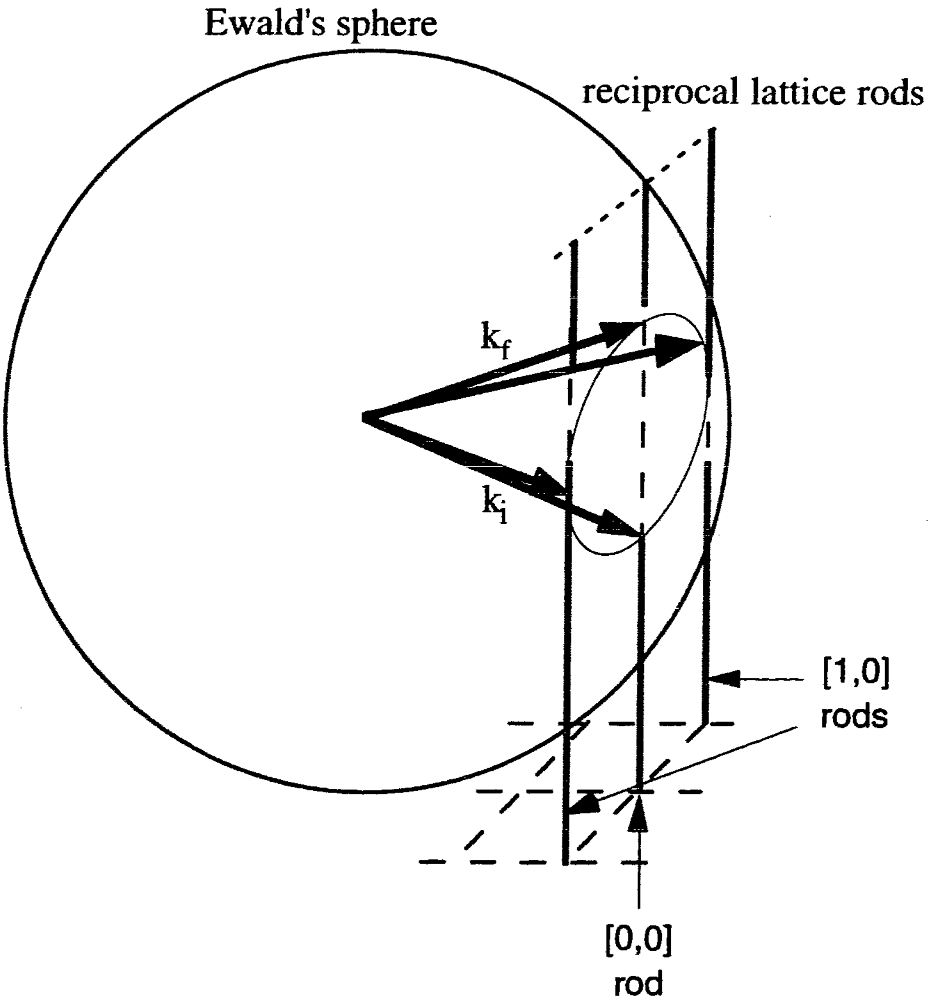

Figure 2.4. The Ewald construction for the diffraction from the square 2-D mesh. Only the first row of reciprocal rods is shown.

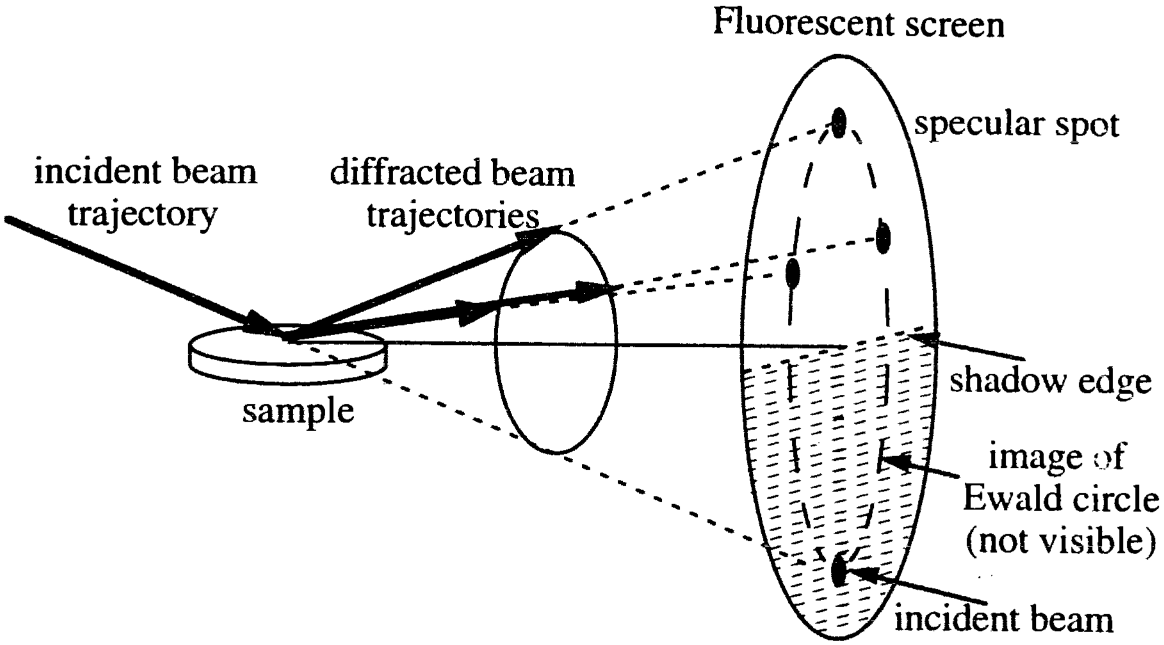

Figure 2.5 Incident and scattered electron beam trajectories obtained from Ewald construction and the corresponding RHEED pattern created on the phosphorescent screen. Only the beams which hit the screen are shown.

2.3.3 RHEED Intensities for Point Scatterers.

So far the discussion is valid for a perfect infinite 2-D lattice. MBE growths are rarely perfect. The real surfaces are not represented by infinite planes but contain atomic terraces having finite dimensions. Therefore, it is interesting to investigate the role of atomic terraces on RHEED. The simplest picture can be obtained by using a single atomic terrace containing N×N atoms. The scattering amplitude, f(**K**), is proportional to the Fourier Transform of the scattering potential, U(**r**), [2.5]:

$$\mathrm{f}(\mathbf{K}) = \frac{1}{4\pi} \int_{\text{sample}} e^{-i\mathbf{K}\bullet\mathbf{r}'} \cdot U(\mathbf{r}') \cdot d\mathbf{r}' \tag{2.7}$$

where $\mathbf{K} = \mathbf{k}_f - \mathbf{k}_i$ is the scattering wavevector. In the simplest case the scattering potential, U(**r**), can be represented by a sum of delta functions:

$$U(\mathbf{r}) \propto \sum_{\mathbf{R}} \delta(\mathbf{r} - \mathbf{R})\delta(z) \tag{2.8}$$

where $\mathbf{R}=n_1\mathbf{a}_1+n_2\mathbf{a}_2$ is the in-plane lattice vector, and n_1, n_2 are integers limited by the size of the terrace: $1<n_1<N, 1<n_2<N$. The Fourier Transform of the potential in equation (2.8) gives:

$$f(\mathbf{K}) \propto \sum_{\mathbf{R}} e^{-i\mathbf{K}\bullet\mathbf{R}} = \sum_{n_1=1}^{N} e^{-i\mathbf{K}\bullet n_1\mathbf{a}_1} \sum_{n_2=1}^{N} e^{-i\mathbf{K}\bullet n_2\mathbf{a}_2} \tag{2.9}$$

This expression can be evaluated using simple algebra. The square mesh of the ideal fcc (001) surface (shown in Figure 2.3 (a)) is used as an example, but the discussion is similar for any surface. The intensity of the scattered beams, $I(\mathbf{K}) \propto |f(\mathbf{K})|^2$, is given by:

$$I(\mathbf{K}) = |f(\mathbf{K})|^2 = \frac{\sin^2\left(\frac{1}{2}N|\mathbf{K}_x||\mathbf{a}_1|\right)}{\sin^2\left(\frac{1}{2}|\mathbf{K}_x||\mathbf{a}_1|\right)} \cdot \frac{\sin^2\left(\frac{1}{2}N|\mathbf{K}_y||\mathbf{a}_2|\right)}{\sin^2\left(\frac{1}{2}|\mathbf{K}_y||\mathbf{a}_2|\right)} \tag{2.10}$$

where $\mathbf{K}_x$ and $\mathbf{K}_y$ are the components of **K** parallel to $\mathbf{a}_1$ and $\mathbf{a}_2$, respectively. For a perfect infinite surface the $\dfrac{\sin^2\left(\frac{1}{2}N|\mathbf{K}_j||\mathbf{a}_i|\right)}{\sin^2\left(\frac{1}{2}|\mathbf{K}_j||\mathbf{a}_i|\right)}$ terms converge to delta functions peaked at $K_x = \dfrac{2\pi}{|\mathbf{a}_1|}m_1, K_y = \dfrac{2\pi}{|\mathbf{a}_2|}m_2$ where m_1

and m_2 are integers and K_z is arbitrary. This corresponds to the reciprocal lines for an infinite plane described in Section 2.3.1. For finite dimensions the positions of the rods do not change; however, the intensity is broadened in the $\mathbf{K}_x$ and $\mathbf{K}_y$ directions. The width, w, of the rod is given by the terrace size L, $w = \frac{2\pi}{L}$, where L=N|a|. From the RHEED geometry, see Figure 2.6,

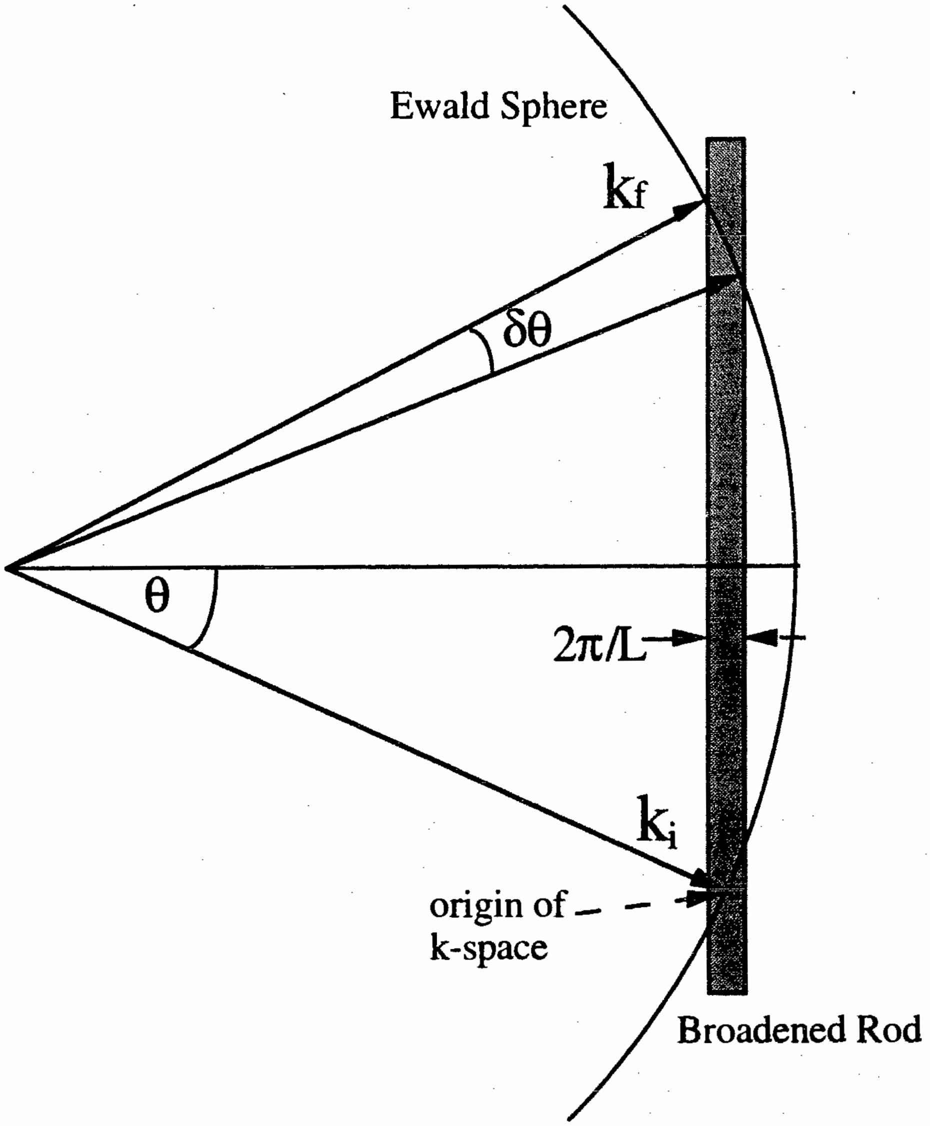

Figure 2.6. Ewald construction for a finite 2-D mesh whose rods have a finite width in k-space.

one can see that the intersections of the rods with the Ewald sphere become broadened. The broadening is asymmetric. It is significantly wider in the direction of the reciprocal rods (perpendicular to the shadow edge). The width of the scattered specular beam, S, along the reciprocal rod is inversely proportional to sin θ:

$$S \approx \frac{2\pi}{L \cdot \sin\theta} \tag{2.11}$$

where θ is the angle of the incident beam to the sample surface. The width, W, perpendicular to the reciprocal rod is:

$$W \approx \frac{2\pi}{L} \tag{2.12}$$

For small angle of incidence $\theta \approx 1^\circ$ ($\sin 1^\circ \approx 0.01745$) the ratio $S/W \approx 60$ which leads to a streaky pattern if L is small enough.

The above discussion was limited to one single atomic terrace. Real surfaces consist of atomic terraces separated from each other by atomic steps. In the simplest case one can consider a two atomic layer surface for which the top atomic layer is partially covered, and one atomic layer below is fully covered, see Figure 2.7.

Figure 2.7. Schematic view of the cross section of the surface atoms of the atomic layer system.

Assuming that the intensity of the specular spot is given by the scattering from uncovered atoms only, see Figure 2.7, equation (2.9) can be rewritten as follows (for a surface having only two levels):

$$\begin{aligned} f(\mathbf{K}) &\propto \sum_{\mathrm{R}} e^{-i\mathbf{K}\bullet\mathbf{R}} = \sum_{\text{uncovered part of filled layer}} e^{-i\mathbf{K}\bullet\mathbf{R}_{2\text{-D}}} + \sum_{\text{top layer}} e^{-i\mathbf{K}\bullet\mathbf{R}_{2\text{-D}}} \cdot e^{-i\mathbf{K}\bullet c\cdot\hat{\mathbf{c}}} \\ &\propto \eta + (1-\eta)\cdot e^{-i\varphi} \end{aligned} \tag{2.13}$$

where η is the fractional coverage of the top layer, c is the spacing between layers and $\hat{\mathbf{c}}$ is the vector normal to the surface. Equation (2.13) is exact for a surface whose terraces have dimensions much larger than the lattice constant [2.6]. For a surface whose terraces have a wide range of sizes equation (2.13) is only approximate, but it can still be used to discuss the intensity in a qualitative manner. Surfaces having randomly distributed terrace sizes are discussed in detail by Pukite [2.6].

Equation (2.13) represents a simple kinematic interference. The phase difference φ between the incident and the specular beam is given by:

$$\varphi = \mathbf{K} \bullet c\hat{\mathbf{c}} = \mathbf{K}_{\perp} c = 2k_i c \sin\theta \tag{2.14}$$

The intensity I of the specular beam which follows from (2.13) is

$$\mathrm{I} \propto \left|\eta + (1-\eta)\cdot e^{-i\varphi}\right|^2 = \eta^2 + (1-\eta)^2 + 2\eta(1-\eta)\cos\varphi \tag{2.15}$$

The perpendicular scattering wavevector $\mathbf{K}_{\perp}$ and the corresponding phase angle φ can be continuously adjusted by changing the incident angle θ, see equation (2.14). For the Bragg conditions φ=(*even integer*)π the intensity of the specular beam for the two atomic layer surface is $I \propto 1$ and is therefore indistinguishable from that of a single atomic layer surface (one large terrace without steps). But for other incident angles the intensity of the specular spot depends on the presence of terraces. The intensity decreases and reaches a minimum $I \propto (2\eta - 1)^2$ for the anti-Bragg condition, φ=(*odd integer*)π. In a simple kinematic theory the total number of scattered electrons depends only on the number of scatterers in the surface. It follows that a decreased intensity in the center of the specular beam (φ=(*even integer*)π) leads to an increased intensity of the diffracted electrons around the center. The specular beam broadens and results in a streaky specular spot. The scattering in real space is usually represented by the intersection of the Ewald sphere with the reciprocal rods in k-space, as discussed in Section 2.3.2. It turns out that in the case of randomly distributed steps the reciprocal rods are periodically broadened [2.7], see Figure 2.8. The thinnest segments correspond to the Bragg conditions. The thickest segments correspond to the anti-Bragg conditions. The specular spot profile has a Lorenzian-like shape having the width which is given by the intersection of the Ewald's sphere with the [0,0] reciprocal rod [2.7]. The broadening of the reciprocal rod originates in the finite size of terraces (see the treatment of the single terrace above). For randomly distributed terraces the width of the reciprocal rod at the anti-Bragg condition is inversely proportional to the average terrace size $\overline{\mathrm{L}}$ [2.6].

For a 10 keV RHEED incident beam the Bragg and anti-Bragg conditions can be adjusted by changing the angle of incidence, θ, in the

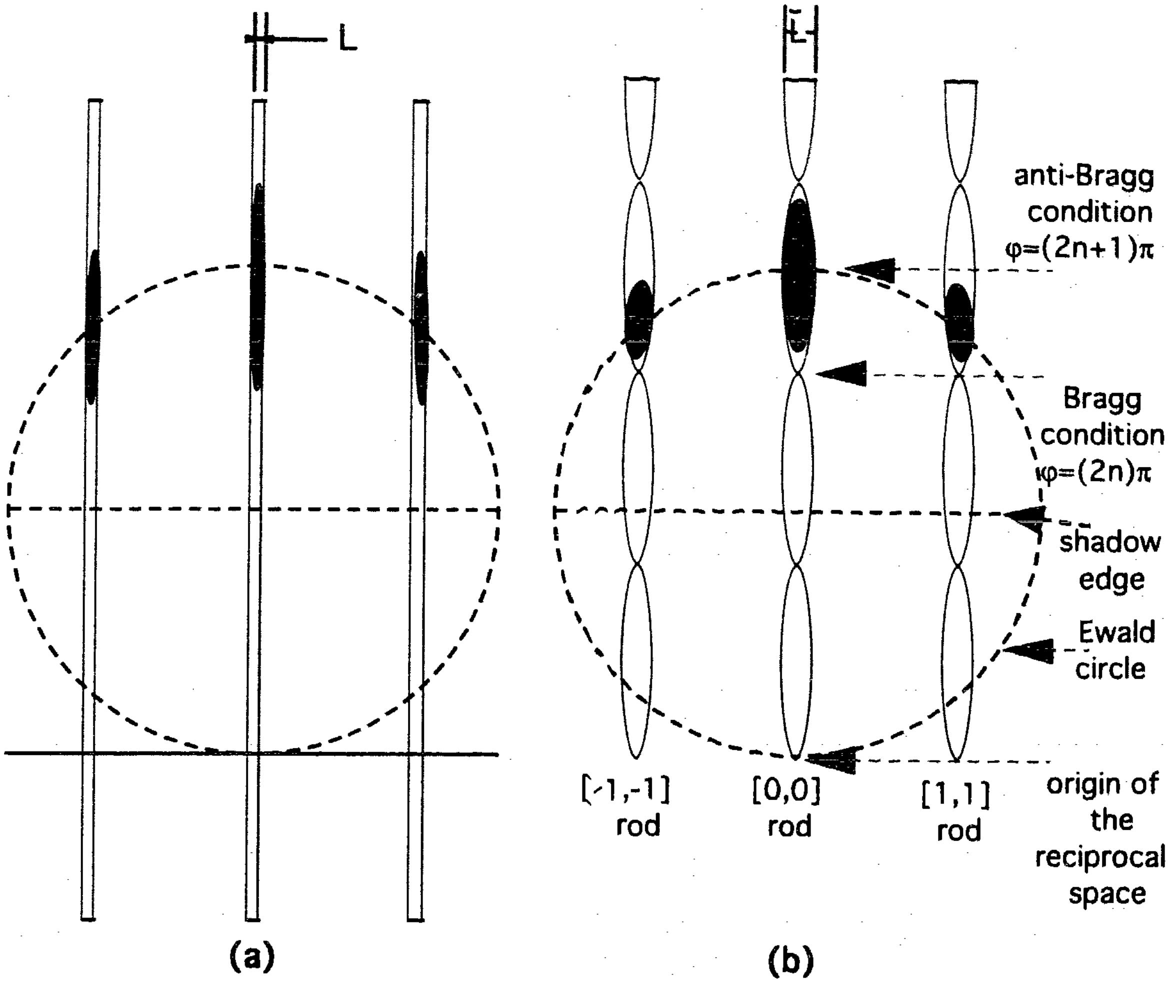

Figure 2.8 The reciprocal rods for surfaces with (a) large extended terrace of size L (perfectly flat surface) (b) randomly distributed terraces of average size $\overline{L}$ (stepped surface); n is an integer. The widths of the rods are exaggerated for the graphical purpose, and hence the intersections of the Ewald sphere with the reciprocal lattice rods are not to scale. Intersections below the shadow edge are not shown.

range of a few degrees. The formula (2.14) which was derived by using a simple kinematic approach can be employed only as a guideline. Dynamic aspects of the electron scattering play a significant role in RHEED. The Bragg and anti-Bragg conditions are usually found experimentally by monitoring the strength of RHEED intensity oscillations as a function of the incident angle (discussed in the next section).

A schematic drawing of a RHEED pattern for the incident beam along the <100> azimuth of the fcc Cu(001) surface at the anti-Bragg condition is shown in Figure 2.9. The position of RHEED streaks and their widths are given by the intersection of the Ewald's sphere with the reciprocal rods, see above. The separation, ρ, between the streaks is proportional to the separation between the reciprocal lattice rods along the <100> azimuth, $\frac{4\pi}{a}$,

$$\rho = \mathrm{C}\frac{4\pi}{a}; \tag{2.16}$$

and the width, σ, of the specular streak is given by

$$\sigma = \mathrm{C}\frac{2\pi}{L\sin\theta} \quad \text{(see equation 2.11)}, \tag{2.17}$$

where C is a common geometrical factor which depends on the distance between the sample and the fluorescent screen. From the above equations the average terrace size, $\bar{L}$, is given by:

$$\bar{L} \approx \frac{a\cdot\rho}{2\cdot\sigma\cdot\sin\theta} \tag{2.18}$$

where a is the fcc Cu lattice parameter.

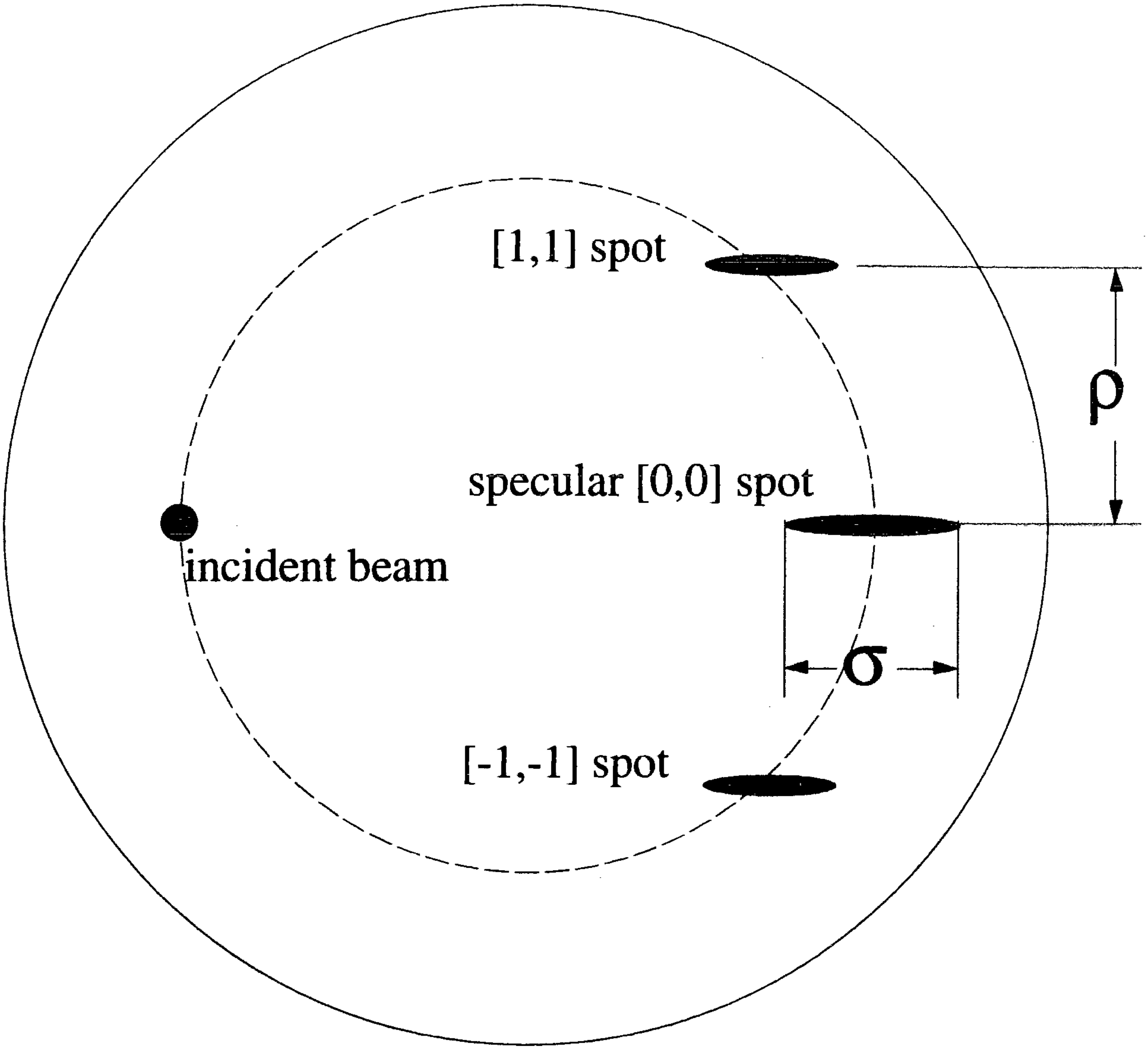

Figure 2.9 Schematic picture of the RHEED pattern for the incident beam along the <100> azimuth of the fcc Cu(001) surface.

2.3.4. RHEED intensity oscillations.

Equation (2.15) shows that for the anti-Bragg condition the intensity of the specular spot can be expected to oscillate with the degree of coverage. Consider a simple picture in which the growth can be described by a layer-by-layer growth, see Figure 2.10.

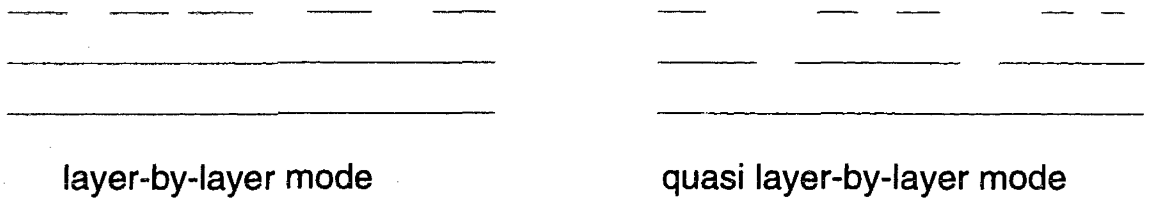

Figure 2.10. Models for the growth modes discussed in the text. Lines indicate rows of atoms.

The layer-by-layer mode refers to a growth in which the add-atoms fill all the voids before a new atomic layer is nucleated. It means that only the top atomic layer is partially filled. In that case the intensity of the specular spot is proportional to the expression given by equation (2.15). For Bragg conditions $\varphi=(\textit{even integer})\pi$ the intensity of the specular beam does not change during the growth. For other incident angles the intensity of the specular spot oscillates during the deposition. Oscillations consist of repeatable parabolas with maxima corresponding to a completely filled layer ($\eta=1$) and minima corresponding to a half filled layer ($\eta=0.5$). For anti-Bragg conditions $\varphi=(\textit{odd integer})\pi$ the oscillations are most pronounced, see Figure 2.11. For less perfect growths in which the top two atomic layers can be partially filled the RHEED oscillations are still observable, but the cusps illustrated in Figure 2.11 are not pronounced and the oscillations have a sinusoidal-like behavior. For growths in which the last three layers exhibit appreciable partial coverage the RHEED intensity oscillations converge rapidly to zero [2.8]. Therefore, the presence of RHEED oscillations indicates a quasi layer-by-layer growth in which the surface roughness is confined mostly to the top two atomic layers, see Figure 2.10. After several initial oscillations the oscillatory period reaches a stationary value which corresponds to the deposition of one additional atomic layer. The initial oscillations require a longer period of time due to a non-trivial 3-D growth of the first couple of layers: the growth of the second layer starts well before the completion of the first one.

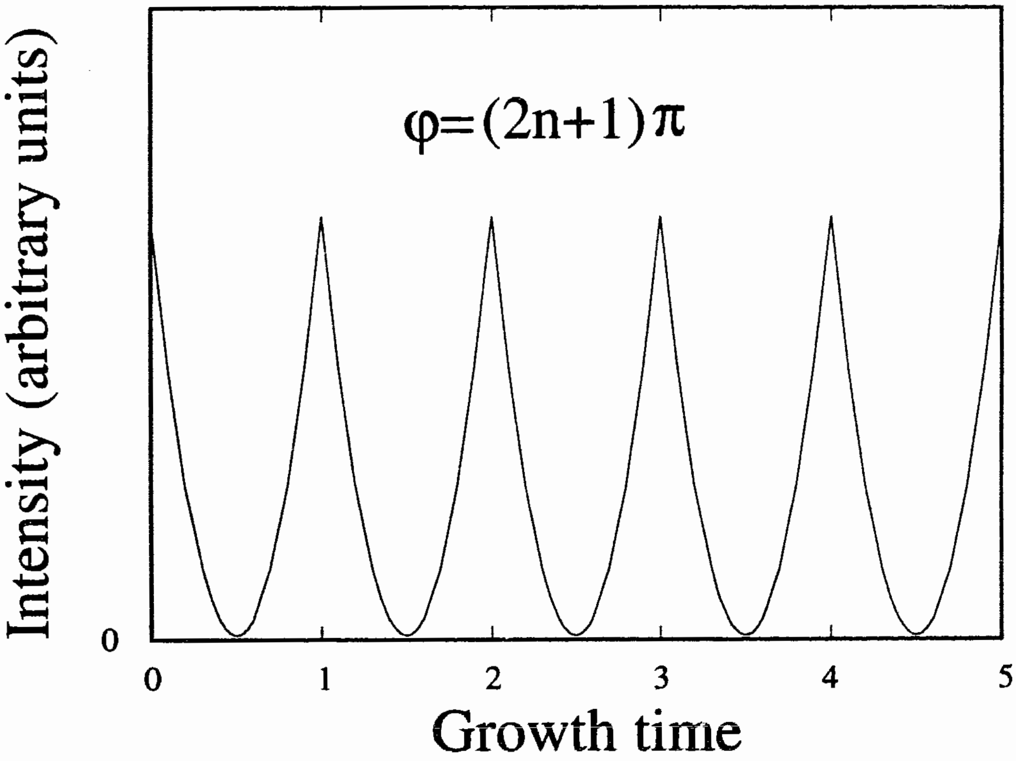

Figure 2.11. RHEED oscillations for a perfect layer-by-layer growth with anti-Bragg condition $\varphi=(2n+1)\pi$, n integer.

2.4 Sample preparation and growth characterization.

2.4.1 Preparation of the fcc Cu(001) substrate

The Cu(001) substrate used as a template for the growths of ultrathin films studied in this thesis was prepared by Dr. Kirschner's group, the Freie Universität Berlin, Germany. A single crystal Cu disk, 3 mm thick and 20 mm in diameter, characterized by a mosaic spread of less than 0.1°, was cut so that the [001] crystallographic orientation was within 0.2° of the (001) axis. The Cu crystal was polished using 1 μm diamond paste. After insertion into the Ultrahigh Vacuum System, UHV, the crystal surface was prepared by cyclic sputtering ($V_{ion} = 600eV$, $I_{ion} = 4\mu A/cm^2$, 15 min.) and annealing (1000 K, 10-20 min.). The total cycling time required to obtain an uncontaminated surface with large atomic terraces was approximately five days. After this treatment the surface showed sharp Low Energy Electron Diffraction (LEED) and Reflection High Energy Electron Diffraction (RHEED) patterns and no visible contamination in the Auger electron spectra. In addition, Scanning Tunneling Microscope (STM) micrographs of the Cu(001) templates showed large extended atomic terraces (some up to 200 nm wide), separated by bands of piled-up monatomic steps [2.9].

The Cu(001) crystalline disk was reconditioned before each growth by sputtering for 2 hours at 100 °C to remove the previous structure, followed by 1/2 hour sputtering at 400 °C and then annealing until the temperature reached 650 °C (15-20 min. at $400\ ^\circ C \leq T \leq 650^\circ C$). This procedure resulted in a clean Cu (001) crystal surface which exhibited sharp RHEED streaks.

Due to the sudden deterioration of the copper substrate, after a large number of growths, the Cu(001) had to be revived. A good Cu(001) surface with large extended terraces up to 300 nm was most likely recovered when the following procedure was performed: after sputtering the surface of the substrate at room temperature (V_{ion}=600 eV, I_{ion}=4 μA/cm^2) to remove contaminants the temperature was increased to 900 K and sputtering was continued for 10 hours with voltage and current reduced to 500 eV and 0.1 μA/cm^2, respectively [2.10].

2.4.2 Film preparation and nomenclature

The epitaxial growth of ultrathin fcc Co(001) films was carried out in the Physical Electronics MBE-400 system described in Section 2.2. Each ultrathin layer of fcc Co(001) was grown on the fcc Cu(001) template, covered with a copper layer and a protective gold layer on top, see Figure 2.12(a). A sample containing an additional iron layer between the cobalt and the second copper layers was also grown. Each trilayer structure was grown with two cobalt layers separated by a copper spacer layer and covered by additional Cu and protective Au layers, see Figure 2.12(b). See Tables 2.1 for a list of all samples used in this work. Beams of Cu, Co, Fe or Au were created using a tantalum boat for Cu, a tungsten wire for Fe and Co, and a pyrolytic BN crucible for the Au depositions. Growths were performed at temperatures in the range 330-410 K, see Table 2.1 for the details. The quality of the growth was monitored by means of the RHEED patterns and RHEED intensity oscillations.

Table 2.1 List of a) single Co layer b) Co/Fe layer and c) multilayer samples.

a) Single layer samples	Growth Temperature (K)
1.7 Co / 11.5 Cu / 20 Au	330
3.3 Co / 6 Cu / 20 Au	375
4 Co / 6 Cu / 20 Au	300
6.5 Co / 10.5 Cu / 20 Au	300
8.6 Co / 10.5 Cu / 20 Au	300
10 Co / 10 Cu / 20 Au	355
b) 4 Co / 3 Fe / 8.5 Cu / 20 Au	300
c) Trilayer samples	Growth Temperature (K)
4 Co / 6 Cu / 10.3 Co / 11 Cu / 20 Au	375(4Co) 410(6 Cu) 345(10 Co)
4 Co / 6 Cu / 4 Co / 3 Fe / 6 Cu / 20 Au	300
4.3 Co / 6 Cu / 4 Co / 17 Cu / 20 Au	300
4 Co / 10 Cu / 10 Co / 10 Cu / 20 Au	300

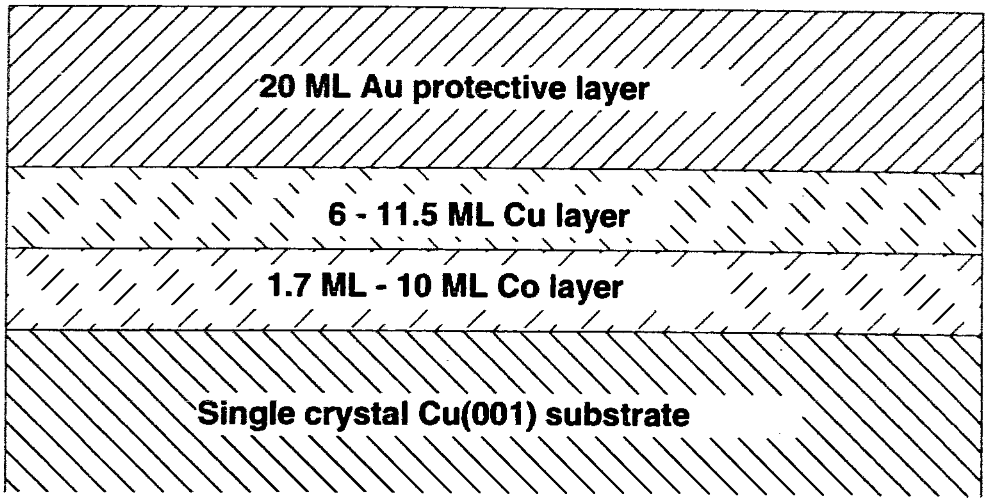

a) Single layer samples

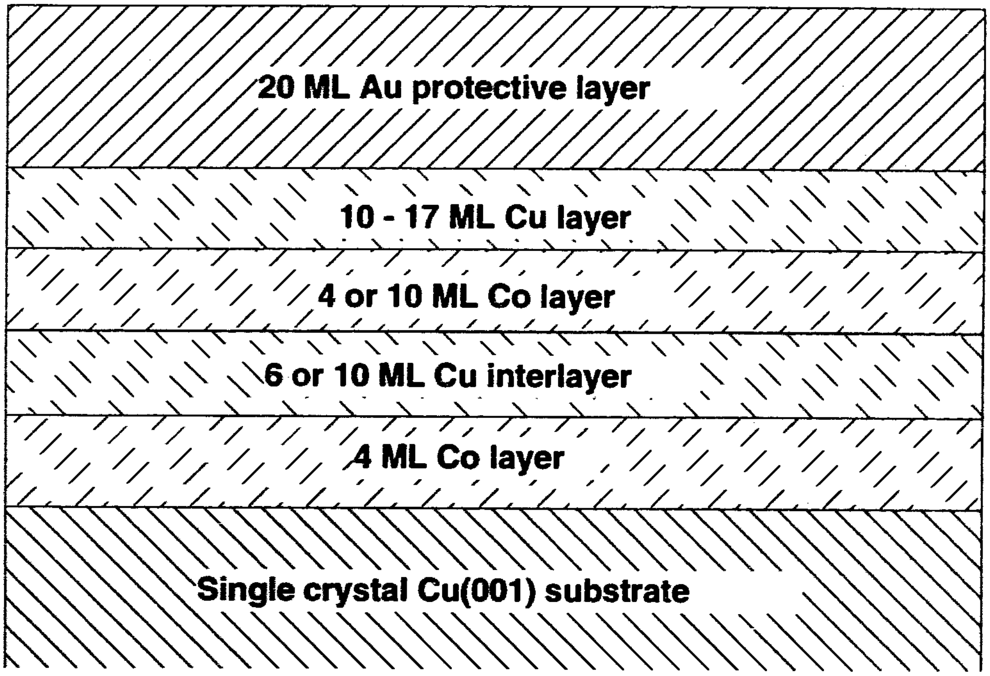

b) Multilayer samples

Figure 2.12. Schematic side view of the layered structures used in this work.

2.4.3 RHEED patterns of the Cu substrate and deposited films

RHEED patterns for the fcc Cu(001) surface are shown in Figure 2.13. The RHEED pattern along the <110> azimuths (of real space) show diffraction streaks corresponding to the intersects of the Ewald sphere with the [1,0] and [2,0] reciprocal rods, see Figure 2.13(a). Along the<100> azimuth only the diffraction spots corresponding to the intersects of the Ewald sphere with the [1,1] reciprocal rods are observable, see Fig. 2.13(b).

One could in principle change the streak profile by varying the incidence angle of the electron beam from the Bragg to the anti-Bragg condition, as shown in Section 2.3.3. This effect was not clearly pronounced for the fcc Cu(001) substrate. The absence of sharp streaks for the incidence angle corresponding to the Bragg condition is caused by the presence of a mosaic spread in the substrate. The widths of the observed streaks suggest that the mosaic spread in our substrate was ~0.15°. This is somewhat larger than the value of 0.1° claimed by Dr. Kirschner's group. It is therefore possible that a part of the observed width was caused by finite size terraces. Detailed angular studies are difficult due to the presence of inelastic scattering (Kikuchi bands) which rapidly changes with the angle of incidence and can strongly affect the apparent width. For that reason a lower bound limit for the terrace size was estimated by using the full width of the streaks. Equation (2.18) leads to the average terrace size $\overline{L} \approx 35$ nm for well prepared Cu substrates, 30 nm for Cu films grown on Co, and 20 nm for Co films grown on Cu, all growths carried out at RT. The RHEED patterns of Co films show that the cobalt overlayer follows the in-plane spacing of the fcc Cu(001) substrate, see Figure 2.13(c).

All samples were covered by an epitaxial layer of Au before being exposed to ambient conditions. Au grows on Cu(001) substrates in the (111)

Figure 2.13. RHEED patterns at the anti-Bragg condition corresponding to the incident beam along (a) the <110> azimuth of the fcc Cu(001) substrate, (b) the <100> azimuth of the fcc Cu(001) substrate, (c) the <110> azimuth of the fcc Co(001) film, and (d) the<100> azimuth of the fcc Co(001) film.

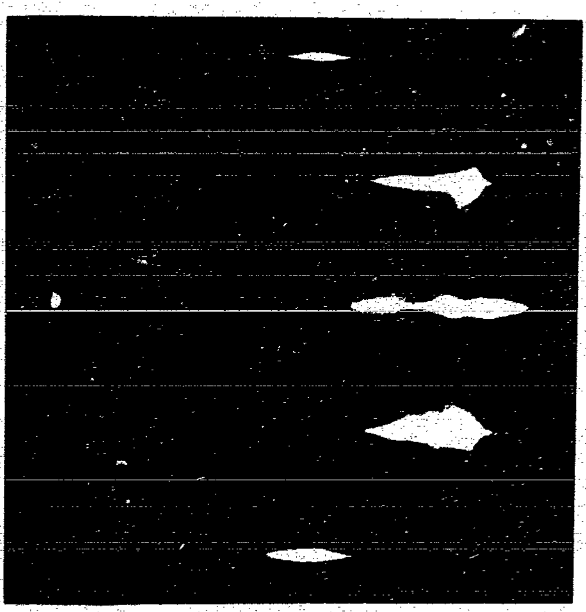

(a)

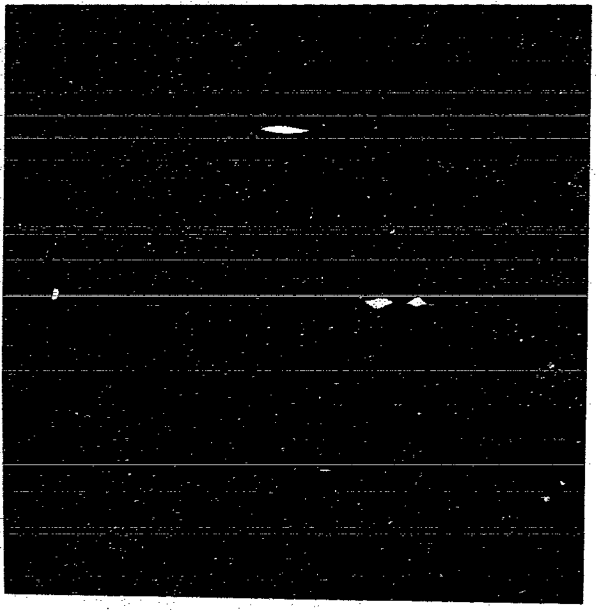

(b)

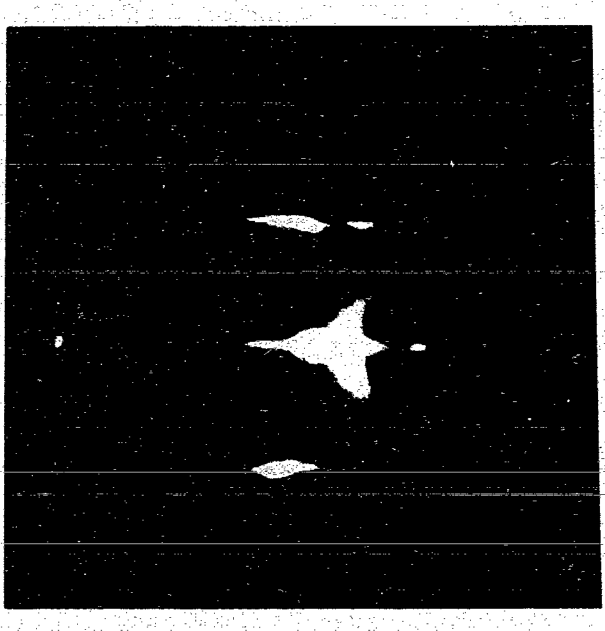

(c)

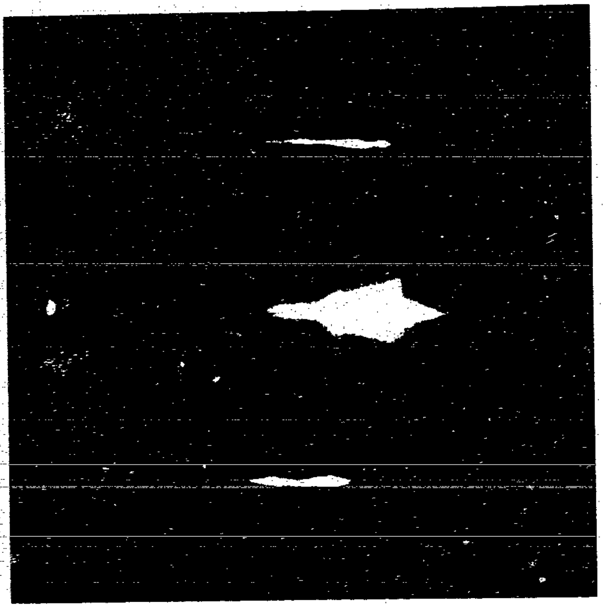

(d)

orientation. There are two nonequivalent orientations of the Au(111) with respect to the Cu(001). These are rotated by 30 with respect to each other. Both orientations repeat every 60° and that results in RHEED patterns characterized by an overall 12 fold in-plane azimuthal symmetry.

2.4.4 RHEED oscillations of Co and Cu.

The growths of Co and Cu exhibited strong sinusoidal like oscillations indicating that the growths proceeded in the quasi layer-by-layer mode (as discussed in Section 2.3.4). The deposition rates were slow, typically ~1 monolayer (ML)/min. The regular periodicity of the RHEED oscillations established the time required to form a full atomic layer. Co layers grown on a Cu substrate acquire a regular periodicity after the second atomic layer. The outer (second) Co film grown on a Cu interlayer establishes a regular RHEED oscillation periodicity after the third atomic layer, see Fig. 2.14. This behavior is caused by the deviation of the growth from the quasi layer-by-layer mode for the first two atomic layers [2.11]. The film thickness determined from the RHEED oscillations was confirmed by using the quartz crystal thickness monitor.

The thicknesses of the individual layers were determined by using the total deposition time divided by the stationary period of oscillations. In our growths either the maxima or the minima of the RHEED oscillations were close to an integral number of ML (within 0.2 ML). That means that the RHEED oscillation phase varied by π from one sample to another. However, the RHEED oscillation phase in many cases remained the same within the given structure; that means that all growths carried out for the same structure reached an integral number of ML either at a RHEED oscillation maximum or at a minimum. For example for the 4Co/6Cu/10.3Co sample the maxima of the intensity oscillations corresponded to an integral number of ML in all three layers, see Figure 2.14. It appears that the RHEED oscillation phase was affected by substrate features, as yet unknown, which changed during the preparation of a new substrate.

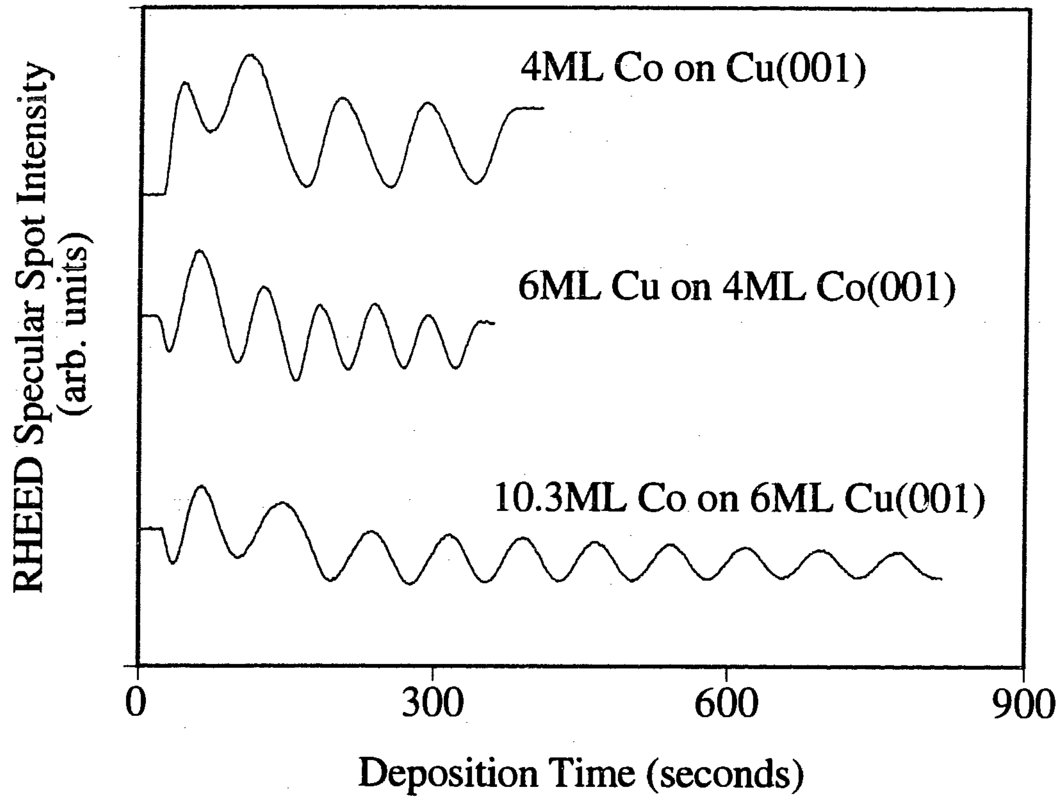

Figure 2.14. RHEED oscillation during the growth of Co and Cu.

2.5 Tetragonal distortion of the fcc Co(001) films

Thermal-Energy Atomic Scattering (TEAS) and Low-Energy Electron Diffraction (LEED) studies [2.12] showed that for the first 10 monolayers (ML) the fcc Co structures grown on Cu (001) substrates have a p(1x1) symmetry with cobalt expanded in the plane of the surface to match the spacing of the Cu(001) template (1.7% expansion with respect to bulk fcc Co). Our RHEED patterns support that view. Detailed LEED investigations in combination with dynamical scattering calculations revealed a changing tetragonal distortion for films 3 ML and thinner [2.1]. Further studies by Extended X-ray Absorption Fine Structure (EXAFS) [2.13], TEAS and LEED [2.12] showed that the vertical compression of 5 ML films and thicker is more or less constant and amounts to ~2.2% with respect to bulk fcc Co (corresponding to a ratio c/a 0.96), see Figure 2.15. Hence, a homogeneous and constant strain due to lattice mismatch is expected for samples between 5-10 ML in thickness. The tetragonal compression along the surface normal has a profound effect on the magnetic properties of Co (001) structures, as will be demonstrated in Chapter 4.

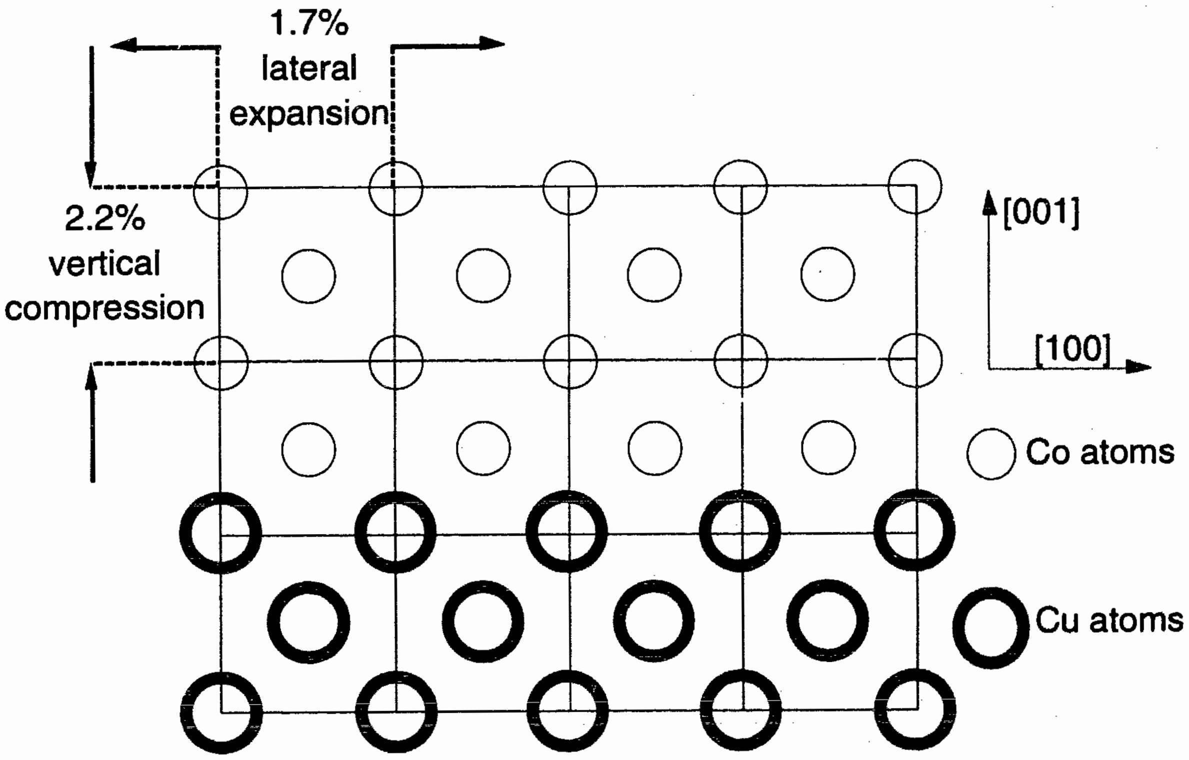

Figure 2.15. Schematic side view of the fcc Cu(001) substrate and the tetragonally distorted fcc Co(001) film.

Chapter 3

FMR Theory for Ultrathin Films

3.1 Introduction

The ferromagnetic resonance (FMR) technique was employed in order to determine the basic magnetic properties of ultrathin Co(001) structures such as the effective demagnetizing fields, the magnetic anisotropies, the spectroscopic splitting factor g, and the Gilbert damping parameter G. Detailed descriptions of FMR can be readily found in works by Gurevich, Urquhart, and Heinrich [3.1, 3.2, 3.3]. The purpose of this chapter is to introduce a quantitative description of FMR which gives a basic understanding of this technique in the ultrathin film limit. Ferromagnetic films are called ultrathin when the film is thin enough so that the exchange interaction locks all of the atomic magnetic moments together across the layer. In an ultrathin film the magnetic moments across the film thickness are parallel and point in one common direction. The film responds to the total torque acting on it like a single, giant magnetic molecule. The effect of a spatially varying exchange field and a quantitative approach to the thin film limit is discussed in detail in reference 3.3.

3.2 Landau-Lifshitz equation of motion for magnetization

In ferromagnetic resonance, the ultrathin ferromagnetic films are subjected to an external dc field and a small alternating magnetic field of microwave frequency ω which is perpendicular to the dc field. The magnetic moments in the thin film precess around the static magnetization due to the ac torque exerted by the ac field. In general, the total magnetic moment is the vector sum of all atomic magnetic moments:

$$\vec{\mathbf{M}}_{total} = \sum_{\text{all atoms i}} \vec{\mu}_i \tag{3.1}$$

where $\vec{\mathbf{M}}_{total}$ is the total magnetic moment and $\vec{\mu}_i$ are the atomic magnetic moments. At saturation, the magnetic moments in an ultrathin film are parallel giving a resultant magnetic moment:

$$M_{total} = \sum_{\text{all atoms i}} \mu_i \tag{3.2}$$

where μ_i is the magnitude of atomic magnetic moments, and the sum is over all atoms in the film. The rate of change of the angular momentum $\mathbf{s}_i$ of an atom is equal to the sum of the torques acting on it. This leads to:

$$\frac{d\mathbf{s}_i}{dt} = \vec{\mu}_i \times \mathbf{H}_{i,eff}^{atom} \tag{3.3}$$

Each atomic magnetic moment responds to its effective field $\mathbf{H}_{i,eff}^{atom}$. The atomic magnetic moment $\vec{\mu}_i$ is related to its angular momentum $\mathbf{s}_i$ by the gyromagnetic ratio, γ, [3.1]:

$$\vec{\mu}_i = -\gamma \mathbf{s}_i \tag{3.4}$$

$$\gamma = \frac{|e|g}{2mc} \tag{3.5}$$

where | e| is the electron charge, g is the spectroscopic splitting factor, m is the electron mass and c is the velocity of light. Substituting (3.4) into equation (3.3) yields:

$$-\frac{1}{\gamma}\frac{d\vec{\mu}_i}{dt} = \vec{\mu}_i \times \mathbf{H}_{i,eff}^{atom} \tag{3.6}$$

which is the Landau-Lifshitz (L-L) equation of motion for a magnetic atom. Summing over all atoms in the film yields:

$$\frac{1}{\gamma}\sum_{i}\frac{d\vec{\mu}_i}{dt} = -\sum_{i}\left[\vec{\mu}_i \times \mathbf{H}_{i,eff}^{atom}\right] \tag{3.7}$$

Since all the magnetic moments in the ultrathin film point in one common direction we can write equation (3.1) as follows:

$$\vec{\mathbf{M}}_{total} = \mathbf{M}V_{total} = \sum_i \vec{\mu}_i = \sum_i \vec{\mathbf{v}}|\vec{\mu}_i| = \vec{\mathbf{v}}\sum_i |\vec{\mu}_i| = \vec{\mathbf{v}}\sum_i \mu_i \tag{3.8}$$

where **M** is the magnetization per unit volume, V_{total} is the film volume, $|\vec{\mu}_i| = \mu_i$ is the atomic magnetic moment and

$$\vec{\mathbf{v}} = \frac{\vec{\mu}_i}{\mu_i} = \frac{\vec{\mathbf{M}}_{total}}{M_{total}} \tag{3.9}$$

is the unit vector pointing in the common direction of the atomic moments in the ultrathin film. Now we can use equations (3.8) and (3.9) to rearrange equation (3.7):

$$\begin{aligned}\frac{1}{\gamma}\frac{d\mathbf{M}_{total}}{dt} &= -\sum_{\mathrm{i}}\left[(\vec{\mathbf{v}}\mu_i)\times\mathbf{H}_{i,eff}^{atom}\right] = -\vec{\mathbf{v}}\times\sum_{\mathrm{i}}\left[\mu_i\mathbf{H}_{i,eff}^{atom}\right] \\ &= -\frac{\mathbf{M}_{total}}{M_{total}}\times\sum_{\mathrm{i}}\left[\mu_i\mathbf{H}_{i,eff}^{atom}\right] = -\mathbf{M}_{total}\times\sum_{\mathrm{i}}\left[\frac{\mu_i}{M_{total}}\mathbf{H}_{i,eff}^{atom}\right]\end{aligned} \tag{3.10}$$

Equation (3.10) can be written as:

$$-\frac{1}{\gamma}\frac{d\mathbf{M}_{total}}{dt} = \mathbf{M}_{total}\times\mathbf{H}_{eff}\ , \tag{3.11}$$

where

$$\mathbf{H}_{eff} = \sum_{i}\frac{\mu_i}{M_{total}}\mathbf{H}_{i,eff}^{atom}\ . \tag{3.12}$$

$\mathbf{H}_{\text{eff}}$ is the scaled sum of effective fields acting on each atom, and $\mathbf{M}_{\text{total}}$ is the total magnetic moment of the film. Equation (3.11) gives us both static and dynamic solutions. In the static case,

$$\mathbf{M}\times\mathbf{H}_{eff} = 0 \tag{3.13}$$

and, therefore, the magnetization **M** will be parallel to the total static effective field $\mathbf{H}_{\text{eff}}$. In the dynamic case, the general solutions to the L-L equation of motion (3.11) are non-linear and complex. However, in FMR, the magnetization **M** is nearly parallel to $\mathbf{H}_{\text{eff}}$:

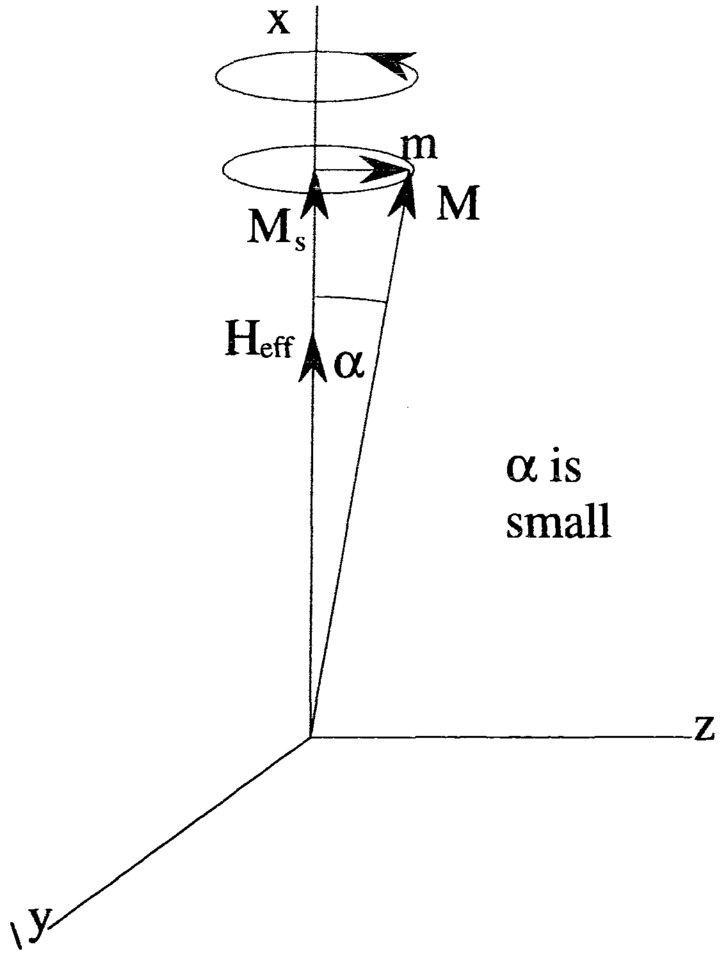

Figure 3.1 The coordinate system for FMR.

In that case,

$$\mathbf{M} = \mathbf{M}_s + \mathbf{m}\ ;\ |\mathbf{m}| << |\mathbf{M}_s| \tag{3.14}$$

Let's consider a solution of equation (3.11) in the coordinate system shown in Figure 3.1. $\mathbf{H}_{eff}$ can be very complex and will be dealt with later on, but here we will consider a simple case when $\mathbf{H}_{eff}$=$\mathbf{H}_{dc}$, where $\mathbf{H}_{dc}$ is the static externally applied field. The external field $\mathbf{H}_{dc}$ and the magnetization **M** can now be written as:

$$H_{eff} = \hat{\mathbf{x}}H_{dc} \tag{3.15}$$

$$M = \hat{\mathbf{x}}M_s + \mathbf{m}\exp(-i\omega t) \tag{3.16}$$

where free harmonic oscillation were assumed:

$$\mathbf{m}\exp(-i\omega t) = \left(m_x\hat{\mathbf{x}} + m_y\hat{\mathbf{y}} + m_z\hat{\mathbf{z}}\right)\exp(-i\omega t) \tag{3.17}$$

Substituting the above equations into equation (3.11) yields:

$$\begin{aligned} &m_x = 0 \\ &i\omega m_y - \gamma m_z H_{dc} = 0 \\ &\gamma m_y H_{dc} + i\omega m_z = 0 \end{aligned} \tag{3.18}$$

In order for the above equations to be consistent the determinant must be equal to zero which gives the expression for frequency of the oscillations:

$$\omega = \gamma H_{dc} \tag{3.19}$$

Further, substituting equation (3.19) into (3.18) yields:

$$m_y = -im_z \tag{3.20}$$

which indicates that the vector $\mathbf{m}_0$ is right-hand circularly polarized. Therefore, vector **M** precesses around the direction of the applied dc field $\mathbf{H}_{dc}$ with a frequency $\omega = \gamma H_{dc}$: $m_y = m_0\cos\omega t$, $m_z = m_0\sin\omega t$.

In real systems the precession is damped through dissipation processes, therefore, an alternating rf magnetization is needed to supply energy to maintain the precessional motion. In FMR studies, the static external field $\mathbf{H}_{dc}$ is combined with a small rf magnetic field $\mathbf{h}$ and all the internal fields represented here by $\mathbf{H}_{internal}$:

$$\begin{aligned}\mathbf{H}_{eff} &= \sum_i \frac{\mu_i}{M_{total}} \mathbf{H}^{atom}_{i,eff} = \sum_i \frac{\mu_i}{M_{total}} \left(\mathbf{H}_{dc} + \mathbf{H}^{atom}_{i,internal} + \mathbf{h} \right) \\ &= \mathbf{H}_{dc} + \left(\sum_i \frac{\mu_i}{M_{total}} \mathbf{H}^{atom}_{i,internal} \right) + \mathbf{h} \\ &= \mathbf{H}_{dc} + \mathbf{H}_{internal} + \mathbf{h}\end{aligned} \tag{3.21}$$

where $H_{internal} = \sum_i \frac{\mu_i}{M_{total}} \mathbf{H}^{atom}_{i,internal}$

The L-L equations (3.11) must be solved with $\mathbf{H}_{eff}$ which includes all of the internal fields to be defined in the next section. But the picture doesn't change in the presence of internal fields, except that the precessional resonant frequency is now dependent not only on the external field but also on parameters describing the internal fields. In FMR, the power supplied by a small rf microwave magnetic field $\mathbf{h}$ of frequency ω_0 is partly absorbed by the film to maintain the precession. As the external field is varied, the resonance frequency of the precessional motion is changed. At the resonant field, $\mathbf{H}_{res}$, the microwave frequency ω_0 equals the precessional frequency of the film, and the microwave absorption reaches a maximum. The following sections of this chapter show how the various magnetic properties of the ultrathin film can be extracted from the FMR measurements. The next section defines the geometry of FMR measurements, then the internal fields are discussed, and finally solutions of the L-L equations of motion are presented for the small amplitude limit.

3.3 Geometry of FMR

All measurements were carried out in the parallel configuration. In this configuration the applied static dc field, $\mathbf{H}_{dc}$, and the saturation magnetization, $\mathbf{M}_S$, are in the plane of the film. Figure 3.2 shows the geometry of the parallel configuration with the appropriate coordinate system. The ultrathin ferromagnetic cobalt films were grown on a non-magnetic copper substrate with the normal along the [001] crystallographic axis. The z-axis is chosen to lie along this normal. In the plane of the film, the x-axis is attached to the equilibrium saturation magnetization vector $\mathbf{M}_S$. The static field, $\mathbf{H}_{dc}$, is applied at an angle φ with respect to the [100] crystallographic direction. Due to the internal fields $\mathbf{M}_S$ is at an angle θ-φ to the dc field $\mathbf{H}_{dc}$. The saturation magnetization makes an angle θ with the in-plane crystallographic axis [100]. The external field can be rotated in the plane of the film thereby changing the angle φ to any desired value. The incident microwave magnetic field, $\mathbf{h} = h_y \hat{y} \cdot \exp(-i\omega t)$, is linearly polarized and perpendicular to the external dc field, i.e. approximately along the y-axis for small θ-φ. For simplicity we shall assume that $\mathbf{h}$ is perpendicular to $\mathbf{M}_S$. The rf response, $\mathbf{m} = \left(m_y \hat{y} + m_z \hat{z}\right) \exp(kz - i\omega t)$, to small rf fields must be obtained by solving the Landau-Lifshitz equations of motion combined with Maxwell's equations with appropriate boundary conditions [3.2]. However, for the ultrathin film limit, the spatial variation across the film can be neglected. Therefore, only the time dependence, $\exp(-i\omega t)$, will be considered.

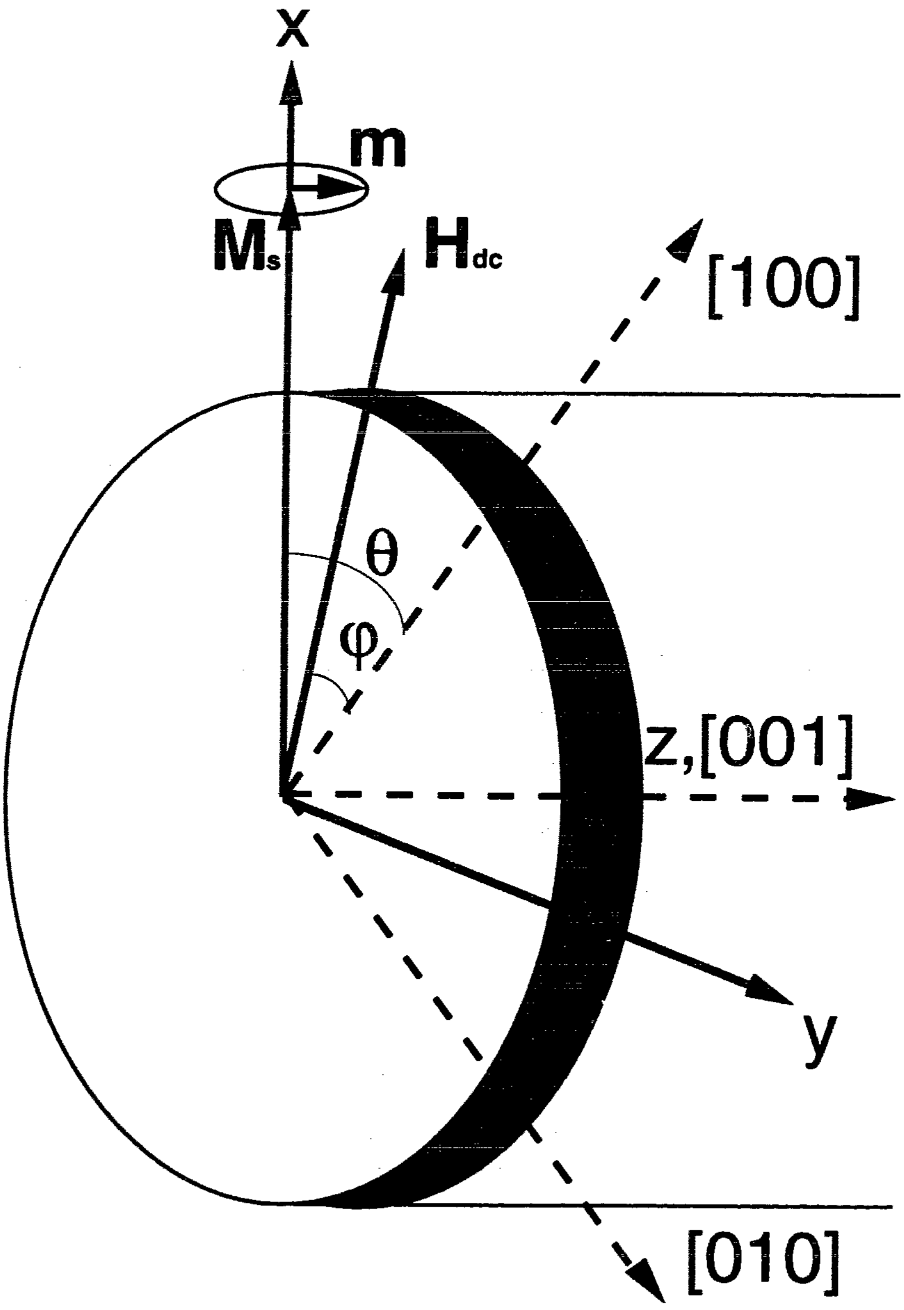

Figure 3.2. Geometry of the parallel configuration of FMR and the related coordinate system.

In realistic systems the motion of magnetization is damped by dissipative processes. The dissipation is usually described by the Gilbert effective field which acts as a frictional torque, $\mathbf{H}_G \propto \frac{\partial \mathbf{M}}{\partial t}$ [3.4, 3.5]. The L-L. equation of motion including a damping term can be written :

$$-\frac{1}{\gamma}\frac{d\mathbf{M}}{dt} = \left[\mathbf{M} \times \mathbf{H}_{eff}\right] - \frac{G}{\gamma^2 \cdot M_s^2}\left[\mathbf{M} \times \frac{\partial \mathbf{M}}{\partial t}\right] \tag{3.22}$$

where the effective magnetic field, $\mathbf{H}_{\text{eff}}$, consists of all the static and rf magnetic fields:

$$\mathbf{H}_{eff} = \mathbf{H}_0 + \mathbf{h} + \underbrace{\mathbf{H}_D + \mathbf{H}_k}_{\mathbf{H}_{int}^{eff}} \tag{3.23}$$

where $\mathbf{H}_0 = H_0 \cos(\theta - \varphi) \cdot \hat{\mathbf{x}} + H_0 \sin(\theta - \varphi) \cdot \hat{\mathbf{y}}$ (3.24)

is the applied magnetic field, and

$$\mathbf{h} = h_y \exp(-i\omega t)\hat{\mathbf{y}} = \left(0, h_y \exp(-i\omega t), 0\right) \tag{3.25}$$

is the rf microwave magnetic field. $\mathbf{H}_\mathrm{D}$ is the demagnetizing field, and $\mathbf{H}_\mathrm{k}$ is the magnetocrystalline anisotropy field. Due to strong damping and small rf field, the magnetization $\mathbf{M}$ makes only small deviations from the equilibrium saturation magnetization $\mathbf{M}_\mathrm{s}$. The second order and higher terms of small rf magnetic components, $|\mathbf{m}| \ll |\mathbf{M}_\mathrm{s}|$, can be neglected. Hence, the linear response of the film is

$$\mathbf{M} = \mathbf{M}_s + \mathbf{m}\cdot\exp(-i\omega t) = M_s\hat{\mathbf{x}} + (m_y\hat{\mathbf{y}} + m_z\hat{\mathbf{z}})\cdot\exp(-i\omega t)$$
$$= \left(M_s, m_y\exp(-i\omega t), m_z\exp(-i\omega t)\right) \quad (3.26)$$

3.4 Internal fields

Due to the spin-orbit interaction the energy of the atom depends on the direction of the magnetization with respect to the crystallographic axes. Assuming that the spatial variations are slow compared with a lattice constant, the energy density E is given by:

$$\mathsf{E} = \frac{E_{atom}}{V_{atom}}, \quad (3.27a)$$

and the magnetization is given by

$$M = \frac{\mu}{V_{atom}} \quad (3.27b)$$

where E_{atom} is the energy per atom, and V_{atom} is the atomic volume per atom. For an fcc lattice with a lattice constant a:

$$\mathsf{E} = \frac{E_{atom}}{a^3/4} \quad (3.27c)$$

The effective fields can be obtained from the free energy density E of the film expressed as a function of magnetization using variational calculations [3.6, 3.4, 3.1] which lead to:

$$\mathbf{H}_{eff} = -\frac{\partial \mathrm{E}(\mathbf{M})}{\partial \mathbf{M}} = -\left(\frac{\partial \mathrm{E}}{\partial M_x}, \frac{\partial \mathrm{E}}{\partial M_y}, \frac{\partial \mathrm{E}}{\partial M_z} \right) \tag{3.28}$$

where E is the free energy density. It follows that the internal field $\mathbf{H}^{atom}_{i,internal}$ acting on atomic moment "i" is given by equation (3.28) with energy E_{atom} corresponding to the atomic energy of the atom "i":

$$\mathbf{H}^{atom}_{i,internal} = -\frac{\partial E_{atom}(\vec{\mu})}{\partial \vec{\mu}} \tag{3.29}$$

This expression can be now employed to calculate internal fields in equation (3.21) for an ultrathin film which has N atomic layers each containing n atoms. The interfaces are located at i=1 and at i=N, see Figure 3.3 below.

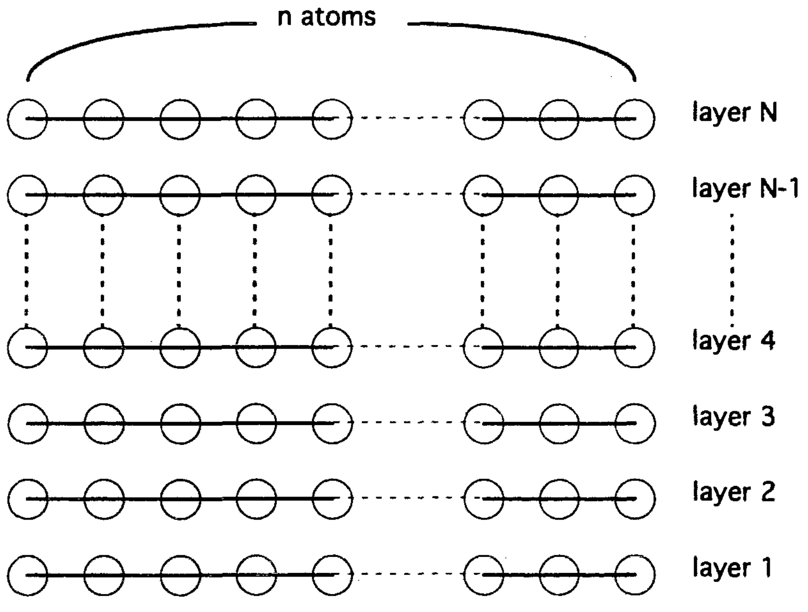

Figure 3.3. Ultrathin film of N atomic layers with n atoms in each layer used to calculate the bulk and interface contributions of the internal magnetic fields.

For simplicity let us assume that the atomic magnetic moment μ_i is independent of the atom position. Further, let's assume that all atomic magnetic moments possess the bulk energy and that the interface atomic moments have additional magnetic energies which originate in the broken symmetry at the interfaces. Pursuing only the internal part of the effective field in equation (3.21):

$$
\begin{aligned}
H_{internal} &= \sum_i \frac{\mu_i}{M_{total}} \mathbf{H}^{atom}_{i,internal} = \sum_{k=1}^{N} \sum_{l=1}^{n} \frac{\mu_{k,l}}{M_{total}} \mathbf{H}^{atom}_{k,l,internal} \\
&= \sum_{k=1}^{N} \frac{\mu}{M_{total}} n\mathbf{H}^{k}_{bulk} + \frac{n\mu}{M_{total}} \left(\mathbf{H}^{1}_{interface} + \mathbf{H}^{N}_{interface} \right) \\
&= \frac{\mu}{M_{total}} n \sum_{k=1}^{N} \mathbf{H}^{k}_{bulk} + \frac{n\mu}{M_{total}} \left(\mathbf{H}^{1}_{interface} + \mathbf{H}^{N}_{interface} \right) \\
&= \frac{\mu}{M_{total}} nN\mathbf{H}^{k}_{bulk} + \frac{n\mu}{M_{total}} \left(\mathbf{H}^{1}_{interface} + \mathbf{H}^{N}_{interface} \right) \\
&= \frac{\mu}{M_{total}} Nn\mathbf{H}_{bulk} + \frac{\mu}{M_{total}} n\mathbf{H}^{1}_{interface} + \frac{\mu}{M_{total}} n\mathbf{H}^{N}_{interface} \\
&= \mathbf{H}_{bulk} + \frac{1}{N}\mathbf{H}^{1}_{interface} + \frac{1}{N}\mathbf{H}^{N}_{interface} \qquad (3.30)
\end{aligned}
$$

where k is the layer index and l is the position of an atom within the kth layer; $M_{total}=N\,n\mu$ is the magnitude of the total magnetic moment of the film. But the number of monolayers can be obtained by dividing the thickness of the film "d" by the interatomic spacing "a" both in angstroms. This leads to another useful expression for the effective internal fields:

$$
\mathbf{H}^{eff}_{internal} = \mathbf{H}_{bulk} + \frac{1}{d}\left(a\mathbf{H}^{1}_{interface} + a\mathbf{H}^{N}_{interface} \right) \qquad (3.31)
$$

The total effective internal field acting on atomic moments in the film consists of two contributions: one which is a bulk contribution, and another which originates in the interfaces and decreases inversely with increasing thickness of the film.

At this point we have derived the meaning of the macroscopic fields for ultrathin films. One would like to evaluate the effective internal fields using equation (3.28) knowing the magnetic energy densities, usually called magnetic anisotropies. Magnetic anisotropies are macroscopic quantities which have to satisfy the symmetry of the sample. Let us restrict further discussion to the geometry of Co(001) samples which have the bulk tetragonal symmetry with the sample normal oriented in the (001) direction, see Figure 2.15 in Chapter 2.

3.5 The magnetocrystalline anisotropy

Magnetocrystalline anisotropy energies originate from the microscopic spin-orbit interaction. Since the orbital motion of an electron is coupled to the crystalline structure, the total internal energy depends on the direction of magnetization with respect to the crystal axes. The magnetocrystalline anisotropy energies have to satisfy the symmetry of the crystal. They favor certain directions of magnetization within a crystalline sample. Phenomenologically, the magnetocrystalline energy can be expressed as a function of the angles between the magnetization, **M**, and the crystallographic axes. In order to represent magnetocrystalline energy in an arbitrary direction one can expand it in powers of directional cosines between **M** and the three cubic axes. Due to the invariance of energy upon time reversal all the odd powers of the direction cosines, α_i's, in the expansion must disappear. For a perfect cubic lattice, any interchange of the direction cosines, α_i's, should result in the same energy. Therefore, the terms of the form $\alpha_i^l \cdot \alpha_j^m \cdot \alpha_k^n$ must have, for any given combination of l, m, n, the same coefficient for any given interchange of i, j and k. One can write:

$$\begin{aligned} E_k = {} & \underbrace{C_{21}\left(\alpha_1^2+\alpha_2^2+\alpha_3^2\right)}_{\text{second order term}} \\ & \underbrace{+C_{41}\left(\alpha_1^4+\alpha_2^4+\alpha_3^4\right)}_{\text{first fourth order term}} \\ & \underbrace{+C_{42}\left(\alpha_1^2\alpha_2^2+\alpha_1^2\alpha_3^2+\alpha_2^2\alpha_3^2\right)}_{\text{second fourth order term}} \\ & \underbrace{+C_{61}\left(\alpha_1^6+\alpha_2^6+\alpha_3^6\right)}_{\text{first sixth order term}} \\ & \underbrace{+C_{62}\left(\alpha_1^4\alpha_2^2+\alpha_1^4\alpha_3^2+\alpha_2^4\alpha_1^2+\alpha_2^4\alpha_3^2+\alpha_3^4\alpha_1^2+\alpha_3^4\alpha_2^2\right)}_{\text{second sixth order term}} \qquad (3.32) \\ & \underbrace{+C_{63}\alpha_1^2\alpha_2^2\alpha_3^2}_{\text{third sixth order term}} + \underbrace{\ldots\ldots\ldots\ldots\ldots}_{\text{higher order terms}} \end{aligned}$$

where C_{in}'s are the constants of the i^{th} order n^{th} term. By using the identity $\alpha_1^2+\alpha_2^2+\alpha_3^2=1$, we can modify the expression for the anisotropy energy as follows [3.7]:

$$E_k = -K_0 - \frac{1}{2}K_1\left(\alpha_1^4+\alpha_2^4+\alpha_3^4\right) + K_2\alpha_1^2\alpha_2^2\alpha_3^2 + \ldots \qquad (3.33)$$

where E_k is the magnetocrystalline anisotropy energy per unit volume, referred to as the cubic anisotropy energy from here on, K_i's are the anisotropy constants which determine the strength of the anisotropies, and

$$\alpha_1 = \cos\beta_{[100]} = \frac{M_{[100]}}{M_s} \; ; \; \alpha_2 = \cos\beta_{[010]} = \frac{M_{[010]}}{M_s}$$
$$\alpha_3 = \cos\beta_{[001]} = \frac{M_{[001]}}{M_s} \tag{3.34}$$

are the directional cosines. M_i are the components of magnetization along the cubic axes i, and β_i are the angles that the magnetization makes with the cubic axes i. Ultrathin films are often tetragonally distorted. The vertical compression along the [001] axis makes the anisotropy constants for the normal direction $K_{i\perp}$ different than the in-plane constants $K_{i\parallel}$. Tetragonal distortions reintroduce the second order powers into the magnetocrystalline anisotropy. The total energy can be written as:

$$E_k = -K_{0\parallel}\left(\alpha_1^2 + \alpha_2^2\right) - K_{0\perp}\alpha_3^2 - \frac{1}{2}K_{1\parallel}\left(\alpha_1^4 + \alpha_2^4\right) - \frac{1}{2}K_{1\perp}\alpha_3^4 - \ldots \tag{3.35}$$

The constant term has been dropped because it does not contribute to the effective fields, see equation (3.28). Let's consider second order terms. By using the trigonometric identity $\alpha_1^2 + \alpha_2^2 + \alpha_3^2 = 1$ one can eliminate α_1 and α_2:

$$E_{k0} = -K_{0\parallel}\left(1 - \alpha_3^2\right) - K_{0\perp}\alpha_3^2 = -K_{0\parallel} - \left(K_{0\perp} - K_{0\parallel}\right)\alpha_3^2 \tag{3.36}$$

The constant term can be ignored because it does not contribute to the effective field. The uniaxial anisotropy energy is defined by:

$$E_u = -K_u\alpha_3^2 \, , \; K_u = K_{0\perp} - K_{0\parallel} \tag{3.37}$$

Therefore, the total anisotropy energy can be expressed as:

$$E_k = -\frac{1}{2}K_{1\|}\left(\alpha_1^4 + \alpha_2^4\right) - \frac{1}{2}K_{1\perp}\alpha_3^4 - K_u\alpha_3^2 \tag{3.38}$$

where the first term is the fourfold in-plane anisotropy characterized by the in-plane anisotropy constant $K_{1\|}$, the second term is the fourfold perpendicular anisotropy characterized by the constant $K_{1\perp}$, and the third term is the uniaxial anisotropy characterized by the uniaxial anisotropy constant K_u. Higher order terms are usually not needed. In the parallel configuration ($\mathbf{M}_s$ lies in the surface of the film) the effective field due to the fourfold perpendicular anisotropy is negligible in FMR, because the out-of-plane component of magnetization, $M_{[001]}=m_z$, is small. Therefore, the anisotropy energy applicable for the parallel configuration is:

$$E_k = -\frac{1}{2}K_{1\|}\left(\alpha_1^4 + \alpha_2^4\right) - K_u\alpha_3^2 \tag{3.39}$$

Consider the uniaxial anisotropy contribution to the energy. For negative K_u, the uniaxial anisotropy energy is minimum when the magnetization is in the plane of the film. This plane is called an easy plane. The uniaxial contribution then favors the in-plane orientation of magnetization. The normal direction [001] is called a hard axis. As the magnetization rotates away from an easy plane ($\beta_{[001]}=90°$) in either direction the uniaxial anisotropy increases, reaching maximum when the magnetization is oriented along the hard axis ($\beta_{[001]}=0°$ or $180°$). The behavior is periodic with period of 180°. If K_u is positive then the normal axis is the preferred direction, and becomes the easy axis.

Next, consider the behavior of the fourfold in-plane anisotropy contribution. For negative $K_{1||}$ the preferred directions, easy axes, within the plane are along the <110> axes. The [100] and the [010] directions are then hard axes. For positive $K_{1||}$ the behavior is reversed: the [100] and the [010] are the easy directions. The two easy axes are perpendicular, within the (001) plane, and are rotated 45° with respect to the two hard axes.

The magnetocrystalline anisotropy energies give rise to the anisotropy fields. They can be calculated using equation (3.28). In order to perform the indicated differentiations, the magnetization components need to be expressed in the x,y,z coordinate system for the parallel configuration of Figure 3.2.

$$\begin{aligned} M_{[100]} &= M_x \cos\theta - M_y \sin\theta \\ M_{[010]} &= M_x \sin\theta + M_y \cos\theta \\ M_{[001]} &= M_z \end{aligned} \tag{3.40}$$

The anisotropy effective fields, up to a linear power in m_y and m_z, can be obtained using equations (3.28), (3.39) and (3.40):

$$\begin{aligned} \mathbf{H}_k = {} & \frac{K_{1||}}{2M_s^2}\left[M_s(3+\cos 4\theta) - 3m_y \cdot \exp(-i\omega t)\cdot \sin 4\theta\right]\hat{\mathbf{x}} \\ & + \frac{K_{1||}}{2M_s^2}\left[-M_s \sin 4\theta + 3m_y \cdot \exp(-i\omega t)\cdot(1-\cos 4\theta)\right]\hat{\mathbf{y}} \\ & + \frac{2K_u m_z \cdot \exp(-i\omega t)}{M_s^2}\hat{\mathbf{z}} \end{aligned} \tag{3.41}$$

where the approximation $M_x = M_s$ has been used.

For simplicity, consider the dc field and the saturation magnetization oriented along the major [100] axis ($\theta=0$), see Figure 3.2. From equation (3.41) the crystalline anisotropy fields are as follows:

$$\mathbf{H}_k = \frac{2K_{1\parallel}}{M_s}\hat{\mathbf{x}} + \frac{2K_u}{M_s}\left(\frac{m_z}{M_s}\right)\exp(-i\omega t)\hat{\mathbf{z}} \qquad (3.42)$$

where $H_{1\parallel}=2K_{1\parallel}/M_S$ is usually used to describe the strength of the fourfold in-plane field, and $H_u=2K_u/M_S$ is usually used to describe the strength of the uniaxial perpendicular anisotropy field. The effective uniaxial and fourfold in-plane anisotropies include both bulk and surface contributions as per equation (3.31). From that equation:

$$K_{1\parallel}^{eff} = K_{1\parallel}^{bulk} + \frac{1}{d}\left(aK_{1\parallel}^{1,interface} + aK_{1\parallel}^{N,iinterface}\right) = K_{1\parallel}^{bulk} + \frac{1}{d}\left(K_{1\parallel}^{1,s} + K_{1\parallel}^{N,s}\right) \qquad (3.43)$$

$$K_u^{eff} = K_u^{bulk} + \frac{1}{d}\left(aK_{\mathrm{u}}^{1,interface} + aK_{\mathrm{u}}^{N,interface}\right) = K_{\mathrm{u}}^{bulk} + \frac{1}{d}\left(K_{\mathrm{u}}^{1,s} + K_{\mathrm{u}}^{N,s}\right) \qquad (3.44)$$

where

$$K_{1\parallel}^{1,s} = aK_{1\parallel}^{1,interface}, K_{1\parallel}^{N,s} = aK_{1\parallel}^{N,interface} \qquad (3.43a)$$

$$K_u^{1,s} = aK_u^{1,interface}, K_u^{N,s} = aK_u^{N,interface} \qquad (3.44a)$$

are the in-plane fourfold and uniaxial perpendicular surface anisotropy constants. Hence, the effective fourfold in-plane and uniaxial perpendicular anisotropy fields consist of bulk and surface contributions:

$$K_{1\parallel}^{eff} = K_{1\parallel}^{\text{bulk}} + \frac{1}{d} K_{1\parallel}^{\text{s}} \tag{3.45}$$

$$K_{u}^{eff} = K_{u}^{\text{bulk}} + \frac{1}{d} K_{u}^{\text{s}} \tag{3.46}$$

where $K_{1\parallel}^{\text{bulk}}$, K_{u}^{bulk}, $K_{1\parallel}^{\text{s}}$, K_{u}^{s} describe the strength of bulk and surface fourfold in-plane and perpendicular uniaxial anisotropies. All relevant interfaces must be considered in both $K_{1\parallel}^{\text{s}}$ and K_{u}^{s}. The thickness dependent interface term represents the difference in the magnetic properties between the bulk layers and the interface layers [3.8, 3.9]. It follows from equation (3.27c) that the first principle calculations anisotropy constant for an fcc surface net are related to the macroscopic constants per interface by:

$$K_{1\parallel}^{\text{s}} = \frac{2K_{1\parallel}^{\text{s,atom}}}{\text{a}^2} \tag{3.47}$$

$$K_{\text{u}}^{\text{s}} = \frac{2K_{u}^{\text{s,atom}}}{\text{a}^2} \tag{3.48}$$

where a is the fcc lattice constant.

3.6 The demagnetizing field

When a magnetic material of finite dimensions is placed in a magnetic field, the induced magnetic poles at the surface of the sample oppose the magnetization. This opposing field is referred to as the demagnetizing field. It originates in the long range dipole-dipole interaction that acts between magnetic moments. Due to its dependence on the shape, the restoring demagnetizing energy is often called the shape anisotropy energy. Consider the parallel configuration employed in the study of Co(001) ultrathin structures, see Figure 3.4. The magnetization, $\mathbf{M_S}$, tilted away from the surface of the ferromagnetic film has a small component $\mathbf{m_Z}$

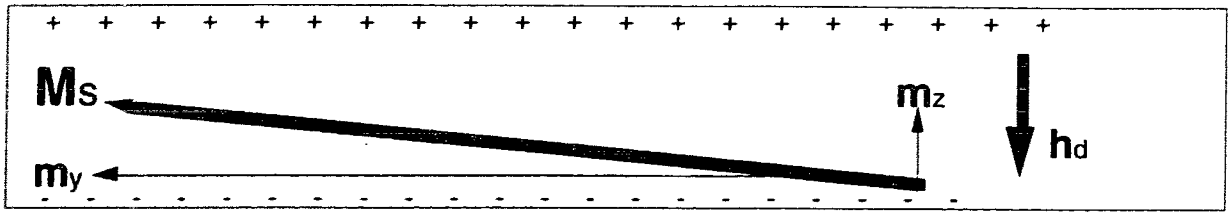

Figure 3.4. The demagnetizing field, $\mathbf{h}_d$, in the parallel configuration.

perpendicular to the surface. The induced magnetic poles at both interfaces result in the restoring demagnetizing field:

$$\mathbf{h}_d = -4\pi D\mathbf{m}_z = \left(0,0,-4\pi D m_z \exp(-i\omega t)\right) \tag{3.49}$$

or, in other words, in the restoring demagnetizing energy:

$$E_D = \frac{4\pi D}{2} m_z^2 \tag{3.50}$$

which favors the in-plane orientation of magnetization. 4πD is the effective demagnetizing factor. For an ultrathin film whose thickness is a few atomic layers, the factor 4πD is calculated by averaging over the discrete sum of dipolar magnetic fields acting on a magnetic atom in every lattice plane. For an fcc lattice with the [001] axis along the film normal [3.10, appendix of 3.11]:

$$4\pi D = 4\pi\left(1-\frac{0.2338}{N}\right) \tag{3.51}$$

where N is the film thickness in monolayers (ML). In the continuum limit (N→ ∞), this factor is just 4π. It is worth pointing out that the shape anisotropy has its own constant term plus 1/N thickness dependent term (see equation 3.51 above) that behave like a bulk field and an interface anisotropy field that varies like 1/d.

3.7 Resonance condition

Upon substituting equations (3.23-3.26, 3.41, and 3.49) into (3.22), with time dependence exp(-iωt), the L-L equations of motions for parallel configuration, linearized in h_y, m_y, and m_z , become:

$$\left[H_0\cos(\theta-\varphi)+4\pi DM_s-\frac{2K_u^{eff}}{M_s}+\frac{K_{1\parallel}^{eff}}{2M_s}(3+\cos 4\theta)-\frac{i\omega}{\gamma}\frac{G}{\gamma M_s}\right]m_z$$

$$-\frac{i\omega}{\gamma}m_y=0 \tag{3.52}$$

$$\left[H_0\cos(\theta-\varphi)+\frac{2K_{1\parallel}^{eff}}{M_s}\cos 4\theta-\frac{i\omega}{\gamma}\frac{G}{\gamma M_s}\right]m_y+\frac{i\omega}{\gamma}m_z=M_s h_y$$

where the rf magnetization components parallel and perpendicular to the film surface, m_y and m_z, are averaged across the film thickness per unit area. Because the demagnetizing field, $4\pi DM_S$, and the uniaxial perpendicular anisotropy field, $\frac{2K_u^{\text{eff}}}{M_s}$, are indistinguishable within the framework of equations (3.52), the effective demagnetizing field, $4\pi M_{\text{eff}}$, is introduced:

$$4\pi M_{eff} = 4\pi D M_s - \frac{2K_u^{eff}}{M_s} \tag{3.53}$$

The microwave power absorbed by the ultrathin film, P_a, is proportional to the imaginary part of the rf susceptibility, Im(χ), $P_a \sim \omega \mathrm{Im}(\chi) h_y^2$. By eliminating m_z from equations (3.52) one can obtain an expression for the rf susceptibility $\chi = \chi' + i\chi'' = m_y/h_y$:

$$\chi = \frac{M_s\left(\tilde{B} - \frac{i\omega}{\gamma}\frac{G}{\gamma M_s}\right)}{\left(\tilde{B} - \frac{i\omega}{\gamma}\frac{G}{\gamma M_s}\right)\left(\tilde{H} - \frac{i\omega}{\gamma}\frac{G}{\gamma M_s}\right) - \left(\frac{\omega}{\gamma}\right)^2} \tag{3.54}$$

where

$$\tilde{B} = H_0 \cos(\theta - \varphi) + 4\pi M_{eff} + \frac{K_{1\parallel}^{eff}}{2M_s}(3 + \cos 4\theta) \tag{3.55}$$

and

$$\tilde{H} = H_0 \cos(\theta - \varphi) + \frac{2K_{1\parallel}^{eff}}{M_s}\cos 4\theta \tag{3.56}$$

The imaginary part of the susceptibility χ'', and hence the absorbed microwave power, P_a, reach maximum when the denominator of equation (3.54) is minimum. This condition occurs when the real part of the denominator is zero:

$$\mathrm{Re}\left[\left(\tilde{B}-\frac{i\omega}{\gamma}\frac{G}{\gamma M_s}\right)\left(\tilde{H}-\frac{i\omega}{\gamma}\frac{G}{\gamma M_s}\right)-\left(\frac{\omega}{\gamma}\right)^2\right]=0 \tag{3.57}$$

The shift in the resonance due to the magnetic damping is small and can be neglected yielding a simpler form of the resonance condition:

$$\left(\frac{\omega}{\gamma}\right)^2=\left(H_{res}\cos(\theta-\varphi)+4\pi M_{eff}+\frac{K_{1\parallel}^{eff}}{2M_s}(3+\cos 4\theta)\right)\cdot \left(H_{res}\cos(\theta-\varphi)+\frac{2K_{1\parallel}^{eff}}{M_s}\cos 4\theta\right) \tag{3.58}$$

where H_{res} is the resonant field corresponding to a particular frequency ω. From measurements of H_{res} as a function of φ at different microwave frequencies one can determine most of the magnetic properties of an ultrathin film. From the frequency dependence of H_{res} one can obtain the gyromagnetic ratio, γ, and the effective demagnetizing field $4\pi M_{eff}$. Sufficiently different microwave frequencies are necessary. Use of 24 GHz and 74 GHz should be adequate in most cases. Then the g-factor can be obtained from equation (3.5). The angular dependence of H_{res} yields the fourfold in-plane anisotropy field, $\frac{2K_{1\parallel}^{eff}}{M_s}$. The perpendicular uniaxial anisotropy is then obtained from equation (3.53) using the demagnetizing field with D calculated for a finite fcc lattice as in equation (3.51) and using the saturation magnetization, M_s, obtained from a static measurement. Studying the thickness dependence of anisotropies may allow one to separate the bulk and the surface contributions as in equations (3.45) and (3.46).

3.8 FMR linewidth ΔH

The dynamic damping can be studied by the means of the FMR linewidth, ΔH, which is the field separation between the extrema of the derivative of the absorption ~ $d\chi''/dH$. The microwave frequency dependence of the FMR linewidth can be described in ultrathin films as [3.12]

$$\Delta H = \Delta H(0) + 1.16\,\frac{\omega}{\gamma}\,\frac{G}{\gamma M_S}, \tag{3.59}$$

where the frequency dependent part arises from the intrinsic magnetic damping and ΔH(0) is caused by magnetic inhomogeneities incorporated into the film structure during the growth [3.13]. ΔH(0) is often used as a measure of the quality of epitaxially grown films.

3.9 FMR apparatus.

A block diagram of the FMR apparatus is shown in Figure 3.5. Microwave frequencies in the range of 10-100 GHz are required. A klystron supplies microwave power to a resonant cavity located between the pole pieces of an electromagnet. The klystron frequency is locked to the cavity resonant frequency by modulating the klystron reflector voltage by a small ac signal at 70 kHz [3.14]. The ferromagnetic sample to be studied forms the end wall of the cavity. The microwave cavity is coupled to the waveguide through a small coupling hole in the top part of the cavity, see Figure 3.6. A small coupling hole was used in order to operate in an undercoupled mode, see Appendix A. An increase in the microwave absorption of the sample decreases the quality factor of the cavity, Q_{cavity}, and in the case of the undercoupled mode leads to an increase of the reflected microwave power, see Appendix A. The FMR signal is measured by monitoring the reflected power from the cavity as a function of the applied dc field H_{dc}. At the resonant field, H_{res}, the microwave absorption of the sample reaches a maximum, and in the undercoupled case it leads to a maximum amplitude of the reflected microwave electric field, E_r.

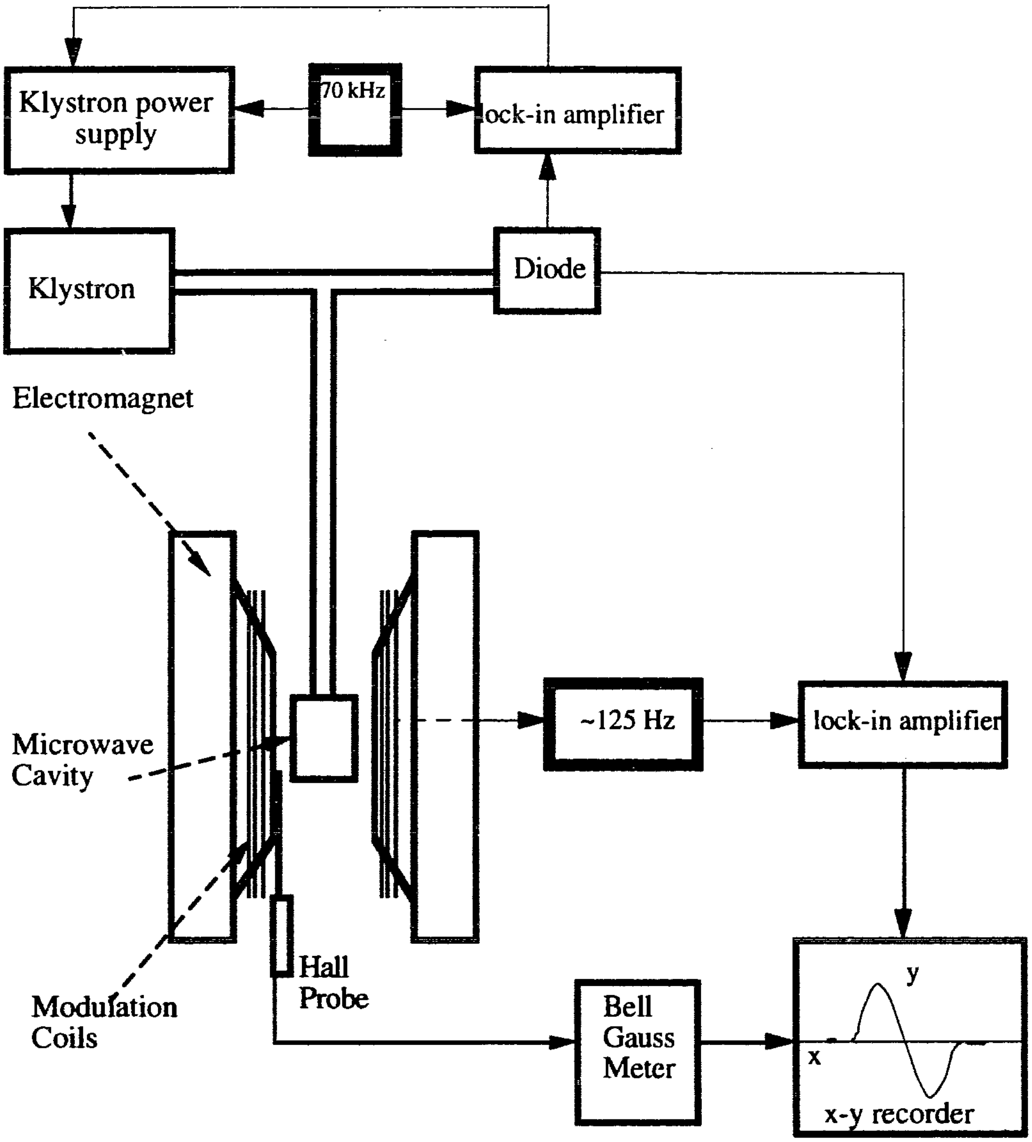

Figure 3.5. Block diagram of the FMR apparatus.

The reflected microwave field amplitude, E_r, is detected by means of a microwave diode detector which generates a dc voltage proportional to E_r. Formula (A.13) from the appendix suggests that the maximum sensitivity can be reached for the critically coupled cavity ($\beta_0=1$, see Appendix A). However in this case the microwave diode works in its quadratic response and for small ΔE_r the diode becomes insensitive. One needs to increase β_0 to provide a sufficient reflected microwave power which assures an optimum microwave diode performance. A maximum performance is achieved by using a coupling parameter β_0 in the range of $1.8<\beta_0<3$ which corresponds to the reflection of 30%-50% of the incident microwave power. For the diode output above 10 mV the microwave diode response is linear (maximum sensitivity). The optimum noise performance of the diode is achieved by terminating its output with a 1 kΩ resistor which results in a dc current of ~10 μA.

The FMR measurements are carried out using a low frequency modulation of the external field (at 125 Hz). The signal from the diode detector acquires an ac component (at 125 Hz) which is measured using a lock-in amplifier detection (phase sensitive detection) to improve the signal-to-noise ratio. The resulting final signal is proportional to the field derivative of the reflected microwave absorption.

The microwave cavity used in the 36 GHz measurements was operated in the TE_{012} mode [3.15]. The substrate diameter (~20 mm) was larger than the cavity diameter (~11 mm at 36 GHz), and hence the entire end of the cavity was formed by the sample, see Figure 3.6. The sample was separated from the cylindrical body of the microwave cavity by a thin kapton foil in order to eliminate other microwave modes which are otherwise present in this type of cavity. A non-conducting kapton foil also prevents eddy currents, generated in the cavity by the low frequency field modulation, from shielding the specimen from the modulation field. The TE_{012} mode has its electric field at the end wall along the azimuthal direction only and approaches a zero value at the cavity walls. Therefore the internal cavity quality factor, Q_{cavity}, is not affected by the absence of the electrical contact between the end wall and the cylindrical body. In the parallel configuration the dc applied field is oriented along the sample surface, see Section 3.3. The cylindrical symmetry of the rf magnetic field permitted full 360° in-plane angular FMR studies.

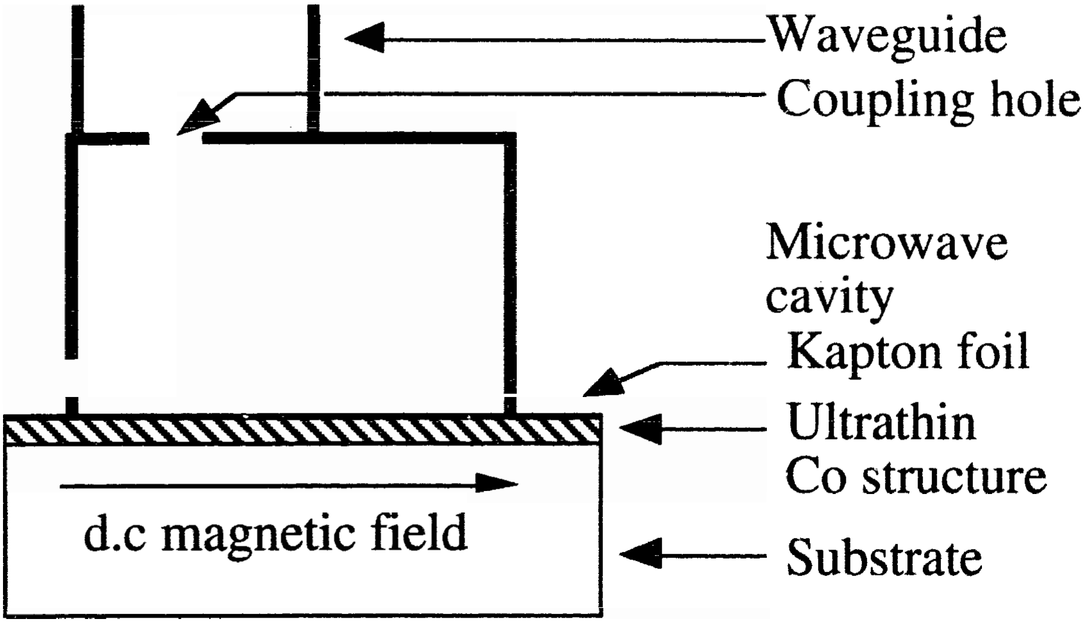

Figure 3.6. Microwave cavity used in the parallel configuration of FMR measurements at 36 GHz.

With a constant incoming power the reflected amplitude of the microwave electric field changes linearly with the absorbed microwave power in the sample. The power absorption, P_{sample}, is proportional to the imaginary part of the rf susceptibility $\chi''=\mathrm{Im}(m_y/h_y)$, $P_{sample} \sim \omega \chi'' h_y^2$, see

Section 3.7. Equation (3.54) for χ'' gives a typical resonance Lorentzian-like lineshape. The maximum absorption occurs at the resonance field, H_{res}, see equation (3.58). The linewidth of the resonance peak is given by the microwave losses. For small modulation of the dc field (appreciably smaller than the FMR linewidth) the measured signal is proportional to the dc field derivative $d\chi''/dH$. The resonance field, H_{res}, is given by the zero crossing of $d\chi''/dH$, and the FMR linewidth ΔH is equal to the field interval between the extrema of $d\chi''/dH$, see Figure 3.7.

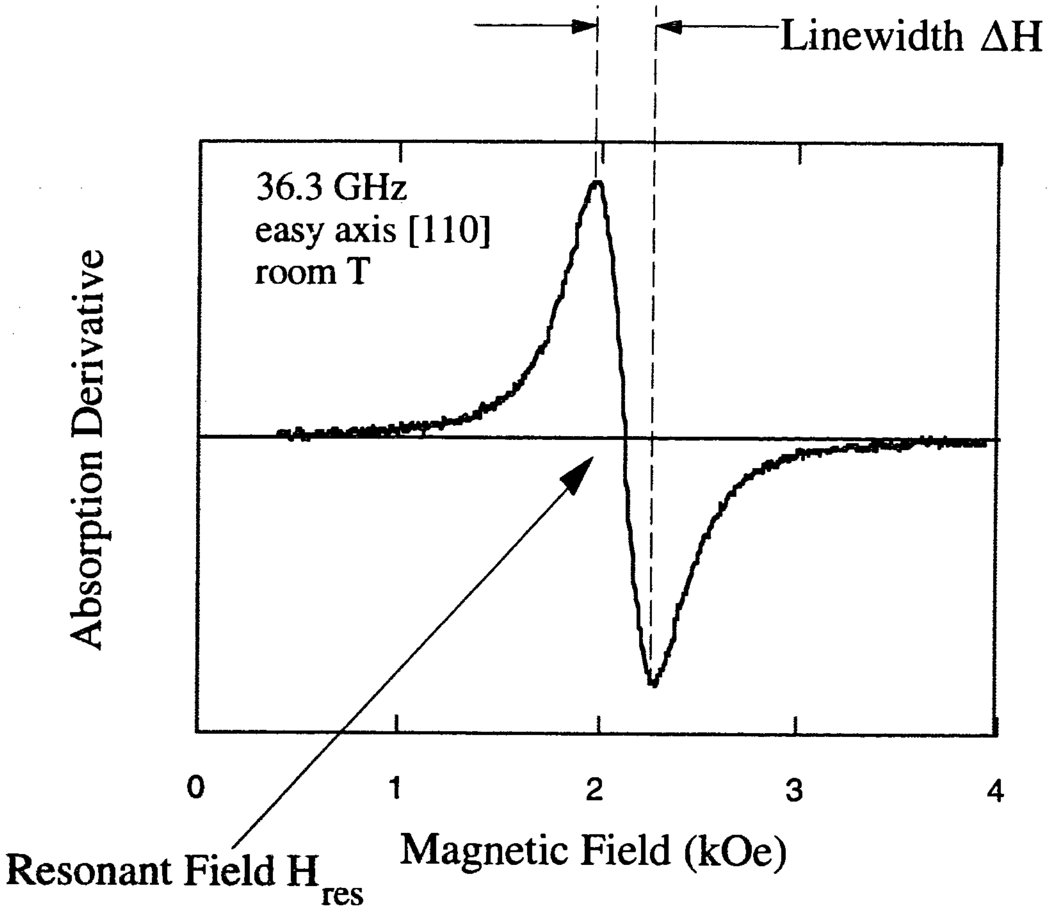

Figure 3.7. An example of the FMR signal in the Cu/4Co/6Cu/20Au sample. The zero crossing of the absorption derivative yields the resonant field H_{res}, and the field interval between its extrema yields the FMR linewidth ΔH.

Chapter 4

Ferromagnetic Resonance studies of Ultrathin fcc Co(001) Structures

4.1 Introduction

In this chapter the ferromagnetic resonance studies of ultrathin layers of metastable fcc Co(001) grown on a Cu(001) substrate are presented. The epitaxial growth procedure and the nomenclature used to represent samples were described in Chapter 2. There have been many studies of the structure of fcc Co(001) grown on a single crystal Cu(001) substrate, see Chapter 2; however, its magnetic properties have not been as extensively studied as in this work. The magnetic studies in this thesis give a detailed account of the basic magnetic properties of ultrathin metastable Co(001) grown on a Cu(001) template. Magnetic parameters such as magnetic anisotropies, the spectroscopic g-factor and the magnetic damping were obtained from the FMR measurements on single cobalt layer samples Cu(001)/Co/ Cu. Cobalt layers separated by a nonmagnetic Cu interlayer in sandwich structures (trilayers) Cu(001) /Co/Cu /Co/Cu were used to study the exchange interaction across the Cu spacer.

4.2 Experimental results and analysis of magnetic anisotropies

The in-plane easy and hard magnetic axes are simple to determine experimentally. Equation (3.58) shows that for the saturation magnetization oriented along the easy axis the resonant field, H_{easy}, reaches a minimum and for the magnetization oriented along the hard axis the resonant field,

H_{hard}, reaches a maximum. The measurements showed that the <100> crystallographic axes are the hard axes, and the <110> directions are the easy axes, see Figure 4.1. The measured resonance fields of ultrathin Co layers had relatively low values (1-5 kOe at 36GHz, room T) compared to that of $\frac{\omega}{\gamma}$ (~12 kOe at 36 GHz, assuming g=2 in equation 3.5). Low resonance fields, imply that $4\pi M_{eff} \gg H_{res}$, see equation 3.58. In this case a simple analysis can be carried out on the back of an envelope. One wishes to obtain the magnetic properties immediately after the FMR measurements are performed and for that reason this simplified approach will be demonstrated below. For $4\pi M_{eff} \gg H_{res}$ and $4\pi M_{eff} \gg \frac{2K_{1\parallel}^{eff}}{M_s}$ equation (3.58) becomes:

$$\left(\frac{\omega}{\gamma}\right)^2 = 4\pi M_{eff}\left(H_{easy} - \frac{2K_{1\parallel}^{eff}}{M_s}\right) \quad \text{for the easy axes <110>} \qquad (4.1a)$$

and

$$\left(\frac{\omega}{\gamma}\right)^2 = 4\pi M_{eff}\left(H_{hard} + \frac{2K_{1\parallel}^{eff}}{M_s}\right) \quad \text{for the hard axes <100>.} \qquad (4.1b)$$

Equations (4.1) can be used to estimate the in-plane fourfold anisotropy, $\frac{2K_{1\parallel}^{eff}}{M_s}$:

$$\frac{2K_{1\parallel}^{eff}}{M_s} = \frac{H_{easy} - H_{hard}}{2} \qquad (4.2)$$

For example the resonance fields in the 4 ML Co sample, see Figure 4.1, result

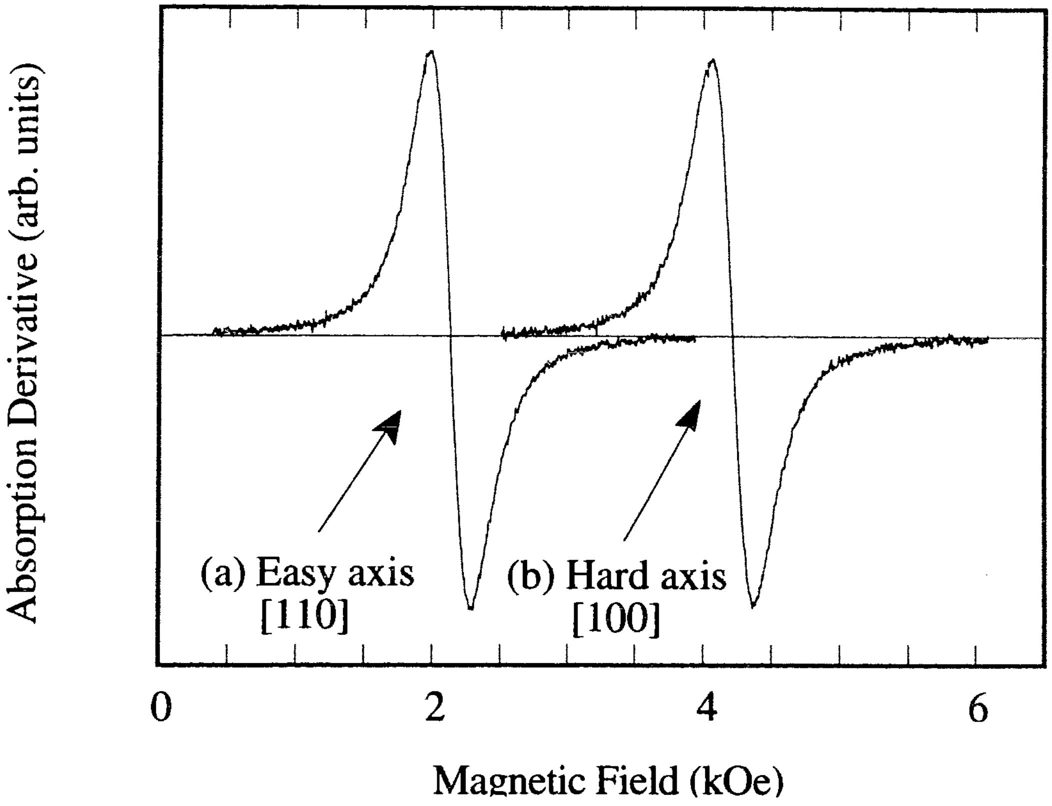

Figure 4.1 The FMR signal measured at 36.3 GHz (room temperature) for the Cu(001)/4Co/6Cu/20Au sample along the (a) easy and (b) hard magnetic axes. The shift in the resonance field between the easy and the hard axes is caused by the fourfold in-plane anisotropy field.

in $\frac{2K_{1\parallel}^{eff}}{M_s} \approx -1$ kOe. Then equation (4.1b) yields $4\pi M_{eff}$ ~ 46 kOe. This value is significantly larger than the saturation induction $4\pi M_S$ (17.87 kOe for hcp cobalt). Therefore, the film normal is a hard axis for the perpendicular uniaxial anisotropy, and the sample plane is an easy plane. The above approximate calculations immediately give one an idea about how strong the anisotropy fields are in fcc Co(001) structures.

4.2.1 Calculations of the g-factor.

In order to perform complete quantitative studies of the magnetic properties of fcc Co(001) films one needs to obtain a precise value of the gyromagnetic ratio γ (g-factor, see equation 3.5). This can be achieved by measurements of H_{res} for at least two sufficiently different microwave frequencies. In this work, the g-factor was calculated from the FMR measurements of the Cu/10Co/10Cu/20Au sample at 23.8, 36.3 and 72.9 GHz. It was found that the measurements carried out at 23.8 and 36.3 GHz alone did not provide reliable values for the g-factor and $4\pi M_{eff}$. The reason is that for low microwave frequencies the term H_{res} (< 5 kOe) which appears in the first bracket on right hand side of equation (3.58) can be neglected. In this case the measured resonance fields are able to determine well only the product $\left(\frac{\omega}{\gamma}\right)^2 \frac{1}{4\pi M_{eff}}$ (see equations (4.1)) and not the individual values for g-factor and $4\pi M_{eff}$. One needs to increase at least one of the microwave frequencies to bring H_{res} to a value which is not negligible compared to $4\pi M_{eff}$. FMR measurements at 72.9 GHz fulfilled this requirement (H_{res}~12kOe).

Accurate values of the g-factor, $4\pi M_{eff}$ and $\frac{2K_{1\parallel}^{eff}}{M_s}$ in the 10 ML Co sample were obtained by using a Surface Physics Laboratory program (written by Dr Urquhart). In this program equation (3.58) is used to fit the measured resonance fields $H_{res}(\varphi)$ at two different microwave frequencies. The 10 ML Co sample was measured at 23.8, 36.3 and 72.8 GHz. For 23.8 and 36.3 GHz the measurements were carried out along the easy and hard axes, while at

72.9 GHz a full angular dependence was obtained. From these measurements two groups of data were created. The first group used the results from 23.8 and 72.9 GHz measurements and the second group used the results from 36.3 and 72.9 GHz measurements. For each group a MINUIT minimization routine determined the self-consistent values of $4\pi M_{eff}$ and g-factor and the corresponding values of $\frac{2K_{1\parallel}^{eff}}{M_s}$ for each microwave frequency. The values of $4\pi M_{eff}$ and g-factor were determined by iteration using the resonance conditions at two microwave frequencies for each group of data starting at g=2. The results of these analyses are shown in Table 4.1.

The value of $4\pi M_{eff}$ was found weakly dependent (less than 1% variation) on the dc magnetic field. The g-factor was found to be almost independent of the field; its average value was found to be g = 2.16. The value of the in-plane 4-fold anisotropy, $\frac{2K_{1\parallel}^{eff}}{M_s}$ was found to depend somewhat on the field. It increased by 7-8% with an increasing dc field.

TABLE 4.1: Magnetic properties of Cu/<u>10Co</u>/10Cu/20Au sample at different microwave frequencies.

FREQUENCIES (Ghz)	$4\pi M_{eff}$ (kOe)	$\frac{2K_{1\parallel}^{eff}}{M_S}$ (kOe)	g
24 - 73	34.4	-1.26 (at 24GHz),-1.36 (at 73GHz)	2.16
36 - 73	34.6	-1.29 (at 36GHz),-1.36 (at 73GHz)	2.16

The above measurements of the same sample Cu/<u>10Co</u>/10Cu/20Au at 23.8, 36.3 and 72.9 GHz were also used to study the linewidth, ΔH, as a function of the microwave frequency f. The frequency dependence of the linewidth shows negligible zero frequency linewidth , ΔH(0) ~ 5 Oe, see equation (3.59). A low value of ΔH(0) shows that the Co ultrathin films exhibit very good macroscopic homogenities. From the slope of the linewidth versus frequency plot the Gilbert-damping coefficient was found to be $G = (3.1*10^8 \pm 0.2*10^8)\ \mathrm{sec}^{-1}$, see Figure 4.2.

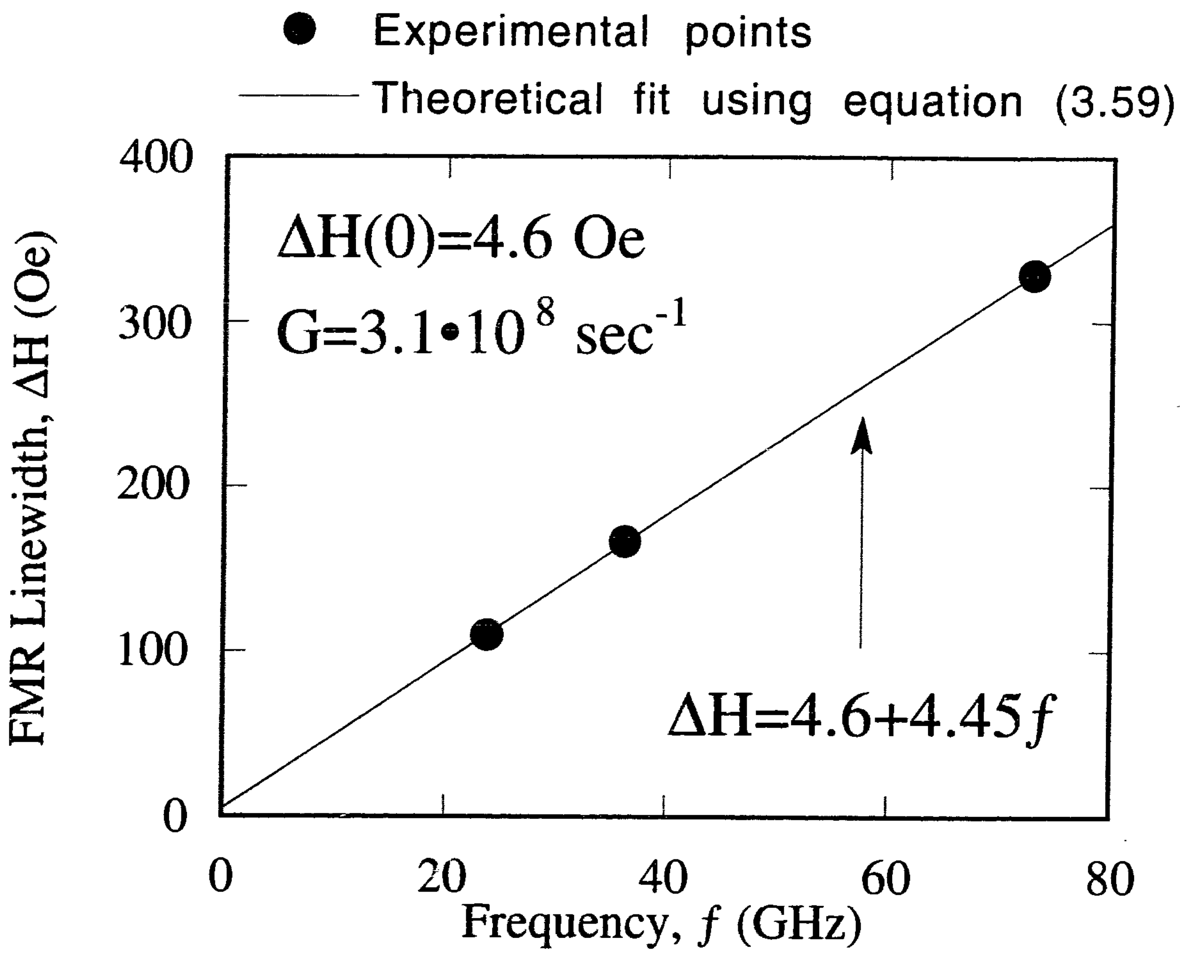

Figure 4.2 The plot of the linewidth, ΔH, as a function of the frequency, *f*, for the Cu(001)/<u>10Co</u>/10Cu/20Au sample. The linewidth, ΔH, was measured for the FMR signal at room temperature along the easy magnetic axis. Errors in the measured linewidth are smaller than 5% (error bars are smaller than the points).

4.2.2 Magnetic anisotropies

The remaining samples were measured at 36 GHz at room and liquid nitrogen temperatures. Due to a large in-plane fourfold anisotropy field the saturation magnetization $\mathbf{M_S}$ is not in general parallel with the dc field $\mathbf{H_{dc}}$. The angle $\varphi-\theta$ between $\mathbf{M_S}$ and $\mathbf{H_{dc}}$ depends on the orientation of $\mathbf{H_{dc}}$ with respect to the in-plane crystallographic axes. The anisotropy pulls $\mathbf{M_S}$ away from the direction of $\mathbf{H_{dc}}$ when the applied field is not along an easy crystallographic axis. However for the applied field directed along the hard axis the saturation magnetization, $\mathbf{M_S}$, is parallel with the field when $H_{dc} > \frac{2K_{1\parallel}^{eff}}{M_s}$. For our samples $H_{dc} > \frac{2K_{1\parallel}^{eff}}{M_s}$, and therefore the measurements of H_{res} carried out along the easy and hard axes were unaffected by dragging the saturation magnetization, $\mathbf{M_S}$, behind the d.c. field, $\mathbf{H_{dc}}$. The majority of the measurements were performed with the field applied along the easy and hard magnetic axes only for which $\mathbf{M_S}$ and $\mathbf{H_{dc}}$ are parallel. In this case equation (3.58) can be used with $\varphi=\theta$ and a set of equations for the easy and hard axes can be solved to obtain the values of the in-plane magnetic anisotropy and $4\pi M_{eff}$. The analyses were carried out using g=2.16 which was found for the Cu / <u>10Co</u> / 10Cu / 20Au sample, see Section 4.2.1. The saturation magnetization, M_S, was taken to be that of the bulk Co ($4\pi M_S$=17.87kOe). The results for all single-layer cobalt samples are summarized in Table 4.2 [4.1].

In order to study the in-plane fourfold anisotropy in more detail, an in-plane angular dependence of $H_{res}(\varphi)$ was measured for the trilayer sample Cu(001) / <u>4.3 Co / 6 Cu /4 Co</u> / 17 Cu / 20 Au at 36.3 GHz. The theoretical fit to the experimental data, $H_{res}(\varphi)$, must include the dragging angle $\varphi-\theta$. The MINUIT -based minimization program available in the Surface Physics

MINUIT -based minimization program available in the Surface Physics Laboratory was used to fit all the experimental points, $H_{res}(\varphi)$, with the formula (3.58) which accounts properly for the dragging angle $\varphi-\theta$, see Figure 4.3.

TABLE 4.2 : Single-layered Co samples grown on a Cu(001) substrate. All measurements were carried out at 36 Ghz. T_S is the temperature of the substrate during the growth of the Co layer. Data is presented in the face-centered tetragonal coordinate system where $\alpha_x, \alpha_y, \alpha_z$ are directional cosines with respect to <100> axes. See Appendix A for comparison of the fct and the bct coordinate systems. ($H_u = 2K_u^{eff}/M_s$). Errors in anisotropies are smaller than 5%.

		295K			77K		
SAMPLE	T_S (K)	H_u* (kOe)	$4\pi M_{eff}$ (kOe)	$\frac{2K_{1\parallel}^{eff}}{M_S}$ (kOe)	H_u* (kOe)	$4\pi M_{eff}$ (kOe)	$\frac{2K_{1\parallel}^{eff}}{M_S}$ (kOe)
1.7Co/11.5Cu/20Au	330	-15.5	30.9	-0.065	-39.9	55.3	-0.60
3.3Co/6Cu/20Au	375	-27.1	43.7	-0.85	-37.9	54.5	-2.09
4Co/6Cu/20Au	300	-26.4	43.3	-1.10	-34.4	51.2	-2.21
6.5Co/10.5Cu/20Au	300	-22.0	39.2	-1.25	-26.3	43.5	-2.04
8.6Co/10.5Cu/20Au	300	-20.4	37.8	-1.27	-23.5	40.9	-1.83
10Co/10Cu/20Au	355	-19.2	36.7	-1.29	-21.5	39.0	-1.81
4Co/3Fe/8.5Cu/20Au	300	X	16.2	-0.41	X	16.5	-0.60

* using $4\pi M_S = 17.87$ kOe for hcp Co.

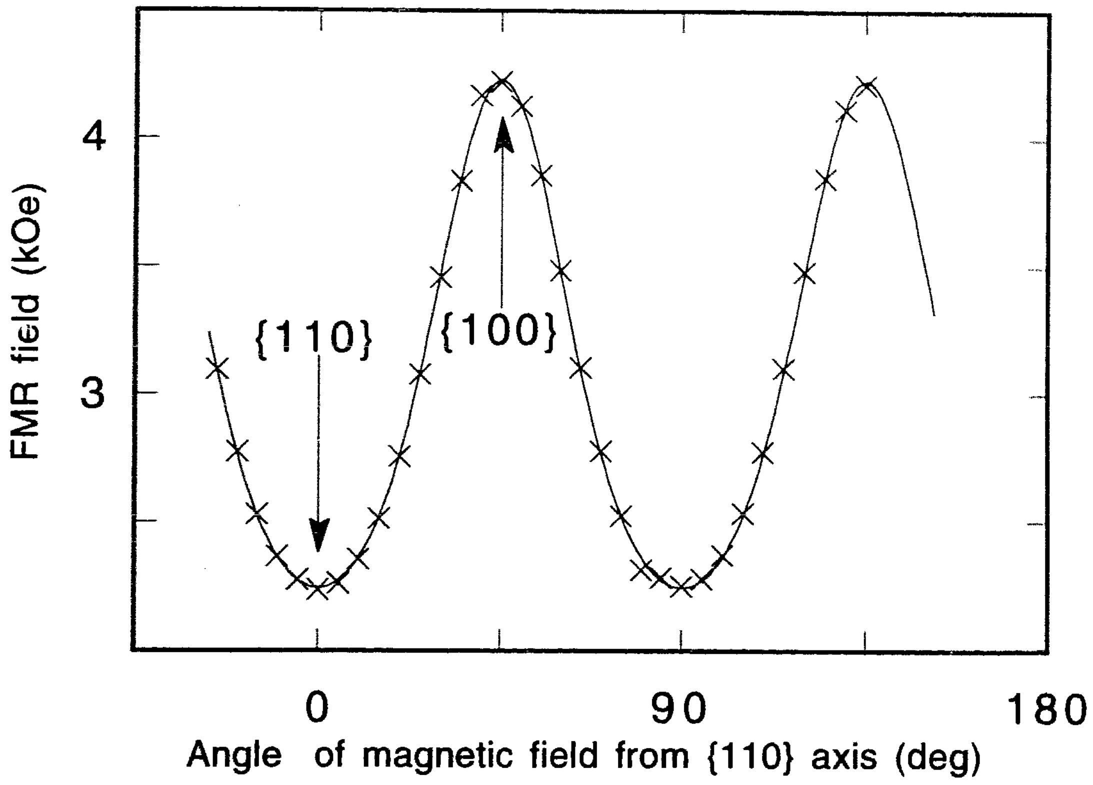

Fig. 4.3. The in-plane angular dependence of the resonance field, H_{res}, observed for the Cu(001)/4.3Co/6Cu/4Co/17Cu/20Au sample at 36.3 GHz. The solid line represents a theoretical fit using the following magnetic parameters: $4\pi M_{eff}$=40.8 kOe, $\frac{2K_{1\parallel}^{eff}}{M_s}$ = -1.05 kOe (obtained from Table 4.3).

Note that the FMR field around the easy magnetic axis changes more slowly with angle than around the hard axis. This behavior is caused by the dragging of the saturation magnetization behind the external field due to a strong in-plane 4-fold anisotropy.

A. Perpendicular uniaxial anisotropies

The single-layered Co samples show large negative uniaxial anisotropy fields indicating that the film surface is an easy plane (or, in other words, the surface normal is the hard axis) (see table 4.2). The uniaxial anisotropy is the result of magnetocrystalline and magnetoelastic energies. The shape anisotropy due to demagnetizing fields is eliminated from the uniaxial anisotropy by using the formula (3.53) for a finite fcc lattice, see Chapter 3 :

$$H_u = \frac{2K_u^{eff}}{M_s} = 4\pi\left(1 - \frac{0.2338}{d}\right)M_s - 4\pi M_{eff} \tag{4.4}$$

where d is the film thickness in monolayers (ML). The thickness dependence of $\frac{2K_u^{eff}}{M_s}$ is shown in Figure 4.4a for liquid-nitrogen and in figure 4.4b for room temperature. At both temperatures the uniaxial anisotropy field can be fit with a constant plus a term dependent on 1/d:

$$\frac{2K_u^{eff}}{M_s} = \left[-13.6 - 82.2\frac{1}{d}\right] \text{ kOe at LN}_2\text{ T} \tag{4.5a}$$

$$\frac{2K_u^{eff}}{M_s} = \left[-15.2 - 42.5\frac{1}{d}\right] \text{ kOe at room T} \tag{4.5b}$$

where d is in monolayers (ML). The sample with 1.7 monolayers of Co from Table 4.2 is omitted from the fitting procedure at 295K, because its Curie temperature is below room temperature [3.10,4.2]. The case of liquid nitrogen will be addressed in the discussion. Corresponding anisotropy constants are:

at liquid nitrogen temperature,

$$K_u^{bulk} = -9.63 \cdot 10^6 \ \frac{\text{erg}}{\text{cm}^3} = -0.963 \ \frac{\text{MJ}}{\text{m}^3} \tag{4.6a}$$

$$K_u^S = -0.508 \ \frac{\text{erg}}{\text{cm}^2} = -0.508 \ \frac{\text{mJ}}{\text{m}^2} \tag{4.6b}$$

and at room temperature,

$$K_u^{bulk} = -10.8 \cdot 10^6 \ \frac{\text{erg}}{\text{cm}^3} = -1.08 \ \frac{\text{MJ}}{\text{m}^3} \tag{4.6c}$$

$$K_u^S = -0.263 \ \frac{\text{erg}}{\text{cm}^2} = -0.263 \ \frac{\text{mJ}}{\text{m}^2} \tag{4.6d}$$

The shape anisotropy contribution to the bulk and the surface terms has already been subtracted using formula (4.4). The surface term value is quoted per one interface.

B. Fourfold in-plane anisotropies

The strong negative fourfold in-plane anisotropy fields favor the <110> as the easy axes (see table 4.2). The thickness dependence of this anisotropy is shown in Figure 4.5a for liquid-nitrogen and in Figure 4.5b for room temperature. Again, a constant plus a term dependent on 1/d was used to describe the behavior:

$$\frac{2K_{1\parallel}^{eff}}{M_s} = \left[-1.51 - 3.01\frac{1}{d}\right] \ \text{kOe} \ \text{ at } \text{LN}_2 \ \text{T} \tag{4.7a}$$

$$\frac{2K_{1\parallel}^{eff}}{M_s} = \left[-1.41 + 1.17\frac{1}{d}\right] \text{ kOe at room T} \tag{4.7b}$$

where d is in ML. Samples 1.7 ML and 3.3 ML of Co were omitted from the fit as will be explained in the discussion. The values of bulk and surface anisotropy constants are given below for reference:

at liquid nitrogen temperature,

$$K_{1\parallel}^{bulk} = -1.07\cdot 10^{6}\ \frac{\text{erg}}{\text{cm}^3} = -0.107\ \frac{\text{MJ}}{\text{m}^3} \tag{4.8a}$$

$$K_{1\parallel}^{S} = -1.86\cdot 10^{-2}\ \frac{\text{erg}}{\text{cm}^2} = -1.86\cdot 10^{-2}\ \frac{\text{mJ}}{\text{m}^2} \tag{4.8b}$$

at room temperature,

$$K_{1\parallel}^{bulk} = -1.00\cdot 10^{6}\ \frac{\text{erg}}{\text{cm}^3} = -0.100\ \frac{\text{MJ}}{\text{m}^3} \tag{4.8c}$$

$$K_{1\parallel}^{S} = 7.24\cdot 10^{-3}\ \frac{\text{erg}}{\text{cm}^2} = 7.24\cdot 10^{-3}\ \frac{\text{mJ}}{\text{m}^2} \tag{4.8d}$$

The value of the surface terms correspond to one interface only.

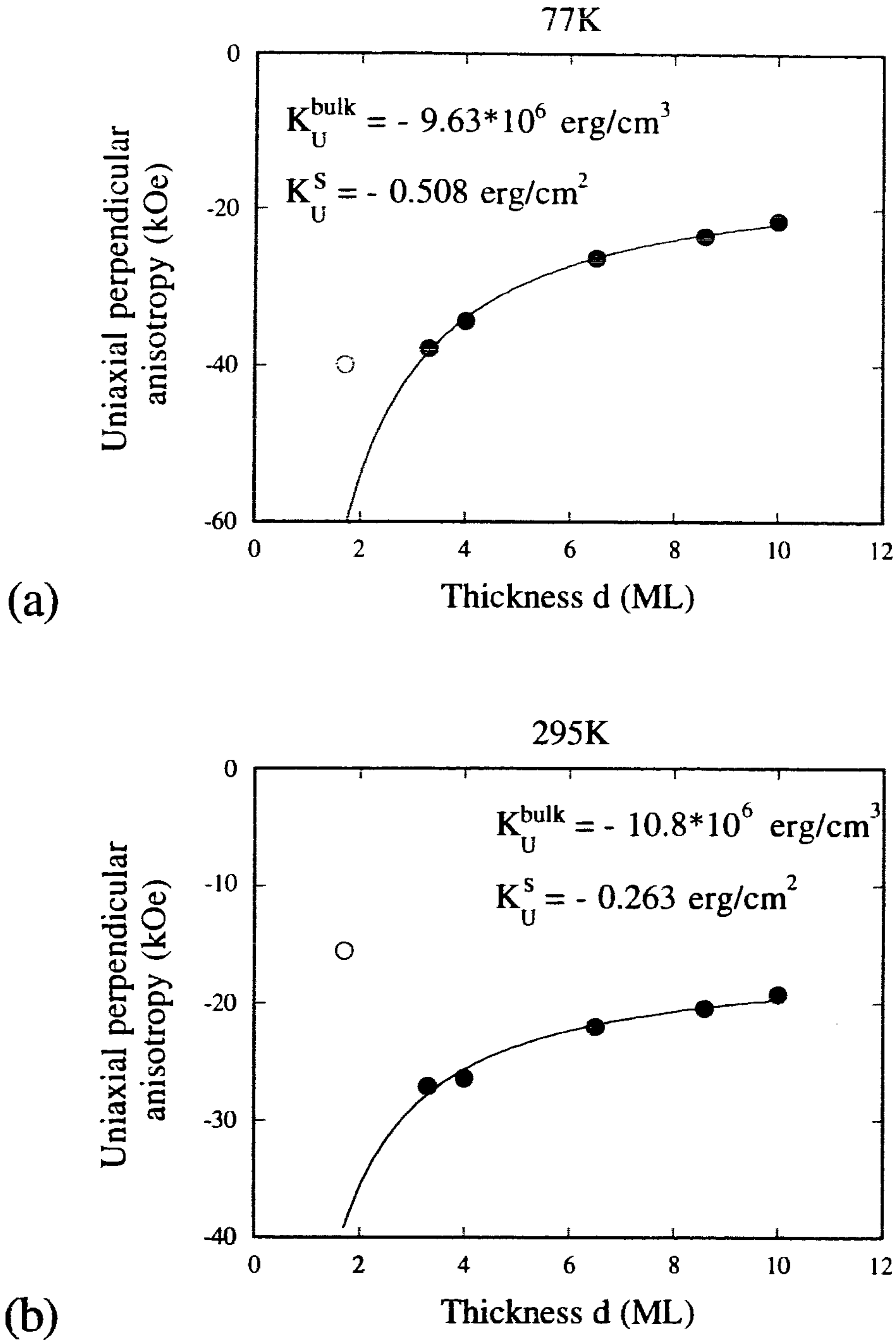

Fig. 4.4. The perpendicular uniaxial anisotropy as a function of thickness of Co(001) film for (a) 77 K and (b) 295 K. The full circles indicate experimental data used to fit the bulk and surface contributions to anisotropy as described by equations (4.5) in the text. The empty circles indicate the 1.7 ML Co sample.

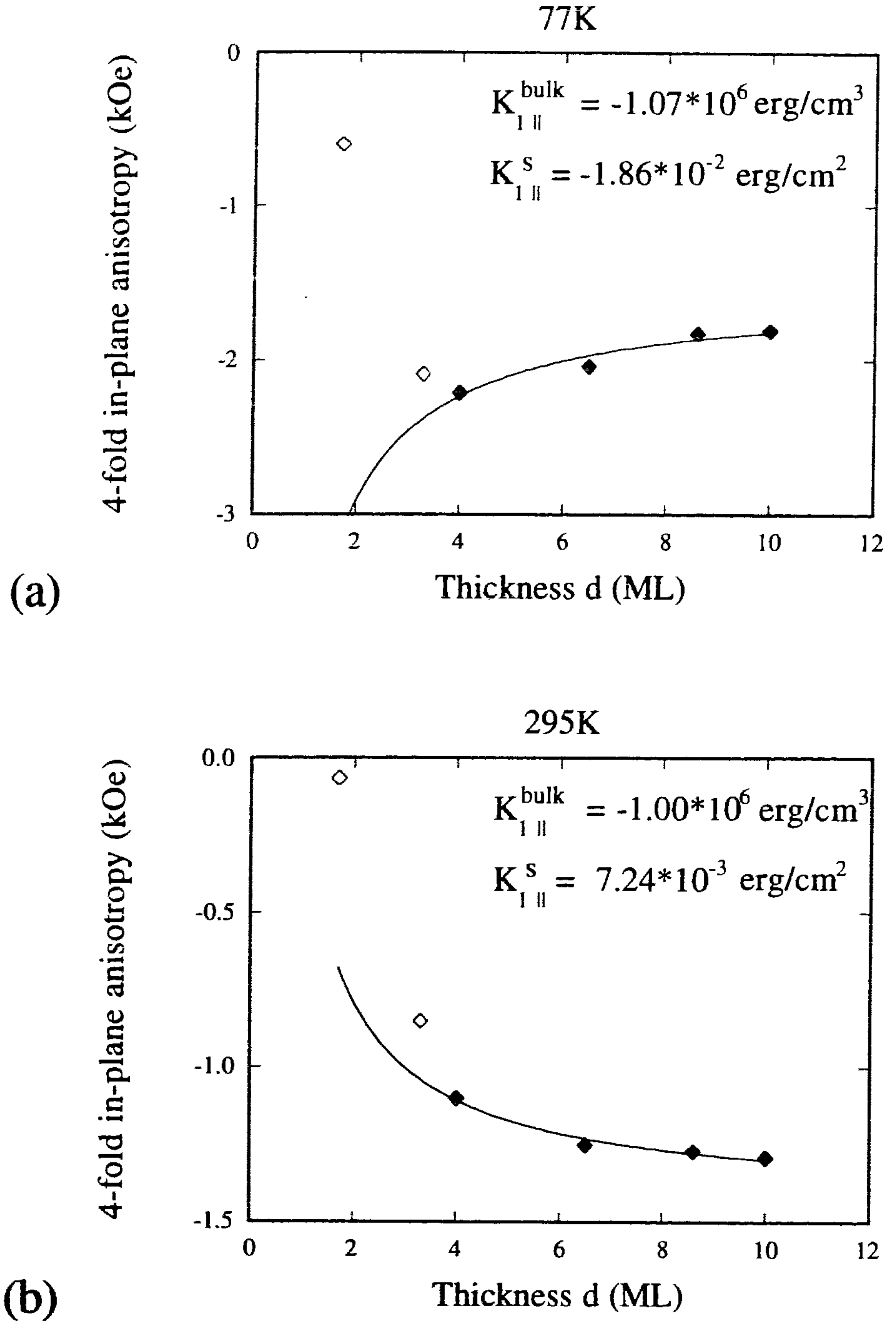

Fig. 4.5. The fourfold in-plane anisotropy as a function of thickness of Co(001) for (a) 77 K and (b) 295 K. The full diamonds indicate experimental data used to fit the bulk and surface contributions to anisotropy as described by equations (4.7).The empty diamonds indicate the 1.7 and 3.3 ML Co samples (not used in the data fit).

3.2.4 Discussion

For an ideal fcc lattice there would be no crystalline bulk contribution to the perpendicular uniaxial anisotropy. Therefore, the large negative constant terms in equations (4.5) are a consequence of the tetragonal distortion of a Co lattice grown on Cu(001). This contribution favors the surface of the film as an easy plane. The thickness dependent part of $\frac{2K_u^{eff}}{M_s}$ is well described by the 1/d term, and it also favors an easy plane. LEED studies indicate a constant and homogenous strain for Co/Cu(001) films thicker than 4 ML [2.10], see Chapter 2. Therefore the interface anisotropies are most likely responsible for the measured 1/d terms in these films. This is similar to Co/Pd(001) superlattices where the strain was also found to be independent of the Co layer thickness up to 6 ML [4.3]. However, this stands in contrast with Co/Cu(111) superlattices for which the measured apparent surface anisotropies are a consequence of the magneto-elastic energy with strains inversely proportional to the Co layer thickness [4.4]. Our results indicate that, additionally to 6.5, 8.5 and 10 ML Co, the 4 ML Co/Cu(001) sample also follows the constant strain behavior. But thinner samples deviate from the constant plus thickness dependent term behavior predicted by equations(4.5) and (4.7): this deviation is discussed below.

The 1.7 ML sample for both the uniaxial and the in-plane anisotropies and the 3.3 ML sample for the 4-fold in-plane anisotropy were excluded from the fitting procedure which led to equations (4.5) and (4.7). The reason for this is two-fold. Firstly, as mentioned in the Chapter 2, detailed LEED investigations revealed that the strain in Co films thinner than 4 ML is thickness dependent. For Co coverages less than 4 ML the tetragonal distortions are smaller [2.10], thus resulting in the reduction of the magneto-elastic volume contribution to the magnetic anisotropies. Secondly, scanning tunneling microscopy (STM) studies of Co grown on Cu(001) [4.5], and our reflection high-energy electron-diffraction (RHEED) oscillations, see Chapter 2, indicate that the first two layers of Co exhibit a deviation from layer-by-layer growth. Islands belonging to the second atomic layer are created before the first layer is completed. Such roughness causes local demagnetizing fields at the surface which tend to decrease the surface anisotropy (make it less negative). Hence, for samples thinner than 4 ML, the deviation from the simple constant volume and 1/d dependent surface term behavior is due to both smaller tetragonal distortions and increased film roughness.

The role of surface roughness and changing lattice strains discussed above is visible in the measured uniaxial and in-plane anisotropies plotted in Figures 4.4 and 4.5. While the magnitude of the uniaxial anisotropy of the 1.7 ML sample at 295K is strongly decreased as compared to the value given by equation (4.5) (by ~60%, see Figure 4.4(b)) mainly because the Curie point is just below room temperature [3.10], the observed lower magnitude (by ~20%, see Figure 4.4(a)) of the uniaxial anisotropy at 77K (well below Tc) is attributed mostly to reduced strain and increased surface roughness. Those effects are even more pronounced in the 4-fold in-plane anisotropy. At both 77K and 295K temperatures the magnitude of the fourfold in-plane anisotropy of the 1.7 ML Co sample is decreased by ~80% and ~90% respectively, see Figure 4.4. The 3.3 ML sample showed an appreciably smaller change in the in-plane anisotropy; 12% at LN_2 temperature, and 19% at room temperature. Considering the fact that the Co film surface topology does not change for thicknesses greater than 3 ML, this reduction can be attributed mainly to the reduced strain in the 3.3 ML thick Co sample.

The value of the bulk contribution to the uniaxial anisotropy can be estimated using the magnetoelastic energy for a tetragonally distorted cubic lattice [4.6]:

$$E_{magel} = B_1\left(e_{xx}\alpha_x^2 + e_{yy}\alpha_y^2 + e_{zz}\alpha_z^2\right) \tag{4.9}$$

For the case of equal in-plane expansion ($e_{xx}=e_{yy}=e_{\|}$ and $e_{zz}=e_{\perp}$) equation (4.9) can be simplified to (using the identity $\alpha_x^2 + \alpha_y^2 + \alpha_z^2=1$)

$$E_u^{mag.el.} = const + B_1\left(e_{\perp} - e_{\|}\right)\alpha_z^2 \tag{4.10a}$$

where

$$B_1 = -\frac{3}{2}\lambda_{100}\left(c_{11} - c_{12}\right) \tag{4.10b}$$

Here $e_{\perp}, e_{\|}$ are the in-plane and the perpendicular strain tensor components, λ_{100} is the magnetostriction constant, and c_{11}, c_{12} are the elastic moduli. The strains quoted in Chapter 2 give $e_{xx}=e_{yy}=e_{\|}=0.0175$ and $e_{zz}=e_{\perp}=-0.022$. The elastic constants for fcc Co are $c_{11}=2.42\text{x}10^{12}$ ergs/cm^2, $c_{12}=1.60\text{x}10^{12}$ ergs/cm^2 [4.7]. In order to explain the strength and sign of the volume contribution to the perpendicular uniaxial anisotropy using the above strains and elastic constants one needs to use a positive magnetostriction constant of $\lambda_{100}\approx 2.2\times 10^{-4}$ for the lattice strains observed in fct Co. This value is about a factor of two larger than those found in Co rich fcc Pd-Co alloys ($\lambda_{100}\approx 1.3\times 10^{-4}$) [4.8], and has the same sign and order of magnitude as magnetostriction constants of Co-Fe and Co-Ni alloys. In addition, the bulk uniaxial anisotropy constant for fcc Cu(001)/Co films, $K_u^{bulk} = -10.8 \cdot 10^6 \ \frac{\text{ergs}}{\text{cm}^3}$, and that for fcc Pd(001)/Co films, $K_u^{bulk} = -3.2 \cdot 10^7 \ \frac{\text{erg}}{\text{cm}^3}$, [4.9, 4.10] have the same sign and the ratio ($3.2 \cdot 10^7 \div 10.8 \cdot 10^6 = 2.96$) which is not far away from the ratio of their vertical compressions (2.2%÷9.6%=4.36 [ref.4.9]). This emphasizes the importance of tetragonal distortions for the strength of uniaxial anisotropies. The linear magnetoelastic theory applied to tetragonally distorted structures is fairly successful in, at least, qualitative predictions of the bulk contribution to uniaxial anisotropies.

In contrast to our Co/Cu(001) films, surface contributions to the uniaxial anisotropy in Co/Pd(001),(110),(111) [4.10] and Co/Pt(001),(110),(111) [4.11,4.12] films are positive favoring the film normal as the easy axis. A negative value of the surface anisotropy in Co/Cu(001) structures is very surprising considering the fact that even the formation of an ordered alloy ($CoPt_3$) in Co/Pt interfaces did not result in substantial modification of surface anisotropies [4.13, 4.14]. Recent *ab initio* band structure calculations [4.15] predict that the interface uniaxial anisotropy of an uncovered fcc Co(001) atomic layer grown on a Cu(001) substrate has a total anisotropy $K_u^s = -\ 0.8 \frac{ergs}{cm^2}$, but a Co(001) covered by Cu(001) layer has nearly zero positive interface anisotropy. Our results contradict these theoretical calculations. The interface anisotropy constant is definitely a non negligible negative number at room temperature, $K_u^s = -\ 0.26 \frac{ergs}{cm^2}$, which becomes larger in magnitude when cooled to a liquid nitrogen temperature, $K_u^s = -\ 0.51 \frac{ergs}{cm^2}$, see equations (4.6b) and.(4.6d). However, our samples are thicker than one monolayer and they are significantly strained; they perhaps exhibit a different behavior than the single monolayer which was used in the theoretical predictions in reference 4.15.

Recently, magnetic anisotropies of Co grown on Cu(001) have been determined by Brillouin light scattering [4.16]. Studies of the fourfold in-plane anisotropy by Krams et al showed the same sign and order of magnitude for volume and surface contributions as our results. The uniaxial perpendicular anisotropy determined in that paper, however, did not exhibit the volume contribution apparent from our studies, and for Co covered with 2 ML Cu, the thickness dependent term indicated that the surface normal was an easy axis in disagreement with our result. The absence of a bulk contribution to the uniaxial anisotropy in their result is very surprising since tetragonal distortions of Co(001) grown on Cu(001) are expected to lead to a large volume uniaxial anisotropy as indicated by equations (4.10).

Calculations based on Néel's model predicted perpendicular surface anisotropies for Co/Au and Co/Cu texturized films in accordance with experiment [4.17]. It is therefore interesting to compare our results with the value of the surface uniaxial anisotropy calculated from Néel's model. In Neel's theory the interactions between two atomic magnetic moments separated by a vector **r** are given by:

$$w(r) \approx l(r)\cos^2\phi + q(r)\cos^4\phi \tag{4.11}$$

where l and q are Neel's coefficients of pair interaction, r is the distance between the atoms, and ϕ is the angle between vector **r** and magnetic moments. The Neel coefficient l can be estimated from magnetoelastic constants [4.6]. Using the magnetoelastic constants for hcp Co, Bruno [4.17] obtained the value of l=6.1×10^{-16}. Using Neel's model one can show that the surface anisotropy in the fcc Co(001) surface is given by:

$$K_u^s = \frac{l}{a^2} = 0.47\frac{ergs}{cm^2} \tag{4.11}$$

where a is the in-plane lattice constant. The positive value for K_u^s indicates a perpendicular easy axis surface anisotropy for the case of Co(001), in contradiction to our experimental results. This should not be too surprising since Néel's approach assumes a free surface, not a covered one, as was investigated in our studies. Our results suggest that predictions of the behavior of the surface anisotropy invoking Néel's coefficients determined from the bulk magnetoelastic model have to be treated with some caution.The thickness dependent part of the uniaxial anisotropy is strongly dependent on temperature, while the thickness independent part does not change appreciably upon cooling to liquid nitrogen temperature. A 10% change in the volume term can be attributed to the temperature dependence of the magnetostriction constant in equation (4.10b). For example for fcc Ni, the change in magnetostriction constant λ_{100} upon cooling from 300 K to 77 K is approximately 9% [4.18]; therefore, λ_{100} for fcc Co might show a similar change. In order to explain the temperature dependence of the 1/d term using the renormalized surface anisotropy due to fluctuations caused by 2-D spin wave theory [4.19] one needs a decrease in saturation magnetization of approximately 17%. Unfortunately, the author is not aware of any published studies related to the dependence of the magnetization on temperature for samples 4 ML and thicker of Co grown on Cu(001).

The fourfold in-plane anisotropy has a large constant term due to lattice strains and a 1/d dependent term most likely due to a surface fourfold in-plane anisotropy. The constant term favors <110> as easy axes at both liquid nitrogen and at room temperature. The temperature dependence of the thickness dependent term is striking: at LN_2 temperature its negative value also prefers <110> as an easy axis, but upon heating to room temperature the sign changes and favors <100> as the easy axis, see equations (4.7). Such behavior is not likely due to thermal fluctuations; for samples 3 ML and thicker the critical point is above 600 K [3.10], and hence at room temperature the thermal fluctuations should be negligible [4.20]. This reversal in sign of the thickness dependent term upon heating from 77 K to 300 K might be caused by a complex dependence of the spin-orbit contribution to the 3d valence-band energies on the sample temperature. On the other hand, the volume term is not significantly affected by the temperature change. This is in complete contrast with bcc Fe [4.6] for which the thickness independent part changes by nearly 30% upon cooling from room to liquid nitrogen, but the 1/d term remains virtually unchanged.

The microwave losses are studied by the ferromagnetic resonance linewidth, ΔH. The FMR linewidth is usually characterized by the zero frequency linewidth, ΔH(0), and by the Gilbert damping, G, see Section 3.8. Figure 4.2 shows that ΔH(0) was found to be ~5 Oe. This is a unique case. For example in the case of Fe the zero frequency linewidth, ΔH(0), was 70 Oe for a 10 ML iron film [4.21]. ΔH(0)~5 Oe testifies to a good macroscopic homogeneity of the Co films. The Gilbert damping parameter, $3.1\text{x}10^8$ sec^{-1}, is three times larger than that in hcp Co ($G = 1\text{x}10^8$ sec^{-1}) [4.22] and significantly larger than that observed in Fe films and in bulk Fe [4.21, 4.23] ($G = 0.84\ \text{x}10^8$ sec^{-1}), but it is comparable to the Gilbert damping for bulk Ni [4.24] (2.45 x10^8 sec^{-1}). It is interesting to note that the g-factors for fcc Co (g=2.16), hcp Co (g=2.18)and for fcc Ni (g=2.19) are also similar. The deviation of the g-factor from its free electron value (g = 2.0) reflects the contribution of the spin-orbit coupling to the 3d valence band magnetic moments. Moreover the intrinsic damping and the magnetic anisotropies in 3d metals also originate in the spin-orbit interaction [4.25]. The cubic anisotropy in bulk Ni is large at cryogenic temperatures (-2.7 kOe at LN_2) and it is negative as in fcc Co layers (e.g. -2.2 kOe for 4 ML thick Co), see Table 4.2. Therefore the similar behavior of the g-factors, the 4 fold crystalline anisotropies and the intrinsic Gilbert damping parameters in fcc Co and fcc Ni suggests that the contributions of the spin orbit interaction to their 3d bands are very similar.

4.3 Exchange coupling between Co layers

FMR measurements are very useful for the study of the magnetic coupling between ferromagnetic layers. The theory of exchange coupled ultrathin trilayers (two ferromagnetic layers separated by a non-magnetic interlayer) has been extensively reviewed [4.26,4.27,4.28]. Here a summary of the main features which are relevant to the measured results are presented. As pointed out in Chapter 3 the magnetic moments within each ferromagnetic layer precess together as a unit. The interlayer exchange interface energy per unit area, E_{ex}, can be written in the form:

$$E_{ex} = - J \frac{\mathbf{M}_1 \cdot \mathbf{M}_2}{M_1 M_2} , \qquad (4.18)$$

where J is the exchange coupling coefficient between the layers, $\mathbf{M}_1$ and $\mathbf{M}_2$ are the saturation magnetizations in the individual films. The exchange coupling between two ferromagnetic layers leads to two precessional modes. For the acoustic mode the magnetic moments precess in phase; for the optical mode the magnetic moments in the two films precess out-of-phase. The character of the magnetic coupling can be determined from the relative positions of the acoustic and the optical modes. For the antiferromagnetic coupling the optical mode is located at a higher field than the acoustic mode. For the ferromagnetic coupling the situation is reversed: the optical peak is located at lower fields than the acoustic peak. The positions and the intensities of both modes depend in a complicated way on the strength of the exchange coupling, but they can be calculated using the L.-L. equations of motion which include the effective fields arising from the exchange coupling [4.26]. One should point out that the optical mode is only observable in FMR measurements if the individual ferromagnetic layers in the absence of exchange coupling have different resonance fields [4.26]. The coupling to the RF driving field is very weak if the two films have identical magnetic properties.

Recent measurements [4.29] have shown that the fcc Co sandwiched between two Cu layers can result in antiferromagnetic coupling between the Co films. We have investigated the exchange coupling in several Co-Cu trilayer samples [3.10]:

(a) Cu/4Co/6Cu/10.3Co/11Cu/20Au,
(b) Cu/4Co/6Cu/4Co/3Fe/6Cu/20Au,
(c) Cu/4.3Co/6Cu/4Co/17Cu/20Au,
(d) Cu/4Co/10Cu/10Co/10Cu/20Au.

The layers participating in the magnetic coupling are underlined and the underlined parts (with integer numbers only) will be used to identify these specimens. The FMR technique was used to investigate the exchange coupling in these structures.

4.3.1. Ferromagnetic Resonance on 4Co/6Cu/10.3Co

The magnetic properties of the individual Co films give sufficiently different resonance fields (The resonance fields in 10 ML Co and 4 ML Co films were 0.32 and 0.66 kOe apart along the easy and hard axes respectively) so that FMR could be used to measure a moderately strong exchange coupling in the trilayer systems. Indeed the sample 4Co/6Cu/10Co exhibited optical peaks at larger fields than the acoustic mode peaks and this clearly indicated a weak antiferromagnetic coupling at both room and at LN$_2$ temperatures, see Fig.4.6. It is surprising that the optical peaks were very weak in spite of the fact that they were close in field to their respective acoustic peaks. The weak optical peaks indicated that the magnetic properties of the individual Co layers changed significantly as a result of their incorporation into a trilayer structure with the result that their resonance fields were even closer than those of the single layers.

Computer fits of the 4Co/6Cu/10Co trilayer data were carried out by adjusting the values of $4\pi M_{eff}$ (in each constituent layer), the in-plane anisotropy $\frac{2K_{1\parallel}^{eff}}{M_s}$, and the exchange coupling between layers, see Figs 4.6(c) and 4.6(d). Unambiguous fits were possible to achieve since the low intensity of the optical mode required the magnetic properties of the constituent layers to be nearly the same. The position of the acoustic peak provided a good starting estimate of $4\pi M_{eff}$ for the thicker Co layer. The exchange coupling was estimated from the position of the optical mode. The value of $4\pi M_{eff}$ for the thinner layer was then determined from the intensity

TABLE 4.3: Magnetic properties of multilayered samples. All growths carried out at 300K except for the sample marked (*).

	295K						77K					
	$4\pi M_{eff}$ kOe		$\frac{2K^{eff}_{1\|\|}}{M_s}$ kOe		J_{easy} $\frac{ergs}{cm^2}$	J_{hard} $\frac{ergs}{cm^2}$	$4\pi M_{eff}$ kOe		$\frac{2K^{eff}_{1\|\|}}{M_s}$ kOe		J_{easy} $\frac{ergs}{cm^2}$	J_{hard} $\frac{ergs}{cm^2}$
layer A layer B	layer A	layer B	layer A	layer B			layer A	layer B	layer A	layer B		
4Co/6Cu/10.3Co/11Cu/20Au *	37.3	34.2	-1.22	-1.18	-.052	-.025	39.2	31.3	-2.01	-2.01	-.061	++
4Co/6Cu/4Co/3Fe/6Cu/20Au	41.9	16.3	-1.10	-.414	.071	.071	48.1	15.6	-2.21	-0.60	++	0.26
4Co/6Cu/10.5Co/10.7Cu/20Au (+)	36.6		-1.27		N/A	N/A	39.7		-1.73		N/A	N/A
4.3Co/6Cu/4Co/17Cu/20Au (+)	40.8		-1.05		N/A	N/A	50.9		-1.69		N/A	N/A
4Co/10Cu/10Co/10Cu/20Au (+)	39.6		-1.00		N/A	N/A	40.1		-1.94		N/A	N/A

* Different growth conditions: 4Co at 375K, 6Cu at 410K, 10Co at 345K

\+ No optical mode visible

++ For samples 4Co/6Cu/10Co/11Cu/20Au and 4Co/6Cu/4Co/3Fe/6Cu/20Au the optical peaks were out of the magnetic field range at 77K for hard and easy axis, respectively. For these cases the computer fits were carried out for the axes which had both the optical and the acoustic peaks available. The anisotropies for the 4Co/6Cu/10Co trilayer were taken as an algebraic mean of the single film anisotropies from Table 4.2. The anisotropies in 4Co/6Cu/4Co/3Fe multilayer were taken to be identical to those of measured single films, see Table I and text.

Fig. 4.6 The FMR signal in the 4Co/6Cu/10.3Co sample along the (a) easy and (b) hard magnetic axes at 36.3 GHz and T=300 K. Note that the optical peaks are weak and occur at higher fields than the acoustic peaks, and therefore the exchange coupling between the Co layers is antiferromagnetic. Note also that the optical peak along the hard axis lies closer to its acoustic counterpart than that along the easy axis. This shows that the exchange coupling is stronger along the easy axis. (c) and (d) are the calculated FMR lines using the theory of the exchange coupled bilayers for the sample whose measurements are shown in (a) and (b). The magnetic parameters for the 4ML (A) and 10.3ML (B) of Co(001) films were determined by fitting the positions and intensities of both the acoustic and optical peaks. The best fits were obtained by using the following parameters: $\left(\frac{2K_{1\|}^{eff}}{M_s}\right)^{(A)} = -1.22$ kOe, $\left(\frac{2K_{1\|}^{eff}}{M_s}\right)^{(B)} = -1.18$ kOe, $(4\pi M_{eff})^{(A)} = 37.3$ kOe, $(4\pi M_{eff})^{(B)} = 34.2$ kOe (see Table 4.3). The exchange coupling along the easy axis, $J_{easy} = -0.052$ ergs/cm^2, is higher than that observed for the hard axis, $J_{hard} = -0.025$ ergs/cm^2.

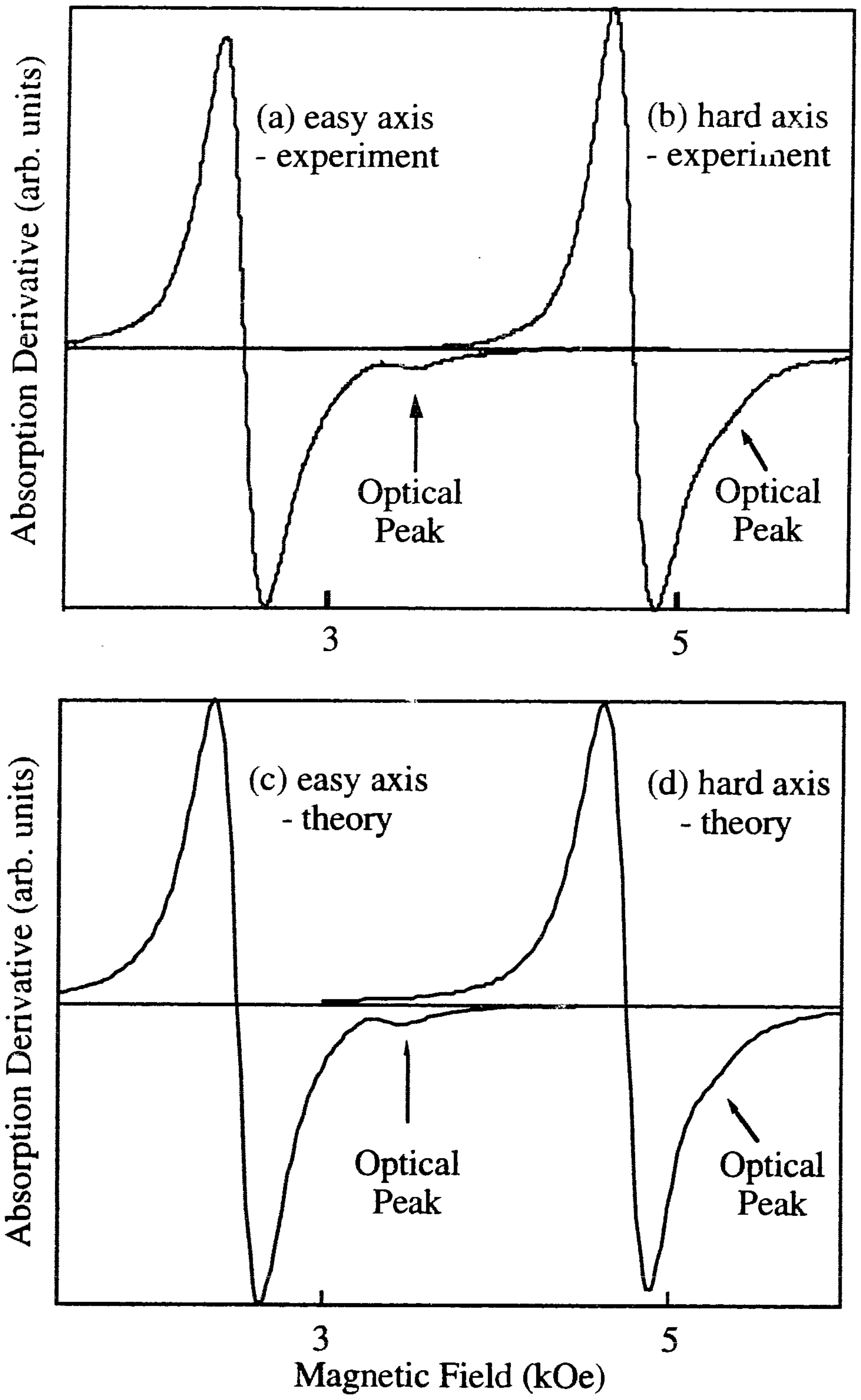
Absorption Derivative (arb. units)
(a) easy axis
- experiment
(b) hard axis
- experiment
Optical
Peak
Optical
Peak
3
5
Absorption Derivative (arb. units)
(c) easy axis
- theory
(d) hard axis
- theory
Optical
Peak
Optical
Peak
3
5
Magnetic Field (kOe)

of the optical mode. Measurements along the hard and easy magnetic axes determined the in-plane crystalline anisotropy. Fits were carried out iteratively until good agreement was achieved in the resonance peak positions and in the relative intensities of the measured optical and acoustic peaks, along both the hard and easy magnetic axes. Results of this analysis are shown in Table 4.3. Note that the value of $4\pi M_{eff}$ obtained for the thinner Co layer was found to be substantially smaller than that obtained from measurements on a single layer. The lattice strains in the trilayer structures may be decreased compared with strains in the single layer structures. A relaxation of lattice strains would result in lower perpendicular uniaxial anisotropies. It is also interesting to point out that the strength of the antiferromagnetic exchange coupling is not isotropic. It is noticeably larger along the easy axis (-.05 ergs/cm^2) than along the hard axis (-.028 ergs/cm^2).

4.3.2. Ferromagnetic Resonance on 4Co/6Cu/4Co/3Fe

In order to increase the difference in resonance fields in the Co layers the outer Co/Cu interface was changed. The sample Cu/4Co/3Fe/9Cu/20Au was grown. It exhibited the magnetic properties of a well behaved ferromagnetic film, see Table 4.2. The magnetic properties of the Cu/4Co/3Fe/Cu film were very different from those measured for a single separate Co layer, see Table 4.2. The presence of the Fe significantly decreased $4\pi M_{eff}$. In fact, $4\pi M_{eff}$=16.2 kG, in the Cu/4Co/3Fe/Cu sample is very close to the saturation induction of fcc Co(001). Most likely this is because the uniaxial anisotropy is significantly decreased. The in-plane 4-fold anisotropy was also strongly decreased, $\frac{2K_{1\parallel}^{eff}}{M_s}$ = -0.41 kOe compared with -1.10 kOe for Cu/4Co/6Cu/20Au. The magnetic properties of the

4Co/3Fe layer are close to an average of those observed for individual 4Co and 3Fe layers.

The FMR fields in the Cu/4Co/Cu and Cu/4Co/3Fe/Cu samples were very different. The resonance fields along the easy and hard axes differed by 4 and 4.6 kOe respectively. Their magnetic properties were different enough, see Table 4.2, so that a trilayer sample consisting of those structures separated by a Cu spacer was well suited for the study of the magnetic coupling using the FMR technique.The trilayer sample 4Co/6Cu/4Co/3Fe was grown and indeed the optical peaks were clearly visible, see Fig. 4.7. The optical peaks were found at smaller fields than the acoustic peaks. The 4Co and 4Co/3Fe layers were coupled ferromagnetically. The addition of a 3 ML Fe film on the outside of the Co layer changed the sign of the exchange coupling between the two Co layers. In contrast to the 4Co/6Cu/10Co trilayer, the FMR measurements in this sample were very easy to interpret. One did not have to change the magnetic properties of the individual layers in order to get a good fit between theory and experiment, see Tables 4.2 and 4.3. The exchange coupling was the only important parameter which was adjusted to fit the data obtained for fields along both the easy and the hard magnetic axes, see Table 4.3. In contrast with the 4Co/6Cu/10.3Co trilayer, the metastable 4 ML Co film in the 4Co/6Cu/4Co/3Fe trilayer did not appear to change its magnetic anisotropies.

The ferromagnetic exchange coupling in the 4Co/6Cu/4Co/3Fe trilayer was found to be isotropic and to increase rapidly upon cooling. At LN$_2$ temperatures it increased by 3.5 times; this is very close to the ratio of room and LN$_2$ temperatures. Such a large increase in the ferromagnetic coupling with decreasing temperature was previously observed for Fe/Pd/Fe trilayers [4.28].

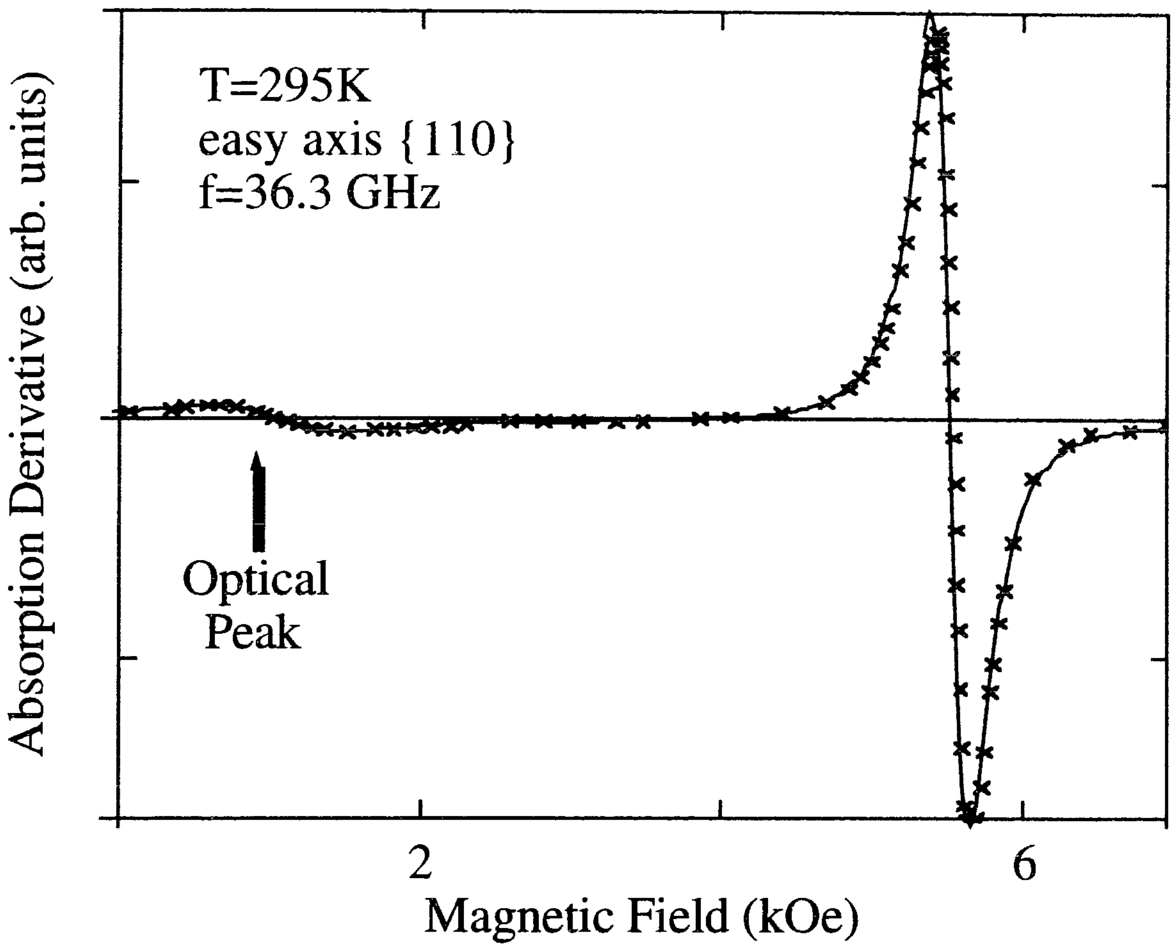

Fig. 4.7. The FMR signal along the easy axis in the sample 4Co/6Cu/4Co/3Fe/Cu. The solid line is a computer fit using the theory of the exchange coupled bilayers. The parameters used to fit the data are shown in Table 4.3. Note that the optical peak is weak and that it occurs at a smaller field than the acoustic peak: the exchange coupling between the Co layers is therefore ferromagnetic.

4.3.3. Ferromagnetic Resonance on 4Co/10Cu/10Co

The FMR data obtained for the 4Co/10Cu/10Co displayed two FMR peaks, see Fig. 4.8. However the low field weak peak observed in this sample is definitely not related to the optical mode. It is located at a field which is too small to saturate the sample. The absence of the optical mode is very likely due to the fact that the resonance fields of 4Co and 10Co layers in the 4Co/10Cu/10Co trilayer are very nearly equal which results in a

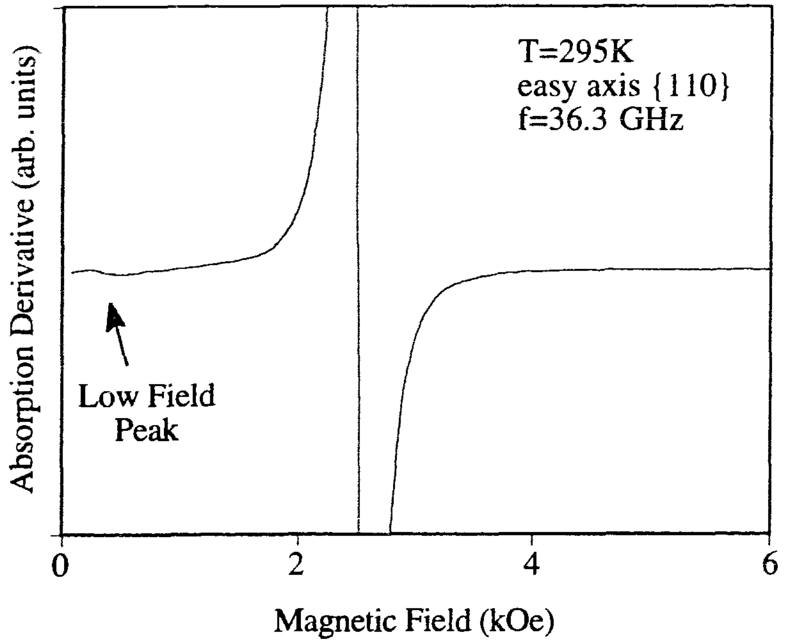

Fig. 4.8. The FMR signal in the sample 4Co/10Cu/10Co/10Cu/20Au. The dc field is along the easy axis. The low field weak peak is located below the saturation field and it does not correspond to the optical mode. In order to enhance the peak in the lower field it was necessary to increase the sensitivity of measurement resulting in clipped higher peak.

negligible intensity of the optical mode. This is a surprising result since the optical mode was observed in the sample 4Co/6Cu/10Co. Apparently, the magnetic properties of the individual layers are more equalized in the trilayer containing the thicker 10 ML copper spacer than in that containing 6 ML Cu.

Chapter 5

Summary of magnetic properties of fcc Co(001) ultrathin structures

Co(001) films grown on an fcc Cu(001) substrate show a strong perpendicular uniaxial anisotropy with the hard axis along the film normal. The in-plane fourfold anisotropy is also strong with the easy axes along the <110> crystallographic directions. Both anisotropies can be represented by bulk and surface contributions. The bulk terms of the uniaxial anisotropy are mainly attributed to tetragonal distortions resulting from lattice mismatch between metastable fcc Co(001) and fcc Cu(001). The surface term is most likely due to the broken symmetry at the interfaces. The surface uniaxial perpendicular anisotropy in Co/Cu(001) structures is negative in contrast to other Co structures which possess a positive surface anisotropy: a positive surface anisotropy corresponds to a tendency to align the magnetization along the specimen normal.

The uniaxial anisotropies in the 1.7 ML sample and the in-plane fourfold anisotropies in the 1.7 ML and in the 3.3 ML samples exhibit a deviation from the simple behavior described by a constant term plus a 1/d term. The uniaxial and the fourfold in-plane anisotropies in the 1.7 ML sample at 77K are lowered (in absolute value) due to the decreased strain and the increased surface roughness. The magnetic anisotropies in the 1.7 ML sample at 295K are additionally decreased because T_C lies just below room temperature. The decrease of the fourfold in-plane anisotropies in the 3.3 ML sample can be mainly attributed to reduced strain.

The temperature dependence of both anisotropies is very strong. The bulk terms are not appreciably changed upon cooling from room to liquid nitrogen temperatures, but the surface terms are very strongly affected by the cooling. In the case of the uniaxial anisotropy the bulk term is most likely affected by a temperature dependence of the magnetostriction constant. The 1/d term behavior might be explained using fluctuations due to 2-D spin wave theory if the change in magnetization upon heating from 77 K to 300 K is ~17 %. The temperature dependence of the surface contribution to the fourfold in-plane anisotropy is intriguing, and cannot be explained by a simple model.

Similar magnitudes of the g-factors, the 4 fold in-plane anisotropies and the intrinsic Gilbert damping in ultrathin fcc Co(001) layers and those of bulk fcc Ni suggests that the contribution of the spin-orbit interaction to their 3d bands is very similar. Ultrathin fcc Co(001) layers and bulk hcp Co also have similar g-factors, but the Gilbert damping in fcc cobalt is three times larger than that in hcp cobalt.

FMR studies of two Co(001) layers exchange coupled through a Cu(001) interlayer show that the magnetic properties of the individual Cu/Co/Cu layers are significantly modified in exchange coupled structures. In Cu/Co/Cu/Co/Cu structures the magnetic properties of the constituent Co layers are very similar despite differences in their thicknesses. As a result the optical peaks in the FMR response are either very weak or unobservable. The only observable antiferromagnetic exchange coupling was found in the 4Co/6Cu/10.3Co trilayer. The exchange coupling in that sample was anisotropic with the coupling larger along the easy magnetic axis.

A single film of 4Co/3Fe exhibits properties expected from the strong coupling of a 4 ML Co to a 3 ML Fe layer. When combined into a trilayer

4Co/6Cu/(4Co/3Fe), the two magnetic layers retained their individual properties while coupling ferromagnetically across the Cu spacer. This was in strong contrast with the behavior of a trilayer 4Co/6Cu/10Co in which the coupling was found to be antiferromagnetic and the two Co layers did not retain their individual properties.

APPENDIX A

Undercoupled microwave cavity

The microwave cavity is characterized by its quality factor. The cavity quality factor, Q_{cavity}, is given by:

$$Q_{cavity} = \frac{W}{P_{cavity}} \tag{A.1}$$

where W is the microwave power stored in the cavity and P_{cavity} describes the microwave power absorption inside the cavity. The microwave power absorption P_{cavity} is the sum of the microwave power absorption of the sample, P_{sample}, and the microwave power absorption of the other parts of the cavity (i.e. other walls), P_{walls}:

$$P_{cavity} = P_{sample} + P_{walls} \tag{A.2}$$

or in terms of the quality factors,

$$\frac{1}{Q_{cavity}} = \frac{1}{Q_{sample}} + \frac{1}{Q_{walls}} \tag{A.3}$$

Hence the changes in the power absorption of the sample result in the changes of the quality factor of the cavity, Q_{cavity}.

The cavity is coupled to the waveguide through a small coupling hole (an orifice). The external quality factor Q_{ext} is given by:

$$Q_{ext} = \frac{W}{P_{orifice}} \tag{A.4}$$

where $P_{orifice}$ represents a leakage of the microwave power through the coupling hole and depends on the size of the orifice. The ratio

$$\beta = \frac{Q_{ext}}{Q_{cavity}} = \frac{P_{cavity}}{P_{orifice}} \tag{A.5}$$

is called the microwave cavity coupling parameter. The reflected amplitude of the microwave electric component, E_r, from the cavity is given by [3.14]:

$$\frac{E_r}{E_o} = \frac{1-\beta}{1+\beta} \tag{A.6}$$

where E_0 is the incident microwave amplitude. In the following discussion $E_0=1$. For $\beta=1$ (critical coupling) all the incident power is absorbed and the cavity is matched to the waveguide. The microwave cavity is undercoupled for $\beta>1$ and overcoupled for $\beta<1$. Formula (A.6) allows one to determine the dependence of the reflected amplitude , E_r, on the power absorbed by the sample, P_{sample}. The FMR measurements were carried out using an undercoupled cavity. The quality factor of the cavity Q_{cavity} is given by:

$$\frac{1}{Q_{cavity}} = \frac{P_{walls}}{W}(1+x), \tag{A.7}$$

where

$$x = \frac{P_{\text{sample}}}{P_{\text{walls}}} \tag{A.8}$$

The parameter x represents the microwave absorption in the film. Equation (A.5) can be rearranged as

$$\beta = \frac{Q_{\text{ext}}}{W} P_{\text{walls}}(1+x) = \frac{Q_{\text{ext}}}{Q_{\text{walls}}}(1+x) = \beta_0(1+x) \tag{A.9}$$

The reflected amplitude is then given by

$$\mathbf{E}_r + \Delta\mathbf{E}_r = \frac{\beta_0^{-1} - 1 - x}{\beta_0^{-1} + 1 + x} \tag{A.10}$$

For a weak microwave absorption in FMR x<<1 and the change in the reflected microwave amplitude can be approximated using the Taylor expansion:

$$\mathbf{E}_r + \Delta\mathbf{E}_r \approx \frac{1-\beta_0}{1+\beta_0} - \frac{2\beta_0 x}{(1+\beta_0)^2} \tag{A.11}$$

The reflected amplitude in the absence of an FMR signal is given by:

$$E_r = \frac{1-\beta_0}{1+\beta_0} \tag{A.12}$$

Then the change in the reflected microwave amplitude is linearly proportional to the FMR absorption,

$$\Delta E_r = -\frac{2\beta_0 x}{(1+\beta_0)^2} \tag{A.13}$$

Note that for an undercoupled microwave cavity an increase in the microwave absorption leads to an increase of the reflected microwave amplitude ΔE_r (in this case both E_r and ΔE_r are negative).

APPENDIX B

Comparison of the face-centered-tetragonal and the body-centered-tetragonal coordinate systems.

The distorted fcc Co(001) lattice can be viewed as either face-centered tetragonal (fct) or body-centered tetragonal (bct), see figure A.1 below:

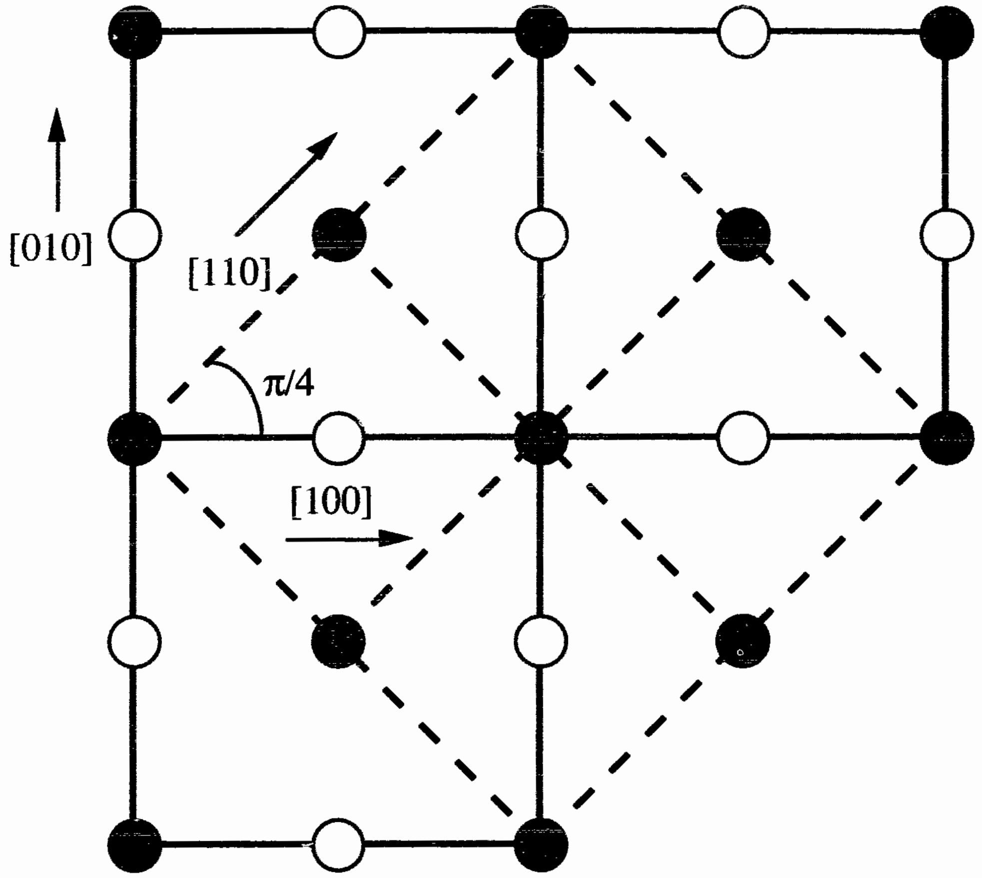

Figure A.1. View of the (001) plane: the full circles indicate Co atoms in one plane, the empty circles indicate atoms in the plane 1.74 Å above. The face-centered tetragonal bases are shown in continuous lines and body-centered tetragonal in dashed lines. The in-plane expansions along [100] and [010] are the same, while the compression is along [001] direction.

It is informative to find a relationship between magnetic anisotropies in fct and bct lattice coordinate systems. For an fct film the in-plane 4-fold magnetic anisotropy energy is

$$E_{k,fct} = -\frac{1}{2} K^{eff}_{1\parallel \mathrm{fct}} \left(\alpha^4_{x,fct} + \alpha^4_{y,fct} \right) \tag{B.1}$$

where $\alpha_{x,fct}$, $\alpha_{y,fct}$, $\alpha_{z,fct}$ are direction cosines with respect to <100> axes for the face-centered tetragonal lattice. For a bct film the in-plane 4-fold magnetic anisotropy is

$$E_{k,bct} = -\frac{1}{2} K^{eff}_{1\parallel \mathrm{bct}} \left(\alpha^4_{x,bct} + \alpha^4_{y,bct} \right) \tag{B.2}$$

Here $\alpha_{x,bct}$, $\alpha_{y,bct}$ are direction cosines with respect to in-plane <110> axes and $\alpha_{z,bct}$ is a directional cosine with respect to [001] axis. For the fct lattice the directional cosines are:

$$\alpha_{x,fct} = \sin\theta \cdot \cos\phi \ , \ \alpha_{y,fct} = \sin\theta \cdot \sin\phi \ , \ \alpha_{z,fct} = \cos\theta \tag{B.3}$$

where θ is the polar angle with respect to the [001] axis and ϕ is the azimuthal angle with respect to the [100] axis. The bct lattice is rotated by $\pi/4$ with respect to the fct lattice:

$$\alpha_{x,bct} = \sin\theta \cdot \cos\left(\phi + \frac{\pi}{4}\right) , \ \alpha_{y,bct} = \sin\theta \cdot \sin\left(\phi + \frac{\pi}{4}\right) , \ \alpha_{z,bct} = \cos\theta \tag{B.4}$$

Upon substituting the above equations into equation (B.2) we obtain:

$$
\begin{aligned}
E_{k,bct} &= -\frac{1}{2} K^{eff}_{1\parallel \mathrm{bct}} \left(\cos^4 \phi' + \sin^4 \phi'\right) \\
&= -\frac{1}{2} K^{eff}_{1\parallel \mathrm{bct}} \sin^4 \theta \left[\cos^4\left(\phi + \frac{\pi}{4}\right) + \sin^4\left(\phi + \frac{\pi}{4}\right)\right] \\
&= -\frac{1}{2} K^{eff}_{1\parallel \mathrm{bct}} \sin^4 \theta \left[\left(\cos\phi \cos\frac{\pi}{4} - \sin\phi \sin\frac{\pi}{4}\right)^4 - \left(\sin\phi \cos\frac{\pi}{4} + \cos\phi \sin\frac{\pi}{4}\right)^4\right] \\
&= -\frac{1}{2} K^{eff}_{1\parallel \mathrm{bct}} \frac{\sin^4 \theta}{4} \left[(\cos\phi - \sin\phi)^4 - (\sin\phi + \cos\phi)^4\right] \\
&= -\frac{1}{2} K^{eff}_{1\parallel \mathrm{bct}} \frac{\sin^4 \theta}{4} \left[\left((\cos\phi - \sin\phi)^2\right)^2 - \left((\sin\phi + \cos\phi)^2\right)^2\right] \\
&= -\frac{1}{2} K^{eff}_{1\parallel \mathrm{bct}} \frac{\sin^4 \theta}{4} \left[(1 - 2\sin\phi\cos\phi)^2 + (1 + 2\sin\phi\cos\phi)^2\right] \\
&= -\frac{1}{2} K^{eff}_{1\parallel \mathrm{bct}} \frac{\sin^4 \theta}{4} \left[2 + 8\sin^2\phi\cos^2\phi\right] \\
&= -\frac{1}{2} K^{eff}_{1\parallel \mathrm{bct}} \frac{\sin^4 \theta}{4} \left[2 + 4\left(1 - \cos^2\phi\right)\cos^2\phi + 4\left(1 - \sin^2\phi\right)\sin^2\phi\right] \\
&= -\frac{1}{2} K^{eff}_{1\parallel \mathrm{bct}} \frac{\sin^4 \theta}{4} \left[6 - 4\cos^4\phi - 4\sin^4\phi\right] \\
&= -\frac{1}{2} K^{eff}_{1\parallel \mathrm{bct}} \sin^4 \theta \left[\frac{3}{2} - \left(\cos^4\phi + \sin^4\phi\right)\right] \\
&= -\frac{3}{4} K^{eff}_{1\parallel \mathrm{bct}} \sin^4 \theta + \frac{1}{2} K^{eff}_{1\parallel \mathrm{bct}} \sin^4 \theta \left(\cos^4\phi + \sin^4\phi\right) \\
&= -\frac{3}{4} K^{eff}_{1\parallel \mathrm{bct}} \left(1 - \cos^2\theta\right)^2 + \frac{1}{2} K^{eff}_{1\parallel \mathrm{bct}} \left(\alpha^4_{x,fct} + \alpha^4_{y,fct}\right) \\
&= -\frac{3}{4} K^{eff}_{1\parallel \mathrm{bct}} + \frac{3}{2} K^{eff}_{1\parallel \mathrm{bct}} \alpha^2_{z,fct} - \frac{3}{4} K^{eff}_{1\parallel \mathrm{bct}} \alpha 4^2_{z,fct} + \frac{1}{2} K^{eff}_{1\parallel \mathrm{bct}} \left(\alpha^4_{x,fct} + \alpha^4_{y,fct}\right)
\end{aligned}
$$

$$
E_{k,bct} = -\frac{3}{4} K^{eff}_{1\parallel \mathrm{bct}} + \frac{3}{2} K^{eff}_{1\parallel \mathrm{bct}} \alpha^2_{z,fct} - \frac{3}{2} K^{eff}_{1\parallel \mathrm{bct}} \alpha^4_{z,fct} + \frac{1}{2} K^{eff}_{1\parallel \mathrm{bct}} \left(\alpha^4_{x,fct} + \alpha^4_{y,fct}\right) \text{(B.5)}
$$

By comparing the above equation with equations (3.38) and (B.2) we can conclude that a simple rotation of the coordinate system from the fct to the bct lattice affects not only the sign of the in-plane 4-fold anisotropy, but also the value of the perpendicular anisotropy. From the last term in equation (B.5) one can see that:

$$K^{eff}_{1\parallel \mathrm{bct}} = -K^{\mathrm{eff}}_{1\parallel \mathrm{fct}} \tag{B.6}$$

In addition, the second term in equation (B.5) contributes to the perpendicular uniaxial anisotropy and the third term to the 4-fold perpendicular anisotropy. The first term is just a constant that does not affect effective anisotropy fields. In our studies the 4-fold perpendicular anisotropy can be neglected. By using equation (3.29) and (B.5) , one can compare the uniaxial anisotropies , $H^{eff}_{u,bct}$ and $H^{eff}_{u,fct}$, for the bct and the fct lattice coordinate systems:

$$H^{eff}_{u,bct} = H^{eff}_{u,fct} - \frac{3K^{eff}_{1\parallel \mathrm{fct}}}{M_s} \tag{B.7}$$

$\frac{2K^{eff}_{1\parallel}}{M_s}$ and $4\pi M_{eff}$ were calculated using the bct coordinate system by solving a set of two resonance conditions (3.35) for an easy and a hard axis. The results are shown in Table B.1:

TABLE B.1 : Single-layered Co(001) samples grown on Cu(001)

All measurements were carried out at 36 Ghz. T_S is the temperature of the substrate during the growth of Co layer. Data is presented in the body-centered cubic coordinate system where α_x, α_y are directional cosines with respect to in-plane <110> axes, and α_z is the directional cosine with respect to [001] axis.

		295K			77K		
SAMPLE	T_S (K)	H_u* (kOe)	$4\pi M_{eff}$ (kOe)	$\frac{2K^{eff}_{1\parallel}}{M_S}$ (kOe)	H_u* (kOe)	$4\pi M_{eff}$ (kOe)	$\frac{2K^{eff}_{1\parallel}}{M_S}$ (kOe)
1.7Co/11.5Cu/20Au	330	-15.4	30.8	0.065	-39.0	54.4	0.60
3.3Co/6Cu/20Au	375	-25.9	42.5	0.85	-34.7	51.3	2.09
4Co/6Cu/20Au	300	-25.1	41.9	1.10	-31.3	48.1	2.21
6.5Co/10.5Cu/20Au	300	-20.1	37.3	1.25	-23.2	40.4	2.04
8.6Co/10.5Cu/20Au	300	-18.5	35.9	1.27	-20.8	38.2	1.83
10Co/10Cu/20Au	355	-17.3	34.8	1.29	-18.8	36.3	1.81
4Co/3Fe/8.5Cu/20Au	300	X	15.6	0.41	X	15.6	0.60

* using $4\pi M_S = 17.87$ kOe for hcp Co.

In the fct lattice coordinate system the in-plane fourfold anisotropy energies, $\frac{2K^{eff}_{1\parallel}}{M_s}$, are large negative numbers, see table 4.1, whose absolute values are equal to those of table B.1 calculated for the bct coordinate system.. However, the effective perpendicular demagnetizing fields, $4\pi M_{eff}$, and the perpendicular uniaxial anisotropy fields, $\frac{2K_u^{eff}}{M_s}$, in fct are larger in absolute value by $\left|\frac{3K_{1\parallel}^{eff}}{M_s}\right|$(compare table 4.1 with table A.1). Both analyses are valid and it is difficult to say which one is more appropriate. However, the fct coordinate system is usually employed, and the analysis in the main body of this thesis was carried out using the fct system.

REFERENCES:

Chapter 1

1.1 L. Gonzales, R. Miranda, M. Salmeron, J.A. Verges and F. Yndurain, Phys.Rev., **B24**,3245,(1981)

Chapter 2

2.1 J.R. Cerdá, P.L. de Andres, A. Cebollada, R. Miranda, E. Navas, P. Schuster, C.M. Schneider, and J. Kirschner, J. Magn. Magn. Mater. **121**, 65 (1993).

2.2 L.E. Davis, N.C. MacDonald, P.W. Palmberg, G.E. Riach and R.E. Weber, *"Handbook of Auger Electron Spectroscopy"*, Physical Electronics, Minnesota, 1978.

2.3 *"Practical Surface Analysis by Auger and X-Ray Photoelectron Spectroscopy"*, edited by D. Briggs, M.P. Sheah, John Wiley & Sons, New York, 1983.

2.4 C. Kittel, *"Introduction to Solid State Physics"* , John Wiley & Sons Inc., New York, 1986, p 35.

2.5 E. Bauer, in *"Techniques of Metals Research"*, Edited by R.F. Bunshah, Wiley Interscience, New York , 1969, vol 2, p 201; A.S. Arrott, in *"Ultrathin Magnetic Structures"*, edited by B. Heinrich and A. Bland (Springer Verlag, Berlin, in press) Vol. II.

2.6 P.R. Pukite, *"Reflection High Energy Electron Diffraction of Interface Formation"*, PhD Thesis, University of Minnesota, 1988.

2.7 J.M. Van Hove, C.S. Lent, P.R. Pukite, and P.I. Cohen, J. Vac. Sci. Technol. **B 1** (3), 741, 1983.

2.8 A.S. Arrott, B. Heinrich, S.T. Purcell, *"Kinetics of Ordering and Growth at Surfaces"*, edited by M.G. Legally, Plenum Press, New York, (1990).

2.9 C.M. Schneider, P. Bressler, P. Schuster, J. Kirschner, J.J. Miguel and R. Miranda, Phys.Rev.Lett., **64**,1059,(1990); C.M. Schneider, *"Electronic Structure and Magnetic Properties of Ultrathin Films: fcc-Cobalt on Cu(100)"*, thesis, Free University, Berlin, 1990 (unpublished).

2.10 J. Kirschner, private communication.

2.11 J.W. Evans, D.E. Sanders, P.A. Thiel and A.E. DePristo, Phys.Rev., **B41**,5410,(1990-I).

2.12 C. M. Schneider, P. Bressler, P. Schuster, J. Kirschner, J. J. de Miguel, and R. Miranda, Phys. Rev. Lett. **64**, 1059 (1990); J. J. de Miguel, A. Cebollada, J. M. Gallego, R. Miranda, C. M. Schneider, P. Schuster, J. Kirschner, J. Magn. Magn. Mater. **93**, 1(1991).

2.13 D. Chandesris, H. Magnan, O. Heckmann, S. Pizzini, in: *"Structure and Magnetism in Low Dimensional Systems"*, eds. R.F.C. Farrow, M. Donath, B. Dieny, A. Fert, B. Hermsmeier, (Plenum, New York, 1993).

Chapter 3

3.1 A.G. Gurevich, *"Ferrites at Microwave Frequencies"*, Consultants Bureau, New York (1963).

3.2 K.B. Urquhart, *"The Magnetic Properties of Ultrathin Films of Fe(001) grown on Ag(001) Substrates"*, Ph.D. Thesis, Simon Fraser University, (1989).

3.3 B. Heinrich, in *"Ultrathin Magnetic Structures"*, edited by B. Heinrich and A. Bland (Springer Verlag, Berlin, in press) Vol. II.

3.4 W.F. Brown, *"Micromagnetics"*, Interscience Publishers, New York, (1963).

3.5 J.F. Cochran, in *"Ultrathin Magnetic Structures"*, edited by B. Heinrich and A. Bland (Springer Verlag, Berlin, in press) Vol. II.

3.6 J.R. McDonald, Proceedings of Physics Society, A **64**, 968, (1951).

3.7 S. Chikazumi, *"Physics of Magnetism"*, Robert E. Krieger Publishing Co, Malabar Florida, (1986).

3.8 G.T. Rado, Phys. Rev. B **26**, (1982); G.T. Rado, Phys. Rev. B **32**, (1985).

3.9 J.F. Cochran, B. Heinrich, A.S. Arrott, Phys. Rev. B **34**, 7788, (1988).

3.10 B. Heinrich, J. F. Cochran, M. Kowalewski, J. Kirschner, Z. Celinski, A.S. Arrott, and K. Myrtle, Phys. Rev. B **44**, 9348 (1991).

3.11 B. Heinrich, S.T. Purcell, J.R. Dutcher, J.F. Cochran, A.S. Arrott, Phys. Rev. B **38**, 12879, (1988).

3.12 B. Heinrich, K.B. Urquhart, A.S. Arrott, J.F. Cochran, K. Myrtle, and S.T. Purcell, Phys .Rev. Lett. **59**, 1756, (1987).

3.13 B. Heinrich, J.F. Cochran, and R. Hasegawa, J. Appl. Phys., **54**, 3690, (1985)

3.14. Z.J. Celinski, *"Molecular Beam Epitaxy Growth and Magnetic Studies of Fe Ultrathin Structures"*, Ph.D. Thesis, 1992; B. Heinrich, in *"Ultrathin Magnetic Structures"*, edited by B. Heinrich and A. Bland (Springer Verlag, Berlin, in press) Vol. II.

3.15. A.T. Starr in Radio and Radar Technique, Sir Isaac Pitman & Sons,Limited, London 1953.

Chapter 4

4.1. M. Kowalewski, C.M. Schneider, and B. Heinrich, Phys Rev B **47**, 8748, 1993.

4.2. C. M. Schneider, P. Bressler, P. Schuster, J. Kirschner, J. J. de Miguel, and R. Miranda, Phys. Rev. Lett. **64**, 1059 (1990).; J. J. de Miguel, A. Cebollada, J. M. Gallego, R. Miranda, C. M.Schneider, P. Schuster, J. Kirschner, J. Magn. Magn. Mater. **93**, 1(1991).

4.3 B.N. Engel, M.H. Wiedmann, R.A. Van Leeuwen, C.M. Falco, Lianjun Wu, Noriaki Nakajama, and T. Shinjo, Appl. Surf. Sci., in press

4.4. H.A.M. de Gronckel, K. Kopinga, W.J.M. de Jonge, P. Panissod, J.P. Schille, and F.J.A. den Broader, Phys. Rev. B **44**, 9100 (1991).

4.5. A.K. Schmid, *"Growth of Epitaxial Co Thin Films on Cu(100) Studied by Scanning Tunneling Microscopy"*, PhD thesis, Free University, Berlin, 1991 (unpublished); A. K. Schmid and J. Kirschner, Ultramicroscopy **42-44**, 483 (1992).

4.6 B. Heinrich, Z. Celinski, J. F. Cochran, A. S. Arrott, and K. Myrtle, J. Appl. Phys. **70**, 5769, (1991); L. Neel, J. Phys. Radium **15**, 225 (1954); S. Chikazumi, *"Physics of Magnetism"* (Robert E. Krieger Publishing Co., Malabar Florida, 1986), pp. 167-175.

4.7 *"Elastic, Piezoelastic, Pyroelectric, Piezooptic, Electrooptic Constants and Nonlinear Dielectric Susceptibilities of Crystals"*, Landolt-Bornstein, New Series Group 3, Vol. 18, edited by K.H. Hellewege and A.H. Hellewege, (Springer-Verlag, Berlin, 1984).

4.8. H. Fujiwara, H. Kadomatsu, and T. Tokunaga, J. Magn. Magn. Mater. **31-34**, 809 (1983).

4.9. B.N. Engel, C.D. England, R.A. Van Leeuwen, M.H. Wiedmann, and C. M. Falco, J. Appl. Phys. **70**, 5873, (1991).

4.10. B. N. Engel, C.D. England, R.A. Van Leeuwen, M.H. Wiedmann, and C.M. Falco, Phys. Rev. Lett. **67**, 1910 (1991).

4.11. J.V. Harzer, B. Hillebrands, R.L. Stamps, G. Guntherodt, D. Weller, Ch. Lee, R. F. C. Farrow, and E. E. Marinero, J. Magn. Magn. Mater. **104-107**, 1863 (1992).

4.12. C.J. Chien, B.M. Clemens, S.B. Hagstrom, R.F.C. Farrow, C.H. Lee, E.E. Marinero, C.J. Lin, Mat. Res. Soc. Symp. Proc. Vol. 231, (1992).

4.13. W.J.M. de Jonge, P.J.H. Bloemen, F.J.A. den Broader, in *"Ultrathin Magnetic Structures"*, Vol. I, edited by B. Heinrich and A. Bland (Springer Verlag, in press).

4.14. H.J.G. Draaisma, F.J.A. den Broader, F.J.M. de Jonge, J. Appl. Phys. **63**, 3479 (1988).

4.15. Dien-sheng Wang, R. Wu, and A.J. Freeman, *"Magneto-crystalline Anisotropy of Interfaces: First Principle Theory for Co-Cu Interface and nterpretation by an Effective Ligand Model"*, preprint, 1993.

4.16. P. Krams, F. Lauks, R.L. Stamps, B. Hillebrands, and G. Guntherodt, Phys. Rev. Lett., 69, 3674, (1992).

4.17. P. Bruno, J. Phys. F: Met. Phys. **18**, 1291, (1988).

4.18. E.W. Lee and M.A. Asgar, Proc. Roy. Soc. London, **A326**, 73, (1971).

4.19. D.L. Mills, in *"Ultrathin Magnetic Structures"*, Vol. I, edited by B. Heinrich and A. Bland (Springer Verlag, in press).

4.20. J. Tobochnik, Phys. Rev. B **26**, 6201, (1982).

4.21. B. Heinrich, K.B. Urquhart, A.S. Arrott, J.F. Cochran, K. Myrtle and S.T. Purcell, Phys.Rev.Lett. **59**, 1756, (1987).

4.22. S.M. Bhaghat and P. Lubitz, Phys Rev B **10**, 179, (1974).

4.23. S.T. Purcell, B. Heinrich, and A.S. Arrott, J.Appl.Phys., **64**, 5337, (1988).

4.24. G. Dewar, B. Heinrich, J.F. Cochran, Can. J. Phys., **55**, 821, (1977).

4.25. (a) J.F. Cochran and B.Heinrich, IEEE Transactions on Magnetics, **Mag-16**, 660, (1980); (b) V. Kambersky, Can. J.Phys., **B 26**, 1366, (1976); (c) V.Korenman and R.E. Prange, Phys.Rev, **B 6**, 2769, (1972).

4.26. B. Heinrich, S.T. Purcell, J.R. Dutcher, J.F. Cochran and A.S. Arrott,Phys.Rev, **B38**,1279,(1988)

4.27. B. Heinrich, Z. Celinski, J.F. Cochran, W.B. Muir, J. Rudd, Q.M. Zhong, A.S. Arrott, K. Myrtle, and J. Kirschner, Phys.Rev.Lett. **64**, 673, (1990).

4.28. Z. Celinski, B. Heinrich, J.F. Cochran, W.B. Muir, A.S. Arrott and J. Kirschner, Phys. Rev.Lett. **65**, 1156, (1990).

4.29. J.J. de Miguel, A. Cebollada, J.M. Gallego, R. Miranda, C.M. Schneider, P. Schuster and J. Kirschner, J. Magn. Magn. Mater. **93**, 1 (1991).